Automatic Determination of Network Openings in Meshed LV Grids

Master of Science Thesis

Mirthe Otter

Delft University of Technology

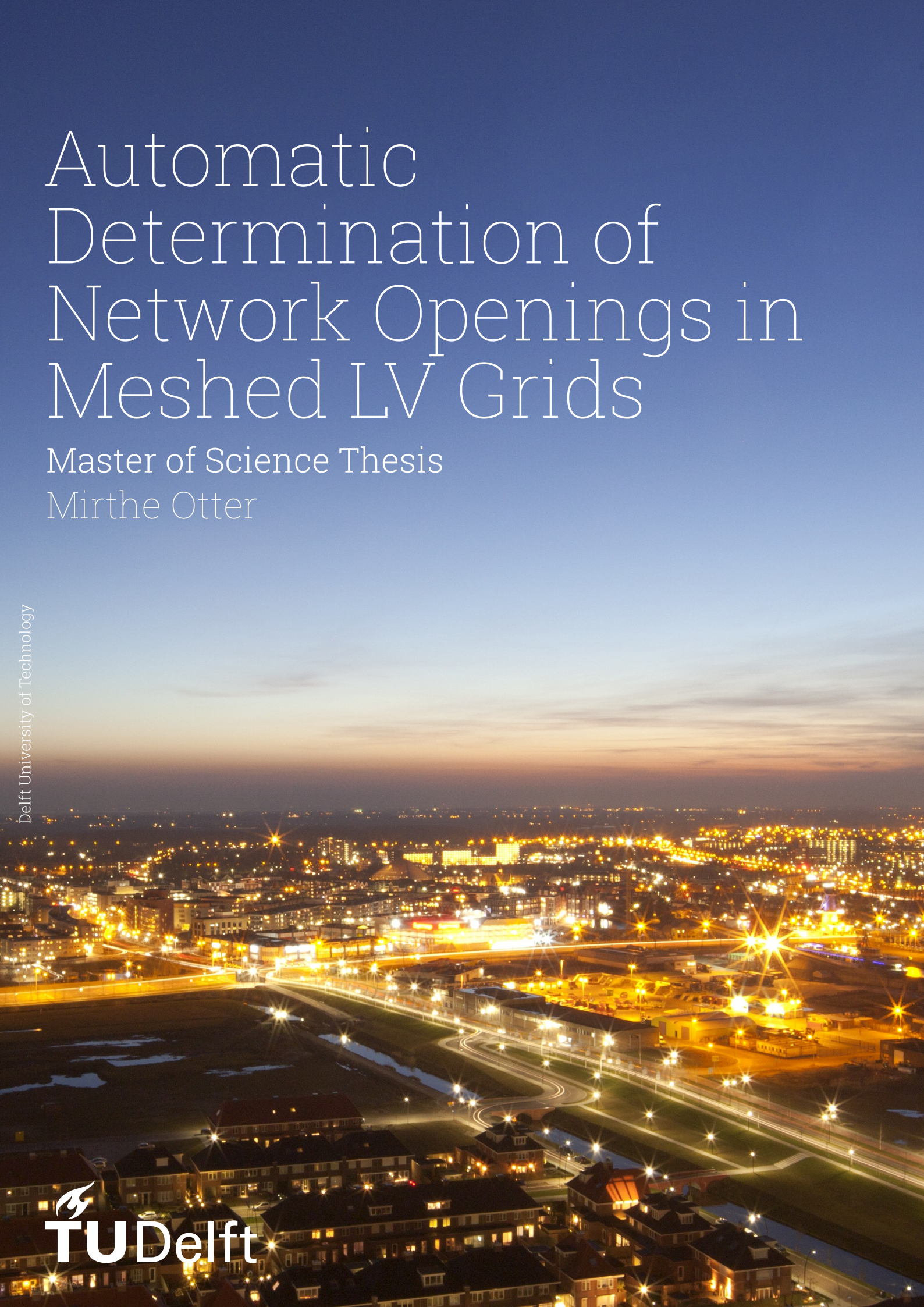

TU Delft

Automatic Determination of Network Openings in Meshed LV Grids

by

Mirthe Otter

to obtain the degree of Master of Science
in Electrical Engineering
at the Delft University of Technology,
to be defended publicly on July 1, 2026 at 09:00 AM.

Thesis committee:	dr. P.P. Vergara Barrios,	Supervisor, IEPG
	Z. Kaseb, MSc.,	Daily Co-Supervisor, IEPG
	dr. dipl. ing. J.L Rueda Torres,	Committee Chair, IEPG
	dr. ir. M Ghaffarian Niasar,	Committee Member, HVT
	dr. ir. E.J. Coster,	External Member, Stedin
	ir. J.W.B. Kers,	External Member, Stedin

An electronic version of this thesis is available at `https://repository.tudelft.nl`.

This thesis was made possible through the support of Stedin Netbeheer B.V.

TU Delft

STEDIN.NET

Abstract

The rapid growth of renewable energy integration, alongside the tightening of safety requirements for protection against electrical shock, is forcing distribution system operators to reassess low voltage grid planning and operation. In response, Stedin has adopted a long-term strategy to de-mesh all low voltage grids by 2040. This presents a significant challenge, as more than 50% of Stedin's low voltage grids (excluding Zeeland) were still operated in a meshed configuration in 2025.

Meshed low voltage grids interconnect secondary substations and end-users through multiple paths, providing operational flexibility. However, these configurations complicate protection coordination and increase short-circuit current levels, resulting in more complex and widespread disturbances during fault conditions. In contrast, radial low voltage grids exhibit more predictable power flow behaviour and improved controllability, making them better suited to accommodate increasing electrification and distributed generation while complying with stricter safety requirements. Consequently, identifying permanent network opening points to achieve radial configurations is essential for developing reliable, compliant, and future-proof distribution systems.

System performance after de-meshing is sensitive to the placement of network openings, making accurate modelling of electrical interactions between interconnected secondary substations a prerequisite for informed decision-making. Existing medium voltage and low voltage grid models often rely on simplified assumptions that neglect critical interactions among multiple closed loops, potentially leading to sub-optimal opening decisions. To address this, an integrated medium- and low voltage grid model is developed in DIgSILENT PowerFactory that explicitly represents electrically relevant low voltage grid sections together with their supplying medium voltage feeders.

To support a systematic transition from meshed to radial topologies while balancing multiple performance criteria, this thesis proposes a simulation–optimisation framework for the automatic identification of feasible permanent network openings. The approach integrates a genetic algorithm implemented in Python with quasi-dynamic simulations within a closed-loop framework. This enables an efficient exploration of the highly combinatorial solution space, yielding technically feasible and near-optimal configurations that remain robust under diverse operating conditions.

Applied to a realistic case study, the framework reduces annual energy losses by 6.6% and lowers maximum feeder voltage drops by 4.07 V compared to a fuse-removal based industrial approach, while achieving performance comparable to heuristic cable-disconnecting methods. The heuristic initial search point strategy, used during initialisation to obtain efficient starting solutions and enhance convergence, provides a strong low-complexity baseline and achieves near-optimal results for the studied network. By enabling globally coordinated optimisation across interacting network sections, the proposed framework shows promise for decision-making in large, complex meshed low voltage grids.

Preface & Acknowledgements

First of all, I would like to thank my supervisor, Pedro Vergara Barrios, for his guidance and support throughout the past academic year. Unexpectedly, following the departure of my initial supervisor, I had to look for an alternative. This transition turned out to be seamless, as the project aligned well with your field of expertise. Beyond the academic content, I greatly appreciated your guidance in structuring and managing a project of this scale.

I would also like to thank Zeynab Kaseb for introducing me to the world of optimisation algorithms and for helping me integrate optimisation logic with the simulation environments.

Next, I would like to thank Stedin, and in particular Bart Kers and Edward Coster. Bart, you were involved from start to finish and consistently positive and enthusiastic, which was highly motivating. Most importantly, you and Edward provided weekly advice, taught me a great deal about practices within Stedin, and supported me with insights and knowledge whenever needed. Edward, I would also like to thank you for stepping in as a supervisor and for the critical perspective you brought to my thinking and writing process, which greatly improved the quality of this work. I also want to thank Stephan van der Linde for helping set up the project and for introducing me to the world of distribution system operators, as well as to the many professionals who deal with the practical challenges of meshed distribution networks.

Furthermore, I am grateful to Nahom Tsehaie for his assistance with customer data and profile fractions. I would also like to thank Stijn Zwanenburg, Willem van Seters, Reinier Bekkenutte, and Gijs Henstra for explaining MV and LV grid modelling practices and for keeping me informed about developments in Gaia. In addition, I appreciate Louise Postma and Koen Peelen for demonstrating the DA3 measurement setups and for providing both data and clear explanations on how to use them.

I would also like to thank Phase to Phase, and especially Anton Ischenko and Berto Jansen, for answering my questions and providing detailed information about Gaia models and the de-meshing approach. I am also grateful to Mitch Terpak for his support in working with the Python library.

Finally, I want to thank my family and friends for their enthusiasm, support, and all the enjoyable moments surrounding this final chapter of my studies. In particular, I am very thankful to Willem, who has always stood by my side, listened patiently to my daily ups and downs, and even kept my simulations running while I was away on a short holiday.

Mirthe Otter
Delft, June 2026

Contents

Nomenclature

Abbreviations

Abbreviation	Definition
AC	Alternating current
ACM	Authority for Consumers and Markets
AI	Artificial Intelligence
ANN	Artificial Neural Network
API	Application Programming Interface
DA3	Distribution Automation 3
DC	Direct current
DER	Distributed Energy Resource
DG	Distributed generation
DDNR	Dynamic Distribution Network Reconfiguration
DN	Distribution network
DNR	Distribution network reconfiguration
DSO	Distribution System Operator
EAN	European Article Numbering
EDSN	Energie Data Services Nederland
EENS	Expected Energy Not Supplied
EN	European norm
ESS	Energy Storage System
EV	Electric vehicle
FFDWMPF	Fast Flexible Direct Weakly Meshed Power Flow
FL	Fundamental loop
GA	Genetic Algorithm
GMM	Gaussian Mixture Model
HV	High voltage
IEC	International Electrotechnical Commission
ISO	International Organisation for Standardisation
ISP	Initial searching point
KPI	Key performance indicator
LV	Low voltage
MINLP	Mixed-Integer Nonlinear Programming
ML	Machine Learning
MST	Minimum Spanning Tree
MV	Medium voltage
MSE	Mean squared error
NEN	Dutch norm
NR	Newton–Raphson
PE	Protective earth
PV	Photovoltaic
QD	Quasi-dynamic
RL	Reinforcement Learning
SAC	Standard annual consumption
SAFI	Standard annual feed-in
SAIDI	System Average Interruption Duration Index
SAIFI	System Average Interruption Frequency Index
SDNR	Static Distribution Network Reconfiguration

Abbreviation	Definition
SGT	Smart Grid Terminal
TSO	Transmission System Operator
VSI	Voltage Stability Index

Symbols

Symbol	Definition	Unit
A	Bus-branch incidence matrix	[$-$]
B_i	Bus i	[$-$]
C	Chromosome representing a network reconfiguration	[$-$]
c	Decision variable, i.e. gene	[$-$]
E	Energy	[Wh] E_j
Branch j	[$-$]	
$\mathrm{fitness}$	Objective (fitness value)	[$-$]
I	Current	[A]
k	Transformation ratio	[$-$]
k_i	Branch operational status indicator	[$-$]
L	Number of fundamental loops	[$-$]
M	Binary mask vector	[$-$]
N_b	Number of buses	[$-$]
N_e	Number of branches	[$-$]
P	Active power	[W]
Q	Reactive power	[var]
R	Resistance	[Ω]
S	Apparent power	[VA]
t	Time-step index	[h]
T	Total number of time steps	[$-$]
U	Voltage	[V]
V	Set of all loop vectors	[$-$]
X	Reactance	[Ω]
Z	Impedance	[Ω]
λ_d	Voltage drop penalty coefficient	[$-$]
λ_f	Power loss penalty coefficient	[$-$]
λ_l	Cable loading penalty coefficient	[$-$]
λ_t	Transformer loading penalty coefficient	[$-$]
λ_v	Voltage deviation penalty coefficient	[$-$]
ϕ	Phase angle	[rad]

1

Introduction

Grid operators face the challenge of adapting the power system to accommodate the rapid growth of renewable energy integration. This challenge intensified after the Paris Agreement in 2015, which set ambitious national targets for reducing greenhouse gas emissions by 49% [1]. A key target is the transition to a CO_2-free electricity system by 2050, which necessitates a substantial increase in distributed generation (DG), such as small-scale photovoltaic (PV) installations connected at lower voltage levels. This transition marks a shift from a vertically to a horizontally operated power system, fundamentally changing network planning and operation. Consequently, alternative control and operational strategies are required to maintain system stability and safe operating margins.

At the same time, Dutch Distribution System Operators (DSOs) face an additional regulatory challenge. In 2022, the Dutch Authority for Consumers and Markets (ACM) revised the Electricity Network Code, introducing stricter safety requirements regarding protection against electrical shock [2]. Low voltage (LV) grids built before April 2018 must comply by 2027, leaving DSOs with a limited timeframe to act. The revised regulations aim to reduce risks associated with electrical faults and enhance public safety, harmonizing safety standards across existing and newly constructed grids [3]. When combined with the rapid increase in DG penetration, these regulatory changes necessitate an urgent reassessment of grid planning and operational practices.

To address these combined challenges, Stedin has adopted a long-term strategy to de-mesh all LV grids by 2040 [4], [5]. The five-year transition period mandated by ACM serves as a critical phase in preparing the distribution grid for full compliance with the enhanced safety requirements regarding protection against electrical shock. During this period, priority is given to LV grids where de-meshing yields the greatest safety improvements.

Historically, Stedin's network architecture presents unique challenges. In contrast to other Dutch DSOs, which operate LV grids radially, approximately 53% of Stedin's LV grids (excluding Zeeland) are operated in a meshed configuration. Meshing could improve voltage regulation and reduce network losses, and meshed grids may better accommodate DG [6], [7], [8]. However, from a protection perspective, disadvantages outweigh these benefits. In the event of a fault, current can flow from multiple directions, complicating protection selectivity and increasing short-circuit currents, especially with high DG penetration [9]. As a result, Stedin experiences complex, large-scale disturbances in its meshed LV grids. This poses risks to Stedin's ability to fulfil its statutory obligations as a DSO, regarding grid reliability and quality of supply [4].

Figure 1.1 illustrates the ratio of network structures in Stedin's service area as of November 2025, highlighting the scale of the challenge at hand. Although installing additional load-break switches could enable radial operation, technical and economic evaluations led to the selection of physical de-meshing as the adopted approach. Given the increased operational and safety risks associated with meshed LV grids under growing DG penetration, physical de-meshing is not only the most robust long-term solution, but also an urgent necessity to ensure regulatory compliance, operational reliability, and public safety.

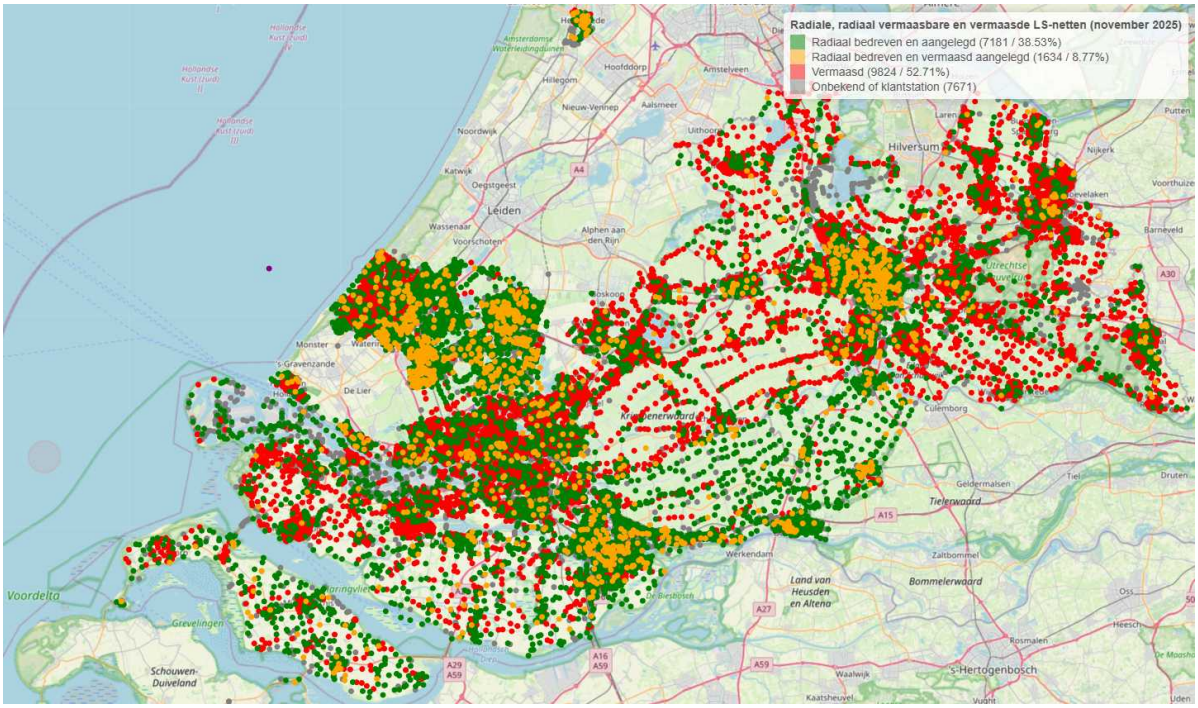

Figure 1.1: Overview of configuration of LV grids in Stedin's supply area (excluding Zeeland) in November 2025. Green indicates LV grids that are configured and operated radially (38.53%). Orange indicates LV grids that are configured as meshed but operated radially (8.77%). Red indicates LV grids that are both configured and operated meshed (52.71%). Grey dots represent unknown configurations or customer stations.

1.1. Problem Statement and Research Motivation

1.1.1. Meshed LV Grid Modelling

Modelling choices at each network level reflect trade-offs between model complexity and intended purpose. Greater detail improves the representation of physical network behaviour but increases development effort and computational cost. To balance accuracy and efficiency, Stedin models medium voltage (MV) and LV grids separately. LV grids are typically represented as isolated radial networks or, where connected via LV mesh cables, as weakly coupled to neighbouring secondary substations directly interconnected by these cables.

In current LV grid models, each secondary substation is assigned an independent swing bus. This modelling assumption neglects voltage magnitude and phase-angle differences caused by voltage drops along the MV feeder connecting meshed secondary substations. Although these models are fit for their intended purposes, such as planning studies, they do not accurately represent phenomena characteristic of meshed LV grid operation.

This simplified approach prevents the full representation of circulating currents in LV mesh cables, leading to inaccurate assessments of power flow behaviour and asset loading. This is critical, as these voltage differences together with mismatches in distribution transformer tap settings are known to induce circulating currents, increasing loading of cables and transformers [10], [11]. As LV grids increasingly operate closer to their technical limits due to rising demand and DG penetration, accurate assessment of network capacity and asset loading becomes essential.

These limitations highlight the need for an improved modelling approach for meshed LV grids that leverages existing tools and available measurement data. Such an approach should be compatible with current workflows and applicable by network operators in practice.

This research therefore investigates how meshed LV grids can be modelled within current distribution network tools to capture key electrical interactions, in particular circulating currents, while remaining computationally manageable. The model should further support LV grid de-meshing by enabling systematic identification of feasible network opening locations and integration with optimisation logic.

1.1.2. Automatic Determination of Network Openings in Meshed LV Grids

The placement of network openings influences post-reconfiguration performance, including network losses, voltage profiles, and asset loading. At present, Stedin relies on a dedicated tool, developed in collaboration with Phase-to-Phase, to identify feasible locations for network openings. This tool evaluates loading and voltage constraints following de-meshing and verifies compliance with short-circuit performance and safety requirements regarding protection against electrical shock. In practice, network openings are implemented either by removing fuses or by physically cutting the mesh cables [12].

The existing approach is effective in identifying technically feasible solutions that comply with all operational and safety constraints. However, its performance is inherently linked to the underlying network models. Due to the simplified representation of meshed LV grids as weakly coupled networks, interactions between multiple closed loops are not explicitly captured. Consequently, the mutual influence of interconnected secondary substations is only partially represented, potentially leading to sub-optimal opening decisions.

In addition, the current approach follows a heuristic, rule-based procedure in which candidate locations are evaluated against a predefined hierarchy of criteria, rather than balancing system-level performance metrics such as loss minimisation, voltage profile improvement and asset loading. As a result, network opening decisions are made iteratively on a per-cable basis, without globally coordinating opening locations across interacting network sections.

This creates an opportunity to investigate whether the current de-meshing approach can be further improved by incorporating optimisation techniques that explicitly account for multiple performance objectives. Static distribution network reconfiguration (SDNR) approaches provide such optimisation methodologies, as they optimise performance metrics subject to operational constraints [13]. However, these methods are typically designed for meshed networks that are operated radially, are generally intended for seasonal or yearly operational adjustments and are limited to opening load break switches.

In contrast, LV grid de-meshing requires permanent network openings that enable a structural transition from meshed to radial topology and remain feasible under diverse operating conditions, without relying on existing switching devices. Therefore, there is a need for a methodology that integrates operational constraints with explicit optimisation objectives while remaining practically applicable within Stedin's planning environment.

Such a methodology should not aim for theoretical global optimality at the expense of modelling complexity, data requirements, or computational effort. Instead, it should identify near-optimal, technically feasible solutions that can be implemented using available data and existing modelling tools. This requires a careful balance between solution quality, robustness, and computational efficiency, as well as compatibility with current workflows.

1.2. Research Goal

The objective of this research is to develop a methodology for identifying feasible network opening locations that enable the permanent reconfiguration of meshed LV grids into radial topologies. This methodology must be practically applicable within the operational environment of Stedin and leverage available network data and current distribution network modelling tools. The proposed approach aims to minimise power losses while improving system reliability.

This objective is summarised in the following research question:

> *How can an automated distribution network reconfiguration method be developed to identify feasible opening locations in existing meshed LV grids that minimise power losses and improve system reliability?*

The following three research questions have been defined to aid in answering the main question:

1. How can meshed LV grids be modelled by leveraging Stedin's existing distribution network modelling tools?
2. What impact do circulating currents have on cable and distribution transformer power losses in meshed LV grids?

3. Which constraints must be considered when selecting feasible locations for network openings in meshed LV grids?
4. How can these constraints be integrated into an automated and systematic approach for identifying feasible network opening locations?

1.3. Outline

The remainder of this thesis is organised as follows. Chapter 2 provides background on distribution networks, circulating currents in meshed LV grids, applicable design criteria, and relevant literature on distribution network reconfiguration. Chapter 3 presents a modelling approach for meshed LV grids using existing tools and validates it through a realistic case study. Chapter 4 introduces a genetic algorithm–based optimisation approach for identifying feasible network openings, integrating optimisation logic with power flow simulations in a closed-loop framework. The performance of the proposed framework is evaluated against heuristic industry approaches. Finally, Chapter 5 summarises the main findings, presents directions for future research and provides practical recommendations.

2

Background and Context

This chapter provides the background for addressing the research questions by introducing key concepts, methodologies, and constraints relevant to meshed LV grids. It begins with an overview of distribution network characteristics in Section 2.1, establishing the context for Research Question 1. Subsequently, it examines circulating currents in meshed LV grids, which are central to Research Question 2. Section 2.2 reviews analytical methods used to assess circulating currents in meshed configurations.

Next, the practical constraints associated with identifying feasible locations for opening meshed LV grids are examined. Stedin's design principles assume that LV grids are designed for a minimum operational lifespan of 40 years without major expansions resulting from autonomous growth. These principles guide de-meshing decisions and are summarized as nine key criteria in Section 2.3, with detailed explanations provided in Sections 2.3.1 through 2.3.4. Together, these criteria form the basis for addressing Research Question 3.

Finally, Section 2.4 reviews literature on Distribution Network Reconfiguration (DNR) and associated methodologies. This establishes the basis for determining feasible opening locations in meshed LV grids, supporting Research Question 4 and contributing to the main research question.

2.1. Distribution Networks

The power system is a large interconnected network, facilitating the transmission of electricity from the generation source to the consumers [14], [15]. In this system, there is a distinction made between two functions: transport and distribution. At the transmission level, electricity is transported over long distances and in large quantities, primarily through overhead lines. To minimise losses, a high system voltage of 150 kV up to 400 kV is used. The transmission grid is operated by the Transmission System Operator (TSO), which in the Netherlands is TenneT.

At distribution level, electricity is progressively stepped down from transmission voltages to levels suitable for end-users. This hierarchical structure and the differentiation between the different grid levels is illustrated in Figure 2.1. The process begins at main distribution substations, where the DSO converts high transmission voltages to MV levels, usually between 10–66 kV. MV networks serve both transport and distribution functions across regional areas, and provide connections for larger industrial loads. From there, voltage is reduced further at transformer stations to 3–23 kV before reaching the LV level of about 400 V for residential and commercial consumers.

Compared to transmission systems, distribution networks exhibit significantly different electrical and operational characteristics. Key characteristics include:

- High resistance-to-reactance (R/X) ratio in underground cables,
- Unbalanced three-phase system,
- Configurations in radial, loop and meshed network structures,
- Stochastic load behavior.

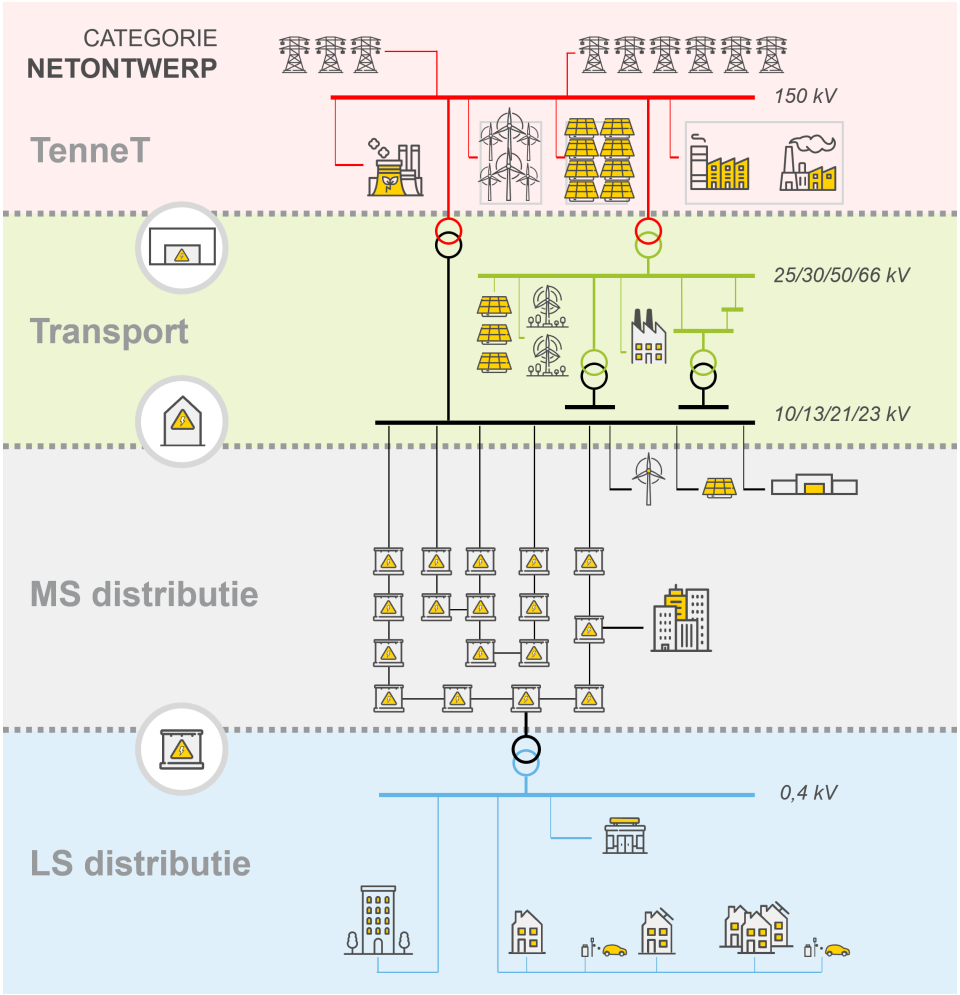

Figure 2.1: Hierarchical structure of the power system, illustrating the distinction between the transmission network operated by the TSO (TenneT in the Netherlands) and the distribution network operated by DSOs. Electrical energy is progressively transformed from transmission voltage levels to MV and LV levels for end-user supply.

2.1.1. Network Structure of Distribution Networks

The regional MV networks are configured in a loop or mesh structure with a normally open point [15]. This point, a load break switch, is closed only during faults to maintain continuity of supply. At the local LV level, distribution networks consist of interconnected secondary substations and consumers. A secondary substation typically includes an incoming line and multiple outgoing feeders connected to one or more buses.

The configuration of LV grids can be categorised into three distinct structures:

- **Radial network:** A radial network connects the secondary substation and consumer via a single connection. There are no switching options available.
- **Loop network:** A loop network connects the secondary substation and consumer via two paths.
- **Meshed network:** A meshed network provides multiple interconnected paths between secondary substations and consumers.

An example of a meshed LV grid is provided in Figure 2.2. In the figure, the black squares represent secondary substations with multiple supply paths to households. In the Netherlands, both loop and meshed networks are typically operated radially, with normally open points closed only during faults. However, some older urban areas still operate LV grids in a true meshed configuration. Within Stedin's service area (excluding Zeeland), approximately 53% of LV grids are configured and operated as meshed LV grids in 2025, as illustrated in Figure 1.1.

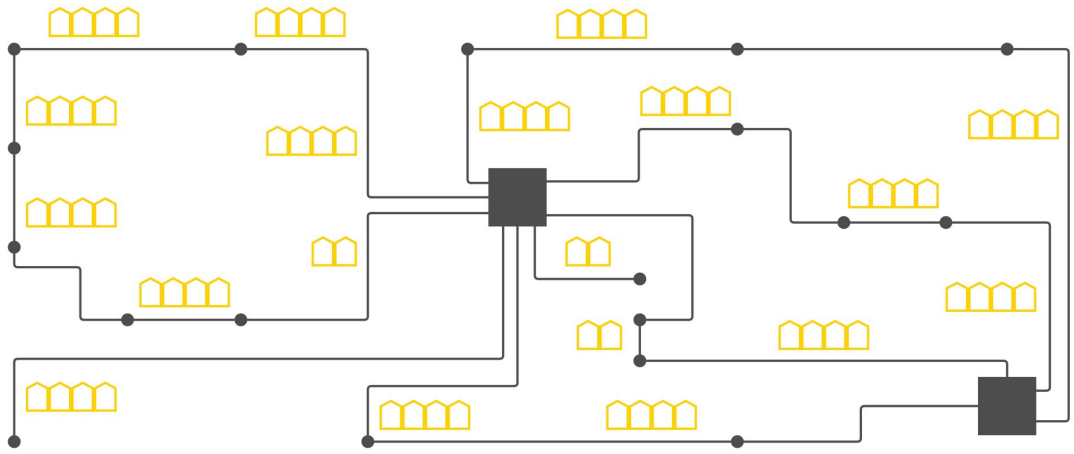

Figure 2.2: Schematic of meshed LV grid, in which the black squares represent secondary substations with multiple supply paths to households. Adapted from [15].

Meshed network structures offer several advantages. They have the potential to accommodate more DG and are considered a superior choice in terms of the diffusion of DG [6], [7], [8]. Besides, this network structure provides a more uniform power flow, improving voltage profiles, reducing losses, balancing loads and decreasing exploitation of lines and transformers. The presence of multiple supply paths between sources and consumers also enhances network reliability under normal operating conditions.

These advantages are accompanied by significant operational and protection-related challenges. In meshed networks, fault currents can flow from multiple directions, resulting in higher short-circuit current levels and complicating protection selectivity [9]. Protection coordination in meshed networks is therefore more complex and costly, reducing the effectiveness of fault localization and isolation and increasing the risk of widespread outages. Voltage regulation becomes more complex, requiring careful planning and control. Moreover, mismatches in transformer tap settings can lead to circulating currents within the network, increasing exploitation of lines and transformers without contributing to useful power delivery [10], [11].

2.1.2. Unbalance Effects

Although transmission systems are generally designed to operate under balanced conditions, distribution networks often experience significant imbalances due to several factors [15], [16], [17]:

1. Uneven allocation of single-phase loads across the three phases.
2. The occurrence of asymmetrical faults.
3. Stochastic load behavior.

Such situations result in what is known as an unbalanced three-phase system, in which the phase voltages or currents differ in magnitude or phase angle, leading to asymmetrical operating conditions. This introduces unwanted neutral or ground currents, increases losses and reduces overall efficiency. A further consequence is the ineffective use of network capacity, because once capacity on the most heavily loaded phase is used up, the unused capacity on the other phases cannot be utilized to relieve the overload.

Phase unbalance in distribution networks therefore presents several operational challenges, including voltage instability, increased network losses, deterioration of power quality, reduced protection reliability, and reduced network efficiency. These effects often translate into higher operational costs.

2.1.3. LV Load Behavior

In LV grids, loads are characterised by asymmetry, non-linearity and stochastic behavior [18]. Stochastic load behavior refers to the variability in electricity consumption patterns among consumers and DG

units connected across the three phases. While customers exhibit certain group-level trends, they act independently at any given moment, causing real-time phase unbalance.

This behaviour is increasingly pronounced due to electrification and the integration of DG [16]. For instance, electric vehicle (EV) charging is strongly influenced by individual lifestyles, while PV generation and other renewable resources introduce intermittent and weather-dependent injections. As a result, load and generation patterns are no longer dominated by a single evening peak and phase unbalance can occur throughout the day. Capturing this stochastic and phase-dependent behaviour is therefore a key challenge in LV grid modelling.

Simultaneity

Historically, LV loads have been modelled using stochastic principles combined with the concept of simultaneity. The simultaneity factor, introduced in 1956 by Rusck, is based on the observation that the maximum load of individual consumers does not occur at the same time [15]. Consequently, the maximum load at a node is smaller than the sum of individual peak loads, an effect that is referred to as diversification.

In stochastic LV load models, individual loads are treated as independent stochastic variables, approximated by normal distributions. The simultaneity factor depends on network size and load homogeneity. For example, public lighting exhibits simultaneity factors close to unity, whereas residential loads show lower simultaneity, especially at remote nodes with few connected consumers. Near the substation, aggregation effects increase simultaneity as individual fluctuations average out.

However, the use of simultaneity factors in modeling has an important implication: the current entering a node is no longer equal to the sum of outgoing branch currents. Since simultaneity factors effectively scale aggregated loads rather than represent instantaneous power flows, Kirchhoff's Current Law (KCL) is no longer satisfied at a single time step. As a result, classical simultaneity-based models cannot be used to compute physically consistent voltages, currents and phase angles and are therefore unsuitable for analysing circulating currents or phase-coupled phenomena.

Strand-Axelsson Load Models

Building on Rusck's work, Strand-Axelsson load models were widely used for network planning, providing probabilistic peak-load estimates based on annual energy consumption [18]. While effective in historically demand-dominated LV grids, these models have become increasingly inadequate due to electrification and DG integration. Peak loads have increased, correlations between annual energy use and peak demand have weakened and relevant operating conditions now extend beyond traditional evening peak periods. Consequently, this modeling approach fails to capture modern LV grid behavior.

Gaussian Mixture Models

To address the challenges encountered with Strand-Axelsson models, Gaussian Mixture Models (GMMs) are used to represent stochastic load profiles [18]. GMMs model load profiles as a weighted combination of multiple truncated normal distributions.

GMMs can be constructed for aggregated consumer loads or individual appliances, such as heat pumps, EVs, PV systems. Temporal characteristics are incorporated using quarter-hour and monthly scaling factors, while correlations between appliances can be explicitly modelled. For example, PV systems often operate simultaneously across neighbouring households.

To translate stochastic profiles into electrical variables, Monte Carlo simulations aggregate deterministic power flow calculations, producing probabilistic distributions for voltages, currents and power flows.

Gaia LV Network Design from Phase-to-Phase provides the methodology for constructing GMMs, while DSOs use smart meter data from their own customers to create representative models through [12]:

1. **Data analysis:** Smart meter datasets are categorized into user groups (e.g., by contract type), creating anonymized profiles.
2. **Model generation:** GMMs are generated for each category using Gaia or Python scripts, ensuring statistical representativeness.
3. **Integration:** Each connection in Gaia's NetBuilder is assigned a corresponding GMM.

2.2. Circulating Current in Meshed LV Grids

As outlined in Section 2.1.1, meshed LV grids interconnect secondary substations and consumers through multiple supply paths. When secondary substations are supplied from different points of the same MV ring, small differences in voltage magnitude and phase inevitably arise due to voltage drops along the feeder. In MV networks, the R/X ratio typically ranges between 0.5 and 2, meaning that both active and reactive power flows influence the voltage drop along a feeder. These differences in voltage magnitude and phase angle induce circulating currents within meshed LV grids.

Additional sources of voltage imbalance may originate from the LV side. Mismatches in transformer types or tap positions can introduce further deviations in secondary voltages. However, the impact of mismatched transformer characteristics in meshed LV grids remains underexplored in literature. For example, the studies in [19], [7] include several transformers in their analysis, but assume identical LV secondary voltages across all substations. Similarly, widely used power flow algorithms for weakly meshed networks neglect the effect of unequal tap settings, despite their relevance for accurately representing network behavior [20]. The Fast Flexible Direct Weakly Meshed Power flow (FFDWMPF) method, for instance, simplifies the system by assuming a single distribution substation acting as the swing bus for all connected loads [21].

Circulating currents resulting from loop-closing operations have been extensively examined in [22], [23], [24], [25], [26]. Loop closing is commonly used to enable load transfer without interrupting supply. These currents, primarily driven by voltage difference across the loop closing switch, can be calculated using methods such as detailed power flow analysis, approximate formulas, or power flow superposition. While detailed analysis offers high accuracy, it is computationally intensive. Simplified methods, including the superposition approach, provide faster calculations with acceptable accuracy, making them practical for planning and operational studies.

2.2.1. Branch Currents in Meshed LV Grids

In single-loop distribution networks, branch currents can be decomposed into multiple components, each representing different influencing factors such as node current distribution, loop configuration, primary power transfer, and the influence of power electronic devices [10]. In their most compact form, branch currents can be represented as the superposition of the interior current and the transporting current.

The interior current reflects the intrinsic current flow driven by local conditions. It captures the effects of nodal load and generation, as well as the aggregated branch currents from other feeders connected to that node. In other words, it accounts for the inherent current flow caused by local injections and topology, independent of power transfer between substations.

The transporting current accounts for the component of branch current associated with power transfer across the loop. It further decomposes into the parallel current I_P, which is induced by the primary power flow along the MV feeder, and the circulating current I_C, which arises from mismatches in transformation ratios between interconnected secondary substations. These two components are illustrated in Figure 2.3.

The analytical expressions for the parallel and circulating current components are given by

$$\underline{I_P} = \frac{\underline{U_1} - \underline{U_2}}{kZ}, \text{and} \tag{2.1}$$

$$\underline{I_C} = \frac{\underline{U_H}}{k_1 Z} - \frac{\underline{U_H}}{k_2 Z}, \tag{2.2}$$

respectively. Here, k, k_1, and k_2 denote the respective transformation ratios, $\underline{U_H}$ is a reference MV-side voltage phasor, and Z is the line impedance. Underlined quantities represent complex phasors.

From Equation (2.1), the parallel current becomes zero when the left and right bus voltages are equal, i.e., $\underline{U_1} = \underline{U_2}$. Similarly, according to (2.2), the circulating current becomes zero when the two transformation ratios match, i.e., $k_1 = k_2$.

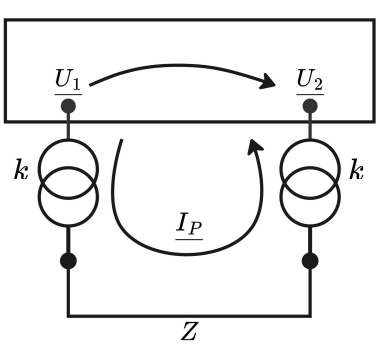

(a) Parallel current $\underline{I_P}$, is induced by the primary power flow along the MV feeder.

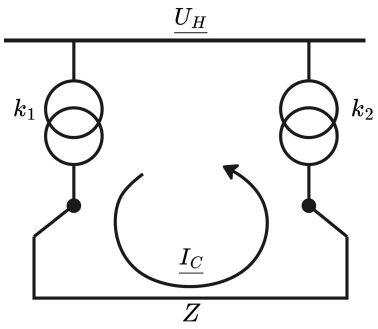

(b) Circulating current $\underline{I_C}$, arises from mismatches in transformation ratios between interconnected secondary substations.

Figure 2.3: Parallel and circulating current flow in a loop network. Adapted from [10].

2.2.2. Superposition Method

A closed-loop network can be represented as the superposition of two components: an open-loop network and an additional network containing a voltage source [11]. The open-loop network is formed by opening all loops of the original network while retaining all sources and nodal loads. The second component removes all sources, nodal loads and radial branches of the original network, but retains the branches that form loops and introduces a voltage source between the ends of the line connecting two distribution transformers. The magnitude of this additional voltage source in the closed-loop network equals the voltage difference between the two ends of the interconnecting line in the open-loop network. By superimposing the power flows of both networks, the power flow in the original closed-loop network can be determined.

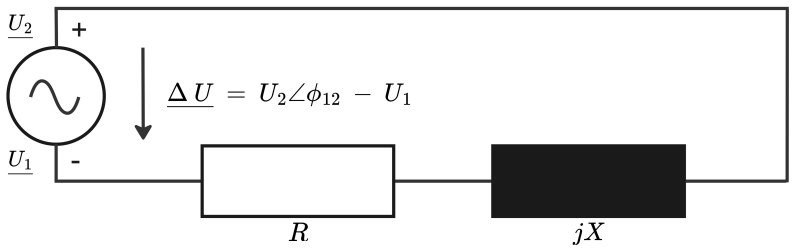

Figure 2.4: Equivalent circuit for calculating circulating current in a closed-loop network. Two distribution transformers are interconnected by a cable with impedance $Z_{eq} = R + jX$. A voltage source represents the voltage difference between the ends of this interconnecting line. Here, U_1 is a reference phasor and ϕ_{12} denotes the phase angle difference between the transformer voltages. Adapted from [11].

Assuming the system operates under balanced three-phase conditions, the analysis can be simplified to a single phase. Consider a closed-loop network with one cable interconnecting two distribution transformers, characterized by impedance $Z_{eq} = R + jX$. A voltage source represents the voltage difference between the two ends of this line, as shown in Figure 2.4. This voltage difference is given by

$$\underline{\Delta U} = U_2\angle\phi_{12} - U_1, \tag{2.3}$$

where $\underline{U_1}$ is chosen as the reference phasor with zero phase angle, i.e., $\underline{U_1} = U_1\angle 0$, and ϕ_{12} is the phase difference between $\underline{U_1}$ and $\underline{U_2}$.

Accordingly, the phasor $\underline{U_2}$ can be expressed in rectangular form as

$$\underline{U_2} = U_2 cos\phi_{12} + jU_2 sin\phi_{12}. \tag{2.4}$$

The resulting circulating current through the cable is determined by this voltage difference and the cable impedance and is given by

$$\underline{I_C} = \frac{U_2 cos\phi_{12} + jU_2 sin\phi_{12} - U_1}{R + jX}. \tag{2.5}$$

2.3. Design Criteria for Opening Meshed LV grids

The document *Ontwerp ontmazen laagspanningsnetten* provides design principles for opening meshed LV grids in different project contexts [27]. Its primary objective is to establish structure and consistency in the procedures required to de-mesh an LV network. These principles are partly derived from the design document *Ontwerp laagspanningsnetten*, which was developed for Stedin's LV grids. This design document assumes that LV grids are designed and constructed for a minimum operational lifespan of 40 years without the need for major expansions resulting from autonomous growth, as anticipated at the time of its publication in 2020 [28].

The design principles for opening meshed LV grids can be summarized in the following nine criteria:

Table 2.1: Design criteria applied by Stedin for opening meshed LV grids, adapted from [27].

ID	Description
R1	The maximum loading capacity of existing distribution transformers must not exceed 120%.
R2	The main cable may be loaded up to 100% of its nominal capacity.
R3	The maximum allowable voltage variation in the LV grid is 5%, with the maximum variation along the main cable being 4% and along the connection cable being 1%.
R4	The voltage at all consumer connections must be within the range of 207 V and 249 V.
R5	According to Article 7.8.1 of the Electricity Network Code, in designated risk areas, the touch voltage must not exceed 25 V. In the event of a fault causing the touch voltage to exceed 25 V, the system must be switched off within 5 seconds [3].
R6	According to Article 7.8.2 of the Electricity Network Code, in non-risk areas, the touch voltage must not exceed 50V. In the event of a fault causing the touch voltage to exceed 50 V, the system must be switched off within 5 seconds [3].
R7	According to Article 2.34 of the Electricity Network Code, the maximum permissible circuit impedance is specified as 283 mΩ [3].
R8	Fuses within the protection chain must be selective to ensure proper fault isolation.
R9	Stedin's policy mandates that all short circuits in the LV grid must be disconnected. The objective is to switch off short circuits within a maximum timeframe of 5 seconds.

The concepts of voltage variation, touch safety, circuit impedance and short circuit current, will be introduced in Sections 2.3.1 till 2.3.4.

2.3.1. Voltage Variation

The *Electricity Network Code*, established by the Ministry of Economic Affairs, defines regulatory requirements for voltage characteristics in Dutch electricity networks [3]. With respect to voltage characteristics, it supplements the European standard NEN-EN 50160, which specifies the voltage characteristics at any point of connection (the metering point) in public European electricity networks. International harmonization ensures appliance compatibility under these limits. DSOs are responsible for maintaining compliance, monitored by ACM: under normal operating conditions, supply voltage may not deviate more than $\pm 10\%$ from the nominal voltage U_n (230 V for LV grids).

The guideline *Ontwerp ontmazen laagspanningsnetten* prescribes stricter limits for LV grids: a maximum variation of 5%, subdivided as 4% along the main cable and 1% along the connection cable [27]. This does not change the overall $\pm 10\%$ limit but distributes it across network layers. The document *Ontwerp laagspanningsnetten*, which outlines design principles for new LV grids, confirms that the $\pm 10\%$ limit is divided between two network layers, assigning 5% to MV and 5% to LV grids [28].

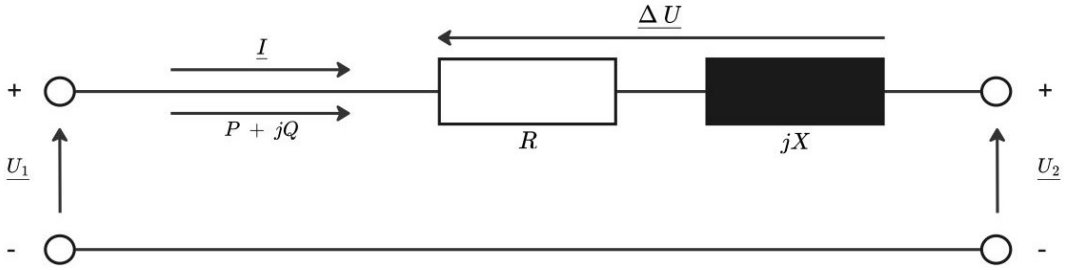

Figure 2.5: Simplified representation of a line section, with a bus at each end and a reference bus at the lower side. The feeder is characterized by an impedance $\underline{Z} = R + jX$ and the current $\underline{I}$, which results from the transfer of active and reactive power from the left to the right bus. Adapted from [15]

.

To explain the effect of voltage variations, consider the simplified line section in Figure 2.5, modeled as a series connection of a lumped resistance R and reactance X. Voltages $\underline{U_1}$ and $\underline{U_2}$ represent the phasor voltages at the sending and receiving bus, respectively.

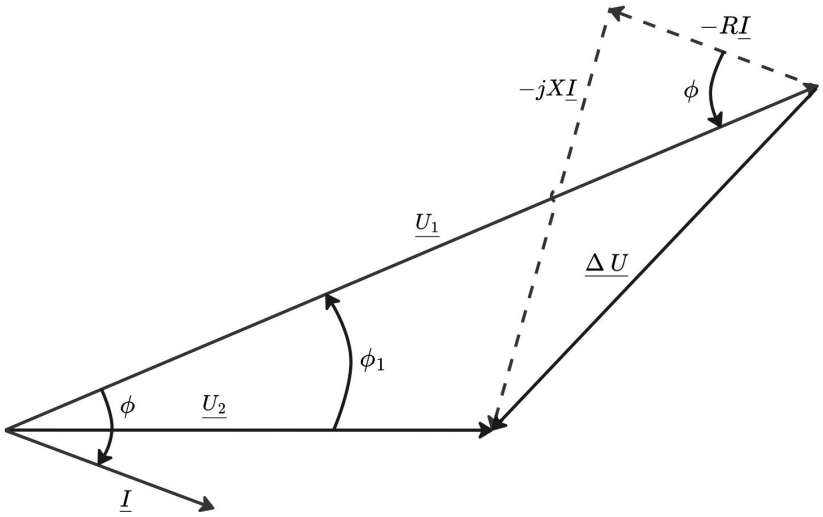

Figure 2.6: Phasor diagram of a simplified line section model, illustrating voltage phasors and their geometric construction based on the current phasor. Adapted from [15].

The voltage drop across the feeder depends on impedance and current $\underline{I}$, the voltage U_2 at the right bus can therefore be expressed by

$$\underline{U_2} = \underline{U_1} - (R + jX) \cdot \underline{I}. \tag{2.6}$$

Figure 2.6 shows that the voltage drop consists of two components: $-R\underline{I}$, which is parallel to the current phasor and $-X\underline{I}$, which is perpendicular to the current phasor. Using $S = U_1 \cdot I^*$, the voltage U_2 at the receiving bus can be expressed in terms of active power P and reactive power Q, following

$$\underline{U_2} = \underline{U_1} - \frac{(RP + XQ) + j(XP - RQ)}{\underline{U_1}}. \tag{2.7}$$

From Equation 2.7, it follows that voltage variation is influenced by the combined transfer of active power and reactive power. As the load increases, the voltage at the receiving bus U_2 decreases. Besides, fluctuations in the sending bus voltage U_1 are also observable at the feeder's receiving end.

The sensitivity of voltage to active and reactive power flows depends on the network's R/X ratio:

- In LV grids, the high R/X ratio ($R \gg X$) causes voltage variations to be predominantly driven by the transport of active power and the voltage angle by the transfer of reactive power.
- In MV networks, where $R/X \approx 1$, the voltage variation is approximately equally affected by the transfer of active and reactive power.
- In HV networks, the line resistance is negligible compared to reactance ($R \ll X$), so the voltage magnitude primarily depends on reactive power. Additionally, the difference between voltage angles is small, meaning the voltage angle is mainly determined by active power transport. This phenomenon is referred to as *decoupling* between active power and voltage angles and reactive power and voltage magnitudes [14].

2.3.2. Protection Against Electrical Shock

Safety requirements regarding protection against electric shock refer to the set of technical criteria that limit the permissible *touch voltage* during an earth fault. These requirements state that either the touch voltage must remain below the defined safety threshold, or, if this threshold is exceeded, the LV grid must be automatically disconnected within five seconds [15]. Failure to comply with these requirements can lead to hazardous situations, for example when a person or animal comes into contact with street lighting infrastructure that has become energised as a result of a fault. Consequently, touch-voltage safety is a critical design constraint for DSOs, particularly when selecting LV cable types and determining the maximum permissible lengths of LV cables.

The severity of electric shock depends on both the magnitude and duration of the current passing through the body. IEC 60479 specifies current-time hazard curves, while NEN 1010 outlines installation requirements. The current through the body is determined by touch voltage and body resistance, which vary with factors such as contact points and footwear. Statistical analyses have produced resistance-based curves. The 5% line, below which 95% of the population remains, is considered the safest and is therefore most commonly applied.

Safety assessment regarding protection against electric shock involves calculating fault voltage during a phase-to-earth short circuit and determining touch voltage using impedance division across the body, footwear and earth. Because body resistance changes with voltage, calculations are iterative. A key measure for limiting voltage rise is ensuring a low-impedance return path.

In Stedin's LV grids, two types of earthing systems are used [28], [27]:

- **TT system:** The original configuration, where the customer's earthing system is separate from the distribution network. Touch safety calculations by the DSO are not required for TT connections, because the customer is responsible for maintaining their own earth connection.
- **TN system:** Specifically, the TN-C system, combines the neutral conductor and the protective earth conductor into a single PEN conductor. In TN systems, the potential on the earthing system increases because neutral and protective earth conductors are interconnected at multiple points. A person touching an earthed device may therefore experience an elevated potential relative to the local earth. The DSO is responsible for maintaining the quality of the of earth connection to the connected party.

In 2022, ACM introduced stricter safety requirements and protection against electrical shock for LV grids built before April 2018, with compliance required by 2027 [2]. DSOs must prioritize adaptations where risk reduction is greatest.

2.3.3. Circuit Impedance

The network impedance at the point of connection indicates network strength. Circuit impedance requirements for LV grids aim to prevent flicker, the visible fluctuation in light intensity caused by rapid voltage variations [15]. Both individual customers and the network operator contribute to flicker through

their respective actions. The severity of flicker depends on network impedance: customers at the end of a feeder contribute more than those near the source, because higher impedance amplifies voltage fluctuations.

DSOs verify network strength through voltage stability calculations. Network impedance represents the total impedance from the source to the node and is derived from the voltage dip observed after applying a test load. This dip equals the sum of the voltage drops across the phase conductor and the return path. Since the circuit consists of both paths, the combined impedance $Z_{phase} + Z_{return}$ is referred to as the circuit impedance $Z_{circuit}$.

2.3.4. Short Circuit

A short-circuit fault places the electrical system in an abnormal operating condition and is critical because it can trigger switching actions, which often result in transient overvoltages [15]. Therefore, distribution networks must be designed and constructed to prevent hazardous situations following short-circuit faults, ensuring that neither people nor equipment are exposed to unacceptable risks. Appropriate protection devices and selectivity settings limit the impact by ensuring only the affected section is disconnected.

Short-circuit calculations verify whether protection devices disconnect faults within the required time and whether components can withstand short-circuit currents without damage. To evaluate if components are short-circuit proof, the maximum short-circuit current must be known. Its magnitude depends on the short-circuit power of the source, the impedance to the fault location and the fault type. For protection coordination and selectivity, the minimum short-circuit current is also critical.

Within Stedin, a policy is applied whereby all short circuits are cleared within five seconds at every point in the network, ensuring compliance safety requirements regarding protection against electrical shock [27]. If de-meshing causes disconnection times to exceed this limit, an assessment must be made to determine whether reducing the fuse rating is feasible. Large-scale network modifications fall outside the current operational strategy.

2.4. Distribution Network Reconfiguration

DNR involves making topological changes to a distribution network by operating normally closed and open switches to achieve specific operational or planning objectives [13]. Traditionally, DNR is applied to meshed distribution networks operated radially and reconfiguration can be performed in either static or dynamic modes. Unlike Dynamic DNR (DDNR), which operates in real time and prioritizes rapid computation to adapt to fluctuating conditions, Static DNR (SDNR) emphasizes accuracy and robustness, making it suitable for planning and operational strategies [9].

This thesis aims to identify feasible opening locations in a meshed LV grid to achieve a radial configuration. Accordingly, an optimization approach similar to SDNR is adopted, with three key distinctions:

1. The network initially operates in a meshed configuration.
2. Openings are permanent, reflecting long-term planning decisions rather than seasonal/yearly operational changes.
3. Openings are not restricted to load break switches. Lines within the distribution network can be disconnected or cut to achieve radiality.

The primary objectives of SDNR methods include reducing power losses, improving voltage profiles, balancing loads and enhancing network reliability, all of which align with sustainability and cost-efficiency goals. Most studies focus on power loss reduction and voltage profile improvement [16]. SDNR problems can be formulated as single-objective or multi-objective optimization tasks. Single-objective approaches typically target active power loss reduction, while multi-objective formulations address trade-offs among voltage stability, reliability and energy efficiency. In this thesis, the focus is on loss reduction, compliance with operational constraints and reliability improvement, motivating the adoption of a multi-objective SDNR approach.

From a methodological perspective, SDNR methods span four categories:

- **Classical approaches:** Mathematical programming and linearization, often limited by scalability and nonlinearity.
- **Heuristic methods:** Faster, but prone to local optima.
- **Metaheuristic methods:** Techniques such as Genetic Algorithms (GA), Particle Swarm Optimization (PSO) and Differential Evolution (DE) are widely used for their ability to handle complex, nonlinear problems without derivative information, offering near-global solutions.
- **Modern approaches:** Artificial Intelligence (AI) and Machine Learning (ML), including Artificial Neural Networks (ANN) and Reinforcement Learning (RL), enable adaptive and predictive capabilities, making them particularly relevant for smart grid applications.

DNR problems are mathematically classified as mixed-integer nonlinear programming (MINLP) problem due to their combination of discrete and continuous variables and non-convex solution space [29]. These characteristics make it highly challenging to solve DNR problems using exact or analytical optimization techniques.

Although modern optimization approaches, such as ML and RL, are among the fastest and most advanced methods, they also present a drawback: they require extensive training effort for larger networks with numerous variables. Since the objective in this work is to identify permanent network openings across many large and structurally diverse networks, rather than performing dynamic reconfiguration in real time, computational speed, adaptivity, and predictive capabilities are not the primary requirements. For this reason, metaheuristic methods are favored over learning-based approaches, as they offer a more suitable balance between flexibility, robustness, and solution quality for SDNR.

However, even metaheuristic algorithms, despite their flexibility, face difficulties when applied to large-scale MINLP problems because of their stochastic nature. Despite this, metaheuristic methods remain among the most commonly used approaches for SDNR due to their effectiveness in handling nonlinear optimization problems. These algorithms iteratively search for near-optimal solutions without relying on derivative information and are often inspired by biological or social behaviors. To improve computational efficiency and avoid premature convergence to local optima, numerous strategies have been proposed to reduce the search space and enhance algorithmic performance, some of which will be addressed in the following sections.

After presenting single- and multi-objective approaches in Sections 2.4.1 and 2.4.2, respectively, a comparative analysis will be provided based on case study results for a 33-bus distribution system reported in the literature. Finally, the potential application of graph theory will be explored to evaluate its suitability as a promising method for addressing the reconfiguration problem in Section 2.4.4.

2.4.1. Single-Objective Approaches

Single-objective formulations of SDNR typically aim to minimise active power losses while satisfying operational and radiality constraints. Several metaheuristic strategies have been proposed to address this problem efficiently.

For example, Adaptive Ant Colony Optimization (AACO) was proposed in [30] to solve the DNR problem. AACO introduces a graph-theoretic codification and rules that guarantee feasible radial configurations throughout the search process, eliminating mesh checks and reducing infeasible solutions. An heuristic spark (HS) accelerates convergence, while node voltages guide ant movement. The method can be extended to multi-objective formulations without significant computational overhead.

Similarly, [31] proposed a selective Firefly Algorithm combined with a heuristic based on the power flow Analysis Criterion (LFAC) to reduce the search space and improve computational efficiency. The method operates in two stages: mesh analysis identifies bus sets corresponding to network loops and LFAC ranks switches based on active power losses under meshed conditions, discarding less favorable candidates. This synergy significantly accelerates convergence while maintaining solution quality, showing strong potential for large networks, systems with DG and scenarios with varying operational constraints.

In [32], a heuristic-based approach determines an Initial Search Point (ISP) to enhance efficiency. The method temporarily closes each normally open switch, performs power flow analysis on the resulting meshed configuration and then opens the branch with the smallest loop current while maintaining radiality. This ISP is integrated into the initial population of a Continuous Genetic Algorithm (CGA), improving convergence speed and solution quality compared to random initialization or initial radial topology. Simulation results confirm its scalability and physics-informed design for complex distribution networks.

Another study, [29], proposes a methodology that leverages mesh analysis to significantly reduce the search space in the DNR problem. The proposed approach combines PSO with a heuristic that systematically analyzes network meshes. The process begins by identifying the switches that form system loops, as the number of meshes determines the minimum number of switches that must be opened to maintain radiality. By selecting switches from subsets most likely to be opened, guided by optimal power flow analysis, the method decreases the amount of candidates and reduces the search space. This targeted reduction enhances convergence and algorithm efficiency, reducing the average number of iterations by up to 80% depending on system size and complexity, while maintaining 100% accuracy in tests. Additionally, the approach improves computational time and ensures robust performance, making it a practical solution for optimizing feasible network openings in meshed LV grids.

As opposed to the aforementioned metaheuristic approaches, [33] introduces a ML-based approach approach for rapid microgrid reconfiguration. A trained neural network predicts the substation responsible for serving each part of the network, based on load and PV profiles, reducing computation time from 34.2 seconds to 1.54 seconds while maintaining over 95% accuracy. This demonstrates strong potential for real-time applications, with future work exploring graph NN for improved scalability and fairness.

2.4.2. Multi-Objective Approaches

Unlike single-objective formulations, multi-objective DNR problems aim to meet multiple objective simultaneously such as loss minimization, voltage profile improvement and reliability enhancement. Common techniques for handling trade-offs include weighted-sum optimization, fuzzy logic-based methods, or Pareto front approaches [13]. These methods enable simultaneous consideration of multiple objectives. An overview of metaheuristic-based multi-objective optimization methodologies for SDNR is presented in Table 2.4. Sections 2.4.2 to 2.4.2 briefly explain each approach, focusing on how they handle trade-offs between objectives.

Weighted-Sum Multi-Objective

[34] presents an advanced multi-objective optimization framework for DNR that simultaneously considers DG and ESS placement and sizing, while integrating dynamic network reconfiguration. The overall objective function combines active power loss P_{loss} and energy not supplied (ENS) using a weighted coefficient w:

$$\min\ OF = w \cdot P_{loss} + (1 - w) \cdot ENS \tag{2.8}$$

where $w \in [0, 1]$ and is set to 0.5 in the study. Priorities differ between connected mode (loss minimization) and islanded mode (ENS minimization).

The optimization is driven by the Adaptive Hybrid Intelligence Optimization (AHIO) algorithm, which combines metaheuristic global search, RL-based local refinement and gradient-assisted local search. Key innovations include adaptive search guided by RL, dynamic pruning of infeasible regions using real-time network constraints and parallelized power flow computation. These features enable faster convergence and higher solution quality. Additionally, the framework integrates uncertainty modeling for renewable generation and load profiles using probabilistic techniques and applies Information Gap Decision Theory for robust decision-making under uncertainty.

Fuzzy Multi-Objective Optimization

Fuzzy Multi-Objective Optimization (FMO) is a technique that incorporates fuzzy membership values and soft constraints to address multiple objectives simultaneously. FMO enables decision-makers to handle uncertainty and imprecision in optimization problems.

[16] introduces a multi-objective framework for managing DERs in unbalanced distribution grids under uncertainty. The approach minimises power losses, voltage deviations, operational costs and emissions using a customized three-phase power flow combined with a GA. GA was chosen for its robustness in handling complex, non-linear problems and demonstrated superior performance compared to PSO, despite slightly higher computation time.

Objectives are consolidated into a single fuzzy-based function, where each normalized objective is scaled to [0,1] and combined with equal weights for balanced evaluation. Normalization is defined as:

$$F_l = \begin{cases} 0 & \text{if } F_l \leq F_{l.min} \\ \frac{F_l - F_{l.min}}{F_{l.max} - F_{l.min}} & \text{if } F_{l.min} < F_l < F_{l.max} \\ 1 & \text{if } F_l > F_{l.max} \end{cases} \tag{2.9}$$

Similarly, [35] proposes a multi-objective framework for coordinating DG dispatch and EV charging under network constraints. Although not a DNR problem, the optimization approach is comparable. To address differing scales among objectives (neutral current, bus voltage, energy loss), each is converted into a fuzzy variable within [0,1] using a membership function similar to equation 2.9, ensuring negative values are clipped and maximum membership is limited to 1.

Pareto Optimal Multi-Objective

When objectives conflict, Pareto optimality provides a set of non-dominated solutions where improving one objective would degrade another. Pareto fronts offer practical insights for decision-making compared to single-point solutions.

[36] proposes an Enhanced Genetic Algorithm (EGA) for DNR that enforces radiality during genetic operations using a loop-based coding strategy. This ensures all individuals remain feasible without additional mesh checks. Reliability indices are incorporated in the evaluation process, enabling trade-offs between loss reduction and reliability via Pareto analysis. Results show EGA converges faster and with greater accuracy than conventional GA, reducing the percentage of infeasible solutions and improving computational efficiency.

Similarly, [37] introduces a Modified Gravitational Search Algorithm (MGSA) for radial and meshed networks, optimizing power loss, ENS and voltage stability index (VSI) under operational constraints. MGSA improves global search using a time-varying velocity mechanism to balance exploration and exploitation, preventing premature convergence and improving global search capability. Pareto optimality is applied with fuzzy normalization for multi-objective handling.

To evaluate Pareto optimality, fuzzy sets are implemented to scale each objective to [0,1], as adressed in Section 2.4.2. Then the normalized membership value for each member in the set of solutions is computed as:

$$N_{\mu j} = \frac{\sum_{k=1}^{n} \beta_k \, \mu_{jk}(x)}{\sum_{j=1}^{m} \sum_{k=1}^{n} \beta_k \, \mu_{jk}(x)} \tag{2.10}$$

where n and m are the number of non-dominated solutions and the number of objectives, respectively. β_k is the weight assigned to each objective, based on the importance of the corresponding objective function. The outcome is the best compromise among the non-dominated set. Tests demonstrate faster convergence and high accuracy, with Pareto solutions deviating only 2–3% from optimal values.

2.4.3. Comparative Analysis

33-Node System

The 33-node test system is widely used in the literature to evaluate and benchmark DNR methods. The single-line diagram of the system is shown in Figure 2.7. The base voltage is 12.66 kV and the base power is 10 MVA [38]. The system consists of 32 closed switches and 5 normally open switches. In its initial radial configuration, switches 33, 34, 35, 36, 37 are open. Under this initial configuration, the total active power loss and ENS are 202.6863 kW and 56217.06 kWh per year, respectively.

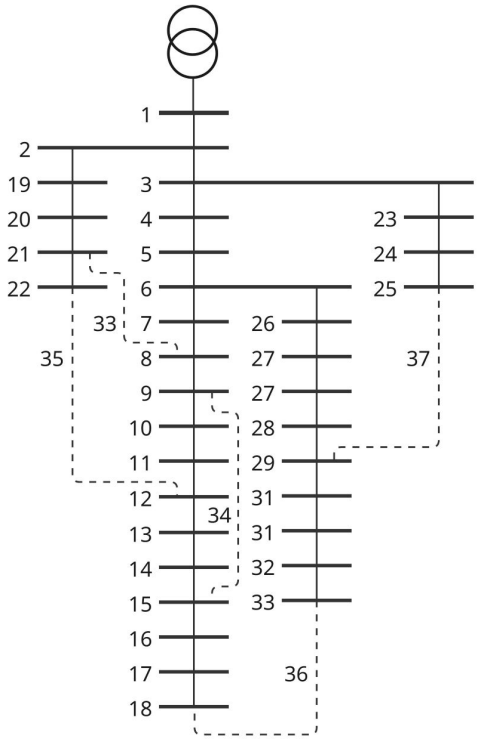

Figure 2.7: Single line diagram of IEEE 33 buses and 37 branches system. Adapted from [31]

Results

Table 2.2 summarizes case study results from literature for several SDNR methods applied to the 33-node distribution system. All studies aimed to minimise power losses and most achieved comparable reductions, except for AHIO [34], which stands out for two reasons. First, it is the only approach that uses a completely different set of operational switches, whereas [32] is the only other method that one different switch compared to others. Second, AHIO has by far the longest execution time, over 100 times slower than the fastest method, AACO [30]. Unfortunately, AACO is not inherently multi-objective, although the authors note it can be extended to handle multiple objectives without significant computational overhead.

Table 2.2: Comparative analysis of 33-node case study results for power loss minimization across SDNR methods.

Reference	Year	Power Loss (kW) Before SDNR	Power Loss (kW) After SDNR	Operational Switches	CPU Time (s)
AACO [30]	2011	202.68	139.55	7, 9, 14, 32, 37	0.30
EGA [36]	2015	210.99	139.55	7, 9, 14, 32, 37	5.06
Firefly [31]	2019	202.68	139.55	7, 9, 14, 32, 37	1.338
CGA using ISP [32]	2020	202.68	139.98	7, 9, 14, 28, 32	4.0147
MGSA [37]	2021	202.67	139.53	7, 9, 14 32, 37	1.56
EABCO [38]	2021	202.67	139.53	7, 9, 14, 32, 37	-
PSO with H-heuristic [29]	2021	208.43	138.97	7, 9, 14, 32, 37	3.71
AHIO [34]	2025	202.7	58	7, 11, 12, 17, 24	50

The objectives of meshed LV grid reconfiguration in this thesis are loss reduction, compliance with operational constraints, and reliability improvement. To this end, four studies that address both power loss minimization and reliability enhancement are again compared in Table 2.3. The table summarizes case study results for a 33-node distribution system, where all studies aimed to minimise Energy Not Supplied (ENS). Two studies by the same author [37], [38] report identical ENS reductions calculated

over one year. [36] does not specify the time horizon but achieves a slightly better relative reduction. Consistent with the power loss minimization results in Table 2.2, the AHIO method [34] again delivers the largest improvement of 74%, though calculated over a four-hour period.

Table 2.3: Comparative analysis of 33-node case study results for ENS minimization across SDNR methods

Reference	Year	ENS Before SDNR	ENS After SDNR	Operational Switches
EGA [36]	2015	3846 kWh	3302 kWh	10, 13, 16, 28, 33
MGSA [37]	2021	56217.06 kWh/year	53299.34 kWh/year	17, 19, 34, 35, 37
EABCO [38]	2021	56217.06 kWh/year	53299.34 kWh/year	17, 19, 34, 35, 37
AHIO [34]	2025	10.733 kWh	2.801 kWh	2, 18, 35, 13, 3

2.4.4. Graph-based Methods

Graph theory offers a powerful mathematical framework for modeling and analyzing distribution networks, making it a promising approach for determining permanent, feasible network openings. A distribution network can be represented as a graph where buses correspond to vertices and lines connecting the buses to edges [39]. This representation enables efficient handling of topological constraints and optimization tasks.

Several studies demonstrate the versatility of graph-based methods in power systems. For instance, [40] applies graph theory for fault location by decomposing the network into Y-shaped tree structures, improving mapping of operational data to fault locations. Similarly, [39] adapts Prim's algorithm to construct radial topologies based on system impedance rather than individual line weights. Besides, correction factors are introduced to minimise switching operations during restoration. Although effective, this approach requires pre-calculated correction factors, which vary by network characteristics.

Graph-based optimization has also been explored for determining the optimal switching path to minimise unpowered sections. [41] proposes a weighted graph model to determine the best decision considering cost functions, achieving rapid decision-making suitable for self-healing microgrids. Likewise, [42] leverages graph Laplacian properties and Dijkstra's algorithm to detect transitions between radial and weakly meshed configurations, reducing computational costs and ensuring accuracy and scalability for large networks.

Table 2.4: Review of multi-objective optimization methodologies for SDNR: reference, method type, optimization methodology, objectives and novelty.

Reference	Type of method	Optimization method	Objective functions	Main achievements
[16]	Metaheuristic	Genetic Algorithm	Power loss, voltage, cost, emissions	Uses probabilistic scenarios for uncertainty; adaptive search maintains diversity and accelerates convergence.
[34]	Metaheuristic	Adaptive Hybrid Intelligence Optimization	Power loss, ENS	Combines RL with adaptive search; prunes infeasible regions and parallelizes power flow.
[35]	Metaheuristic	Differential Evolution	Voltage balance, neutral current, average bus voltage, energy loss	Solves multiobjective optimization problem which jointly coordinates EV and DG to improve network performance; increases level of comfort of the EV user.
[36]	Metaheuristic	Enhanced Genetic Algorithm	Power loss, reliability	Improves GA crossover operator; eliminates mesh validation checks by enforcing radial topology; approach is applicable to meshed structures.
[37]	Metaheuristic	Modified Gravitational Search Algorithm	Power loss, ENS, VSI	Applies time-varying velocity to balance exploration and exploitation; prevents premature convergence; effective for single- and multi-objective DNR problems.
[38]	Metaheuristic	Enhanced Artificial Bee Colony Optimization	Power loss, ENS, emmision	Guides particles using the best solution to improve global search.

3

Meshed LV Grid Modelling

Modelling choices at each network level reflect trade-offs between model complexity and intended purpose. Greater detail improves the representation of network behaviour but increases development effort and computational cost. As a result, current LV grid representations do not fully capture circulating currents and their impact on cable and distribution transformer loading, which are a key characteristic of meshed LV grids. This chapter addresses this gap by proposing an integrated MV–LV network modelling approach and evaluating its ability to reproduce meshed grid behaviour.

Section 3.1 first outlines the current modelling practices and their underlying assumptions. It then discusses an integrated MV–LV network modelling approach that explicitly represents meshed LV grid behaviour while leveraging existing distribution network modelling tools, thereby adressing Research Question 1.

Section 3.2 validates the integrated MV–LV network modelling approach by applying the proposed method to a representative case study. The validity of the model is demonstrated by its ability to reproduce characteristic phenomena of meshed LV grids, including circulating currents, load sharing enabled by path diversity, and system responses to changes in distribution transformer tap settings. In doing so, this section adresses Research Question 2.

3.1. LV Grid Modelling

3.1.1. Current Modelling Practice of MV and LV Grids

Stedin separates the modelling of MV and LV grids. Each domain is represented in a dedicated software environment aligned with its analytical requirements. LV grids are modelled in Gaia LV Network Design from Phase-to-Phase (hereafter referred to as Gaia), which is specifically designed for the detailed design and analysis of LV grids. MV grids, by contrast, are represented in DIgSILENT PowerFactory (hereafter referred to as PowerFactory), which offers broader modelling capabilities and advanced analytical and automation tools.

LV grids are represented either as isolated radial grids or, for meshed LV grids, as weakly coupled grids. In the latter case, each secondary substation is modelled together with its directly connected neighbouring substations via LV mesh cables. However, connections beyond these immediate neighbours are not fully represented, as mesh cables extending further into the network are effectively truncated, with only half of each cable included in the model. Consequently, the full interconnectivity of meshed LV grids is simplified into a set of weakly coupled sub-grids

In this modelling approach, each secondary substation is assigned a dedicated, independent swing-bus. The stochastic, asymmetric, and nonlinear behaviour of LV loads and DG, described in Section 2.1.3, is modelled using Gaussian Mixture Models.

In MV grid models, networks are modelled per primary substation, with all outgoing MV feeders included in a single MV grid model supplied by a swing-bus connected to the primary side of the substation. Each

feeder supplies a set of distribution transformers, and the LV grids connected to these transformers are simplified into aggregated transformer loads.

The profiles of these aggregated transformer loads are constructed deterministically using annual customer consumption and generation data, combined with standardised profiles provided by Energie Data Services Nederland (EDSN) [43]. For radial LV grids, downstream LV loads can be directly aggregated at the supplying transformer. For meshed LV grids, loads connected to multiple substations via LV mesh cables are assigned to one of the supplying transformers based on their physical location.

3.1.2. Modelling Assumptions Affecting Meshed LV Grid Representation

Stedin's separation between MV and LV modelling environments is based on simplifying assumptions that keep each model fit for its intended purpose. The detailed analysis of power flow distribution in meshed LV grids falls outside the scope of these models, due to trade-offs between model complexity and analytical objectives.

While these assumptions enable accurate representation of power flow behaviour in radial LV grids and support planning-oriented analyses, they introduce limitations when the distribution of power flow in meshed LV grids is considered. In particular, the following assumptions in LV grid models restrict the assessment of meshed LV grid power flow:

1. **Secondary substations are modelled with independent swing buses**
   In weakly coupled LV grid models, each secondary substation is assigned an independent swing bus. This assumption neglects voltage magnitude and phase-angle differences between substations caused by voltage drops along the MV feeder. These differences are key drivers of circulating currents, alongside i.e. transformer tap settings, as discussed in Section 2.2. As a result, the model's ability to represent circulating currents and assess their impact on cable and distribution transformer loading is limited.

   Swing-bus voltage magnitudes could be adjusted to reflect MV-level conditions at a given instant. However, the corresponding phase-angle differences which contribute significantly to the reactive component of circulating currents in meshed LV grids remain unaccounted for. Moreover, extending such adjustments consistently over time (e.g., for daily or annual simulations) is not straightforward.

2. **LV loads are represented using stochastic modelling**
   This assumption affects the interpretability of power flow behaviour in meshed LV grids, particularly with respect to the identification of circulating currents. Customer demand and generation are represented using stochastic load modelling, as described in Section 2.1.3. This approach is well suited for planning studies, as it enables realistic estimation of asset loading levels.

   However, this modelling approach is not intended to provide a fully physically consistent power flow formulation in the simulation output. Individual load variations dominate at sparsely connected nodes, while increased aggregation near substations is captured through the use of simultaneity factors. Local variations in these simultaneity factors may lead to situations where the simulated current entering a node does not equal the algebraic sum of downstream branch currents. As a result, while suitable for planning purposes, this modelling approach limits the assessment of power flow distribution in meshed LV grids, which requires a physically consistent interpretation of power flow results.

Additional simplifying assumptions arise when meshed LV grids are represented within MV grid models. These primarily affect the representation of active and reactive power at distribution transformers interconnected through LV mesh cables. As a result, meshed LV grid power flow behaviour is not accurately reflected in distribution transformer loading or MV cable loading. These assumptions continue the enumeration of identified limitations:

3. **LV demand and generation is aggregated into a single load per distribution transformer**
   In MV grid models, LV grids are represented by aggregated load profiles at distribution transformers. While this is adequate for radial LV grid operation, this neglects the path diversity of meshed LV grids, where loads can be supplied via multiple parallel paths.

As a result, load sharing between transformers is represented as a fixed allocation in the model, whereas in reality it varies with operating conditions and may become more balanced due to meshing [6]. Consequently, this simplification limits the accurate representation of active and reactive power flows to and from distribution transformers, as well as their temporal variability.

4. **Electrical dependencies between distribution transformers via the LV grid are neglected** Due to load aggregation, the current MV grid models do not capture power flow interactions between distribution transformers through LV mesh cables. Consequently, circulating currents cannot be represented, as their paths are omitted, nor their sensitivity to LV-side voltage differences between the ends of LV mesh cables.

   This results in under- or overestimation of active and reactive power flows to and from distribution transformers, and an underestimation of the total power exchanged with the meshed LV grid.

Together, these assumptions explain why existing MV and LV grid representations are not able to fully capture the power flow behaviour of meshed LV grids, motivating the development of an alternative yet practically applicable modelling approach.

3.1.3. Deterministic LV Load Modelling

Among the modelling assumptions discussed in Section 3.1.2, a key similarity between the MV and LV domains concerns the modelling of consumer loads. In both domains, deterministic load profiles at the level of individual consumers are not directly available. This results in distinct but related limitations. At the LV level, the use of stochastic load modelling limits a physically consistent interpretation of power flow results. At the MV level, transformer load profiles must be disaggregated over individual LV connections along meshed LV feeders to adequately capture the effects of path diversity and the resulting circulating current in LV mesh cables. To address this, this section describes the construction of deterministic, single-consumer LV load and generation profiles.

The unavailability of deterministic load profiles at the individual consumer level is primarily driven by privacy constraints, which prevent direct access to smart meter data. For grid planning and design purposes, only aggregated annual consumption values derived from smart meters are used, in order to safeguard consumer privacy. Consequently, hourly-resolution deterministic load profiles for individual consumers are not available, necessitating the use of alternative data sources or modelling approaches.

The *London* dataset [44] offers half hour household consumption data from before large-scale PV adoption (2011-2014), making it suitable for reconstructing pure consumption patterns. However, differences in climate, building characteristics, and user behaviour limit its representativeness for Dutch households. The *Zonnedael* dataset [45], published by Liander, contains 15-minute consumption data for about 80 Dutch households from that same period (2012–2014) and is geographically more relevant. Its small sample size, however, is insufficient for representing the diversity of customers typically supplied by a secondary substation within Stedin's service area.

Given the constraints of the two datasets, this thesis adopts standardised profile fractions published by EDSN [43] to construct deterministic load and generation profiles. These standardised profiles provide an estimate of electricity consumption and infeed patterns based on historical meter readings reported by energy suppliers and DSOs, and therefore represent a statistically representative temporal distribution of demand and generation. This approach is aligned with current MV grid modelling practices, where MV load profiles are likewise generated by combining annual consumption data with EDSN time-based fractions.

Hourly deterministic profiles are constructed using each consumer's standard annual consumption (SAC) and standard annual feed-in (SAFI). In addition to these annual values, the following information is required for each connection: the network trace (i.e. the assigned feeding distribution transformer), the grid-area European Article Numbering (EAN) code and the EDSN standardised profile category.

The combination of grid-area EAN code and profile category determines the applicable EDSN standardised profile fractions for consumption and feed-in, which are subsequently scaled by the consumer's SAC and SAFI, respectively. Depending on the time of day and the season, positive profile values may occur in both energy-flow directions. To illustrate these profiles, Figure 3.1 shows hourly profile fractions for the standard consumption categories E1A, E1B, E2A, and E2B for a winter day.

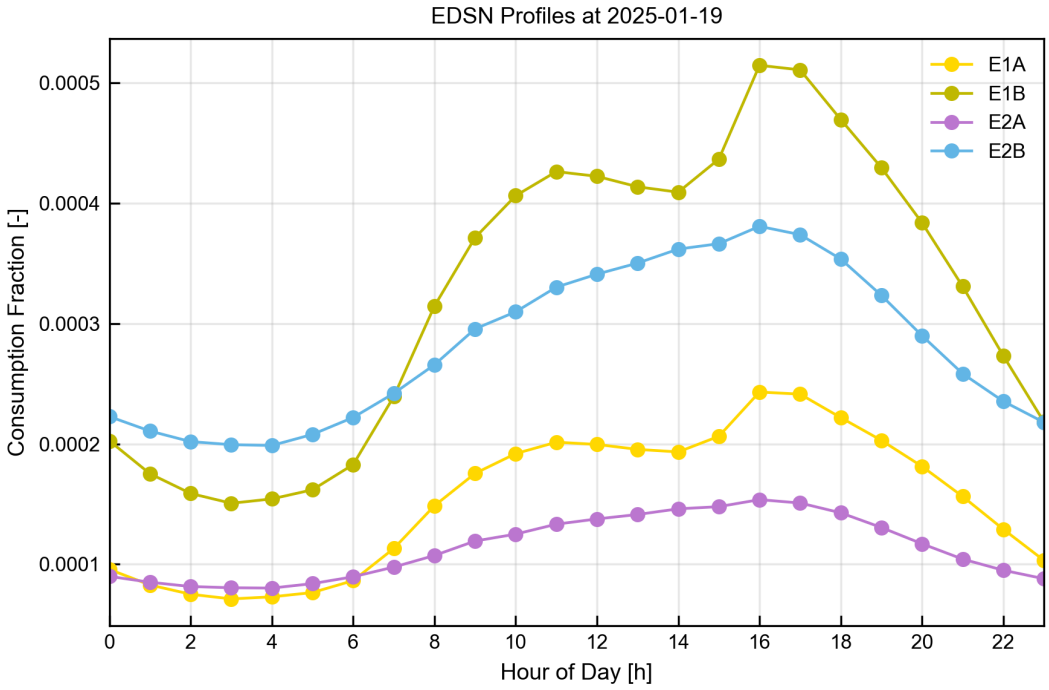

Figure 3.1: Hourly EDSN standard consumption profile fractions for categories E1A, E1B, E2A, and E2B on 19 January 2025.

3.1.4. Evaluation of Candidate Modelling Strategies

Several modelling strategies were evaluated to improve the representation of power flow distribution in meshed LV grids, while making use of existing distribution network modelling tools and available measurement data.

These strategies were assessed based on their ability to address the modelling assumptions that limit the representation of power flow distribution in meshed LV grids, identified in Section 3.1.2. These limitations primarily result from trade-offs between model complexity and intended purpose. In addition, suitability for automated simulation execution and result extraction was considered, as this is required for the systematic identification of feasible network openings in relation to the main research question in Section 1.2.

A first strategy investigated the implementation of MV cables within LV grid models, addressing Assumption 1, combined with the assignment of deterministic LV load profiles to consumer connections (in Gaia v8.10.1) to enable deterministic *netbelasting* calculations and address Assumption 2. While this approach captures voltage magnitude and phase-angle differences between secondary substations along an MV feeder and allows for a more physically consistent interpretation of power flow results than stochastic modelling, several limitations restrict its practical applicability:

- In the GMM framework, a single consumer may simultaneously exhibit demand and generation behaviour, each with distinct characteristics (e.g. $\cos\phi = 0.98$ for demand and $\cos\phi = 1.0$ for generation). When using external profiles, only a single net profile can be assigned to a connection. Consequently, accurately representing combined demand and generation would require splitting each consumer connection into separate load and generation entities and assigning individual profiles to each. This would be labour intensive.
- *Netbelasting* with external deterministic profiles does not include phase angles in the output, preventing analysis of phase angle differences between primary sides of secondary substations.
- Phase-resolved voltages and currents are not reported. Only the most heavily loaded phase is provided.
- Automated execution with external deterministic profiles is not supported via the Gaia macro language nor its PyPtP interface (an open-source Python software development kit (SDK) developed

by Phase-to-Phase [46]).

- Computation times are substantially longer than quasi-dynamic (QD) simulations in PowerFactory, limiting suitability for iterative or optimisation-based workflows.
- Significant data filtering and alignment are required to assign each connection with a deterministic profile.

These limitations indicate that, in its current form, Gaia is not well suited for detailed deterministic analysis of power flow distribution in meshed LV grids, nor for automated simulation execution and result extraction within this context.

Such limitations in commercial power system software have motivated the development of the Power Grid Model [47], an open-source Python/C++ library for high-performance distribution grid calculations. While commercial tools offer powerful standalone applications with graphical user interfaces, they often lack user-friendly, well-documented APIs, are not fully cross-platform, and scale poorly in cloud environments. Conversely, many existing open-source solutions lack support for asymmetric load flow calculations and efficient parallelisation for large-scale or batch simulations.

The Power Grid Model aims to address these gaps and is expected to outperform existing solutions. It appears particularly promising for meshed LV grid modelling, as it enables seamless MV–LV integration, fast and automated computations, and compatibility with optimisation workflows via its Python interface. However, it does not meet the thesis project requirements, as it is not an established modelling tool within Stedin. Therefore, alternative strategies must be considered.

The Gaia-related limitations also affect the feasibility of a second strategy, *MV-LV co-simulation*. This approach aimed to iteratively couple the MV and LV modelling environments via Python: primary-side transformer voltages from the MV grid model are used as inputs to the LV model, while the resulting active and reactive power supplied by each distribution transformer is fed back into the MV grid model. In doing so, this strategy directly addresses Assumptions 1, 3, and 4. The approach leverages existing tools, supports automation, and could scale to larger networks.

While PowerFactory offers a robust Python interface enabling automated and iterative calculations on the MV side, a critical limitation was identified in the LV modelling domain. Neither the Gaia macro language nor its PyPtP interface [46] currently supports automated execution of deterministic power flow calculations. Consequently, fully automated MV–LV co-simulation is not feasible. In addition, the requirement for iterative convergence may introduce substantial computational cost, although this has not been explicitly assessed.

The potential use of field measurements from Smart Grid Terminals (SGTs) and Distribution Automatisation Boxes (DA3-boxes) was also assessed. SGTs are installed at secondary substations and measure the aggregated power flow at the transformer level. As such, they provide no information on voltages or currents per outgoing LV feeder and therefore offer no insight into load distribution or circulating currents within meshed LV grids.

DA3-boxes can measure feeder-level currents and voltages. However, their practical applicability is limited by sparse deployment and data availability. Consequently, neither SGT nor DA3-box data can be reliably used to validate or enhance deterministic meshed LV grid modelling.

In summary, none of the evaluated strategies provides a feasible solution for automated, physically consistent analysis of meshed LV grids within the available modelling tools. Therefore, a final candidate modelling strategy based solely on PowerFactory is introduced and discussed in the next section.

3.1.5. Integrated MV-LV Network Modelling Approach

Based on the evaluation presented in the previous section, an integrated MV–LV network modelling approach in PowerFactory is adopted as the modelling methodology for the remainder of this thesis. This approach explicitly represents the relevant sections of the meshed LV grid together with the MV feeder(s) supplying its distribution transformers, thereby addressing Assumptions 1 and 4. Distribution transformers connected to the same MV feeder but not electrically part of the meshed LV grid are retained in the model by assigning their original aggregated MV loads, as defined in the existing MV grid model. The MV feeder is supplied by a swing bus.

Within the LV grid, only the LV mesh cable is represented in detail, as it connects two distribution transformers in a closed-loop and governs meshed power flow behaviour such as circulating currents and load sharing between distribution transformers. Purely radial LV feeders are not modelled individually. Their loads are aggregated at distribution transformer level to preserve correct loading while limiting model complexity.

In line with this LV representation, deterministic LV load and generation profiles are included using an aggregation level matched to their electrical relevance, thereby adressing Assumption 3: radial-feeder loads at transformer level, and loads connected to the LV mesh cable aggregated per lateral. This preserves the load distribution along the LV mesh cable and enables realistic representation of power flow distribution and transformer and cable loading.

The resulting MV–LV network representation aligns closely with Stedin's current MV grid modelling practice, particularly with respect to the construction of transformer load profiles using EDSN fractions. Although the simplified LV representation is not suitable for detailed LV-level studies or highly accurate loss calculations, it is well suited for analysing meshed LV grid power flow behaviour and for assessing its impact on loading of the LV mesh cables, distribution transformers and MV cables.

3.2. Model Validation

This section applies the integrated MV–LV network modelling approach to a representative case study and validates the developed integrated MV-LV network model by assessing its ability to reproduce phenomena characteristic of meshed LV grids. The validation focuses on active and reactive power flows, the presence of circulating currents, load sharing enabled by path diversity, and system responses to changes in distribution transformer tap settings.

The MV-LV network model is benchmarked against the current MV grid model with aggregated MV loads, which serves as a reference representation lacking explicit LV grid topology. By comparing transformer-level power flows under identical operating conditions, the added analytical value of explicitly modelling the relevant parts of a meshed LV grid is demonstrated.

3.2.1. Case Study Description

The selected meshed LV grid consists of eight secondary substations, hereafter referred to as shortened anonymised identifiers (e.g. 'Substation 1' to 'Substation 8'), all supplied by a common MV feeder. While the MV feeder supplies additional secondary substations, those supply radial LV grids and their loads are aggregated at distribution transformer level, and are thus left out of further detailed analysis. A schematic representation of the meshed LV grid is shown in Figure 3.2. The MV feeder is indicated by red lines and the eleven LV cables forming loops in the network are highlighted in blue.

The MV feeder originates from a primary substation equipped with a 20 MVA YN$\triangle$11 transformer operating at a nominal line-to-line voltage of 10.5 kV. The secondary substations within the meshed section are equipped with distribution transformers rated between 200 kVA and 630 kVA. Most transformers have transformation ratios of either 10750/420 V or 10250/400 V and are operated with tap settings in the neutral position. An overview of the technical details of the distribution transformers is provided in Table 3.1.

Table 3.1: Technical details of distribution transformers installed at secondary substations part of the case study.

Secondary Substation	Transformer Type	Tap Setting	Vector Group
Substation 1	10750/420V 400kVA	3/5	DYN5
Substation 2	10750/420V 400kVA	3/5	DYN5
Substation 3	10250/400V 315kVA	3/5	DYN5
Substation 4	10250/400V 200kVA	3/5	DYN5
Substation 5	10250/400V 315kVA	3/5	DYN5
Substation 6	10750/420V 630kVA	3/5	DYN5
Substation 7	10250/400V 250kVA	3/5	DYN5
Substation 8	10250/398V 200kVA	2/3	DYN5

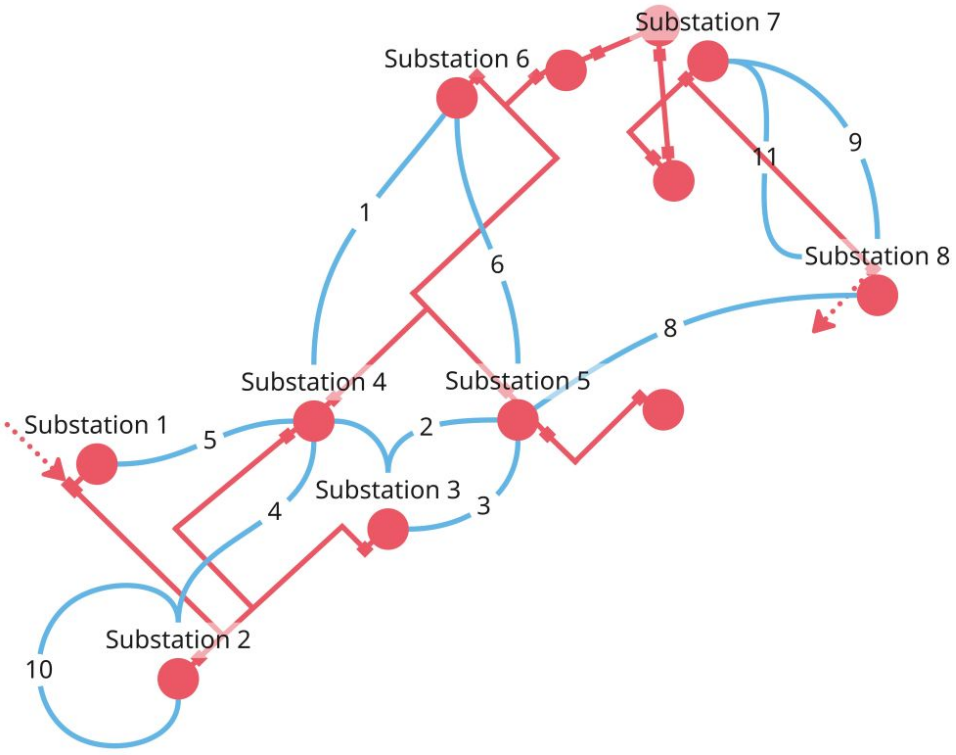

Figure 3.2: Schematic representation of the meshed LV grid containing 8 secondary substations (Substation 1-Substation 8) interconnected by eleven LV mesh cables. The MV feeder is indicated by red lines and the eleven LV cables forming loops in the network are highlighted in blue.

The meshed LV grid is located in an urban area characterised by a diverse mix of residential building types, including a substantial share of four-storey apartment blocks. Substation 1 is located most upstream along the MV feeder and supplies a mixed-use area with a combination of small commercial buildings and a limited number of residential households. Substation 6 represents another key node in the grid, supplying a predominantly commercial area that includes several supermarkets and retail facilities constructed in the 1960s, as well as adjacent apartment complexes. The comparatively high loading levels in this area justify the installation of a 630 kVA transformer, as indicated in Table 3.1.

The selected network constitutes a suitable case study due to its limited size, well-documented topology, and the availability of DA3 measurement units at three of the eight secondary substations. These measurements enable comparison and evaluation of candidate modelling strategies.

Load Profile Characteristics

The dataset used in this case study spans October 2024 to September 2025 and is constructed using EDSN profile fractions, following the approach described in Section 3.1.3. Consumption and generation are represented by separate component types to reflect their electrical behaviour. Consumption is modelled using a *General Load* component with a power factor of $\cos\phi = 0.98$, and PV generation is represented by a *Static Generator* operating at unity power factor. In both cases, time-series data are assigned via *Time Characteristics*.

3.2.2. Active and Reactive Power Relationship

Figure 3.3 shows that, unlike the aggregated MV grid model, the integrated MV–LV network model produces distinct operating points for each distribution transformer. In the MV grid model with aggregated MV loads, all loads lie on a single line in the P–Q plane due to the fixed power factor assumption ($\cos\phi = 0.98$), which enforces a constant ratio between active and reactive power.

In contrast, the integrated MV–LV network model reveals deviations from this linear relationship. Small voltage differences between distribution transformer secondary buses induce circulating currents in the

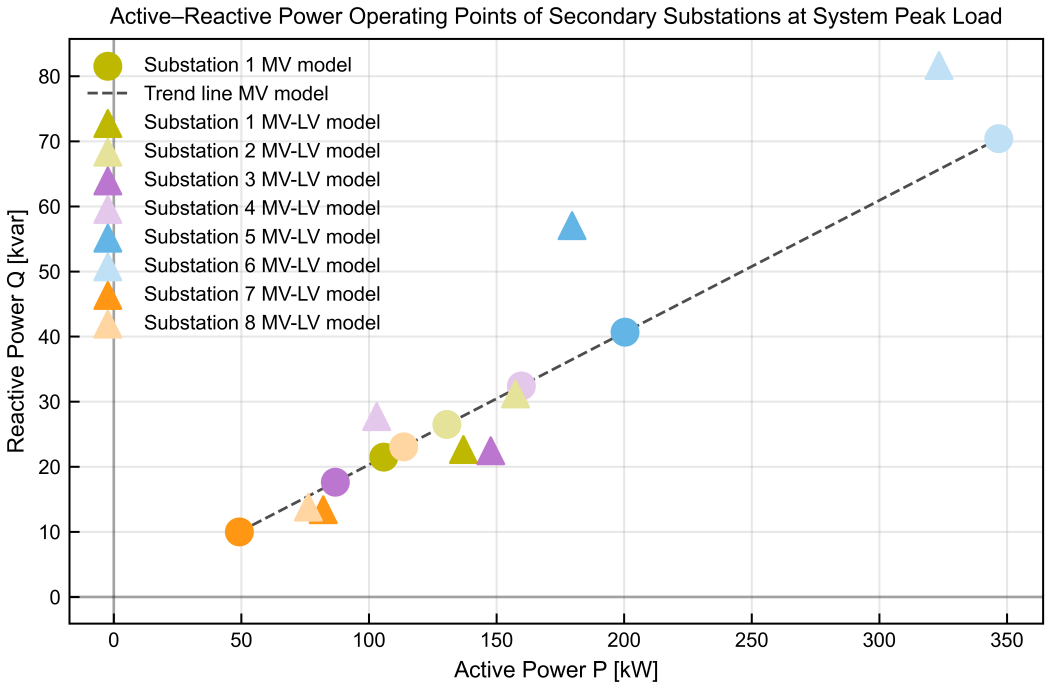

Figure 3.3: Active and reactive power flow at eight distribution transformers under system peak load conditions (19 January 2025, 16:00). Results from the MV grid model with aggregated MV loads (dots) are compared against the MV–LV network model incorporating a simplified LV topology to reproduce meshed network behaviour (triangles in matching colours).

meshed LV grid, causing some transformers to inject reactive power while others absorb it.

The effect is more pronounced when PV generation is high, shown in Figure 3.4. In the MV grid model with aggregated MV loads, excess PV generation appears as pure active power export ($\cos\phi = 1$) to the MV grid. In the integrated MV-LV network model, distribution transformers simultaneously exchange reactive power. For instance, Substation 4 exports active power to the MV network while absorbing reactive power, illustrating how the meshed LV grid redistributes both active and reactive flows in response to voltage differences at the secondary side of distribution transformers.

3.2.3. Path Diversity

Another key observation concerns the effect of path diversity in the meshed LV grid. In Figures 3.3 and 3.4, the eight distribution transformers in the integrated MV-LV network model share the total load or generation in different proportions than in the current MV grid model.

In the current MV grid model, each distribution transformer is assigned a fixed share of demand or generation due to load aggregation. In contrast, the integrated MV–LV network model explicitly represents parallel LV paths, allowing power to redistribute across the network. Consequently, distribution transformer shares vary over time with operating conditions.

3.2.4. Voltage Variability

While the integrated MV-LV network model enables assessment of the voltage profiles within the meshed section, it adopts a simplified representation of the upstream MV feeder infeed. The MV side bus of Substation 1 is supplied by an external grid with a fixed voltage magnitude.

In the current MV grid model, however, the voltage at this bus exhibits temporal variation due to changing operating conditions at the upstream primary substation supplying a wider network area. Recorded values exhibit a peak-to-peak variation of approximately 2%.

Because the integrated MV–LV network model assumes a constant infeed voltage, upstream fluctuations are not propagated to the LV grid, leading to an underestimation of voltage extrema. Consequently, the additional $\sim$2% MV-level variation is excluded from the simulations.

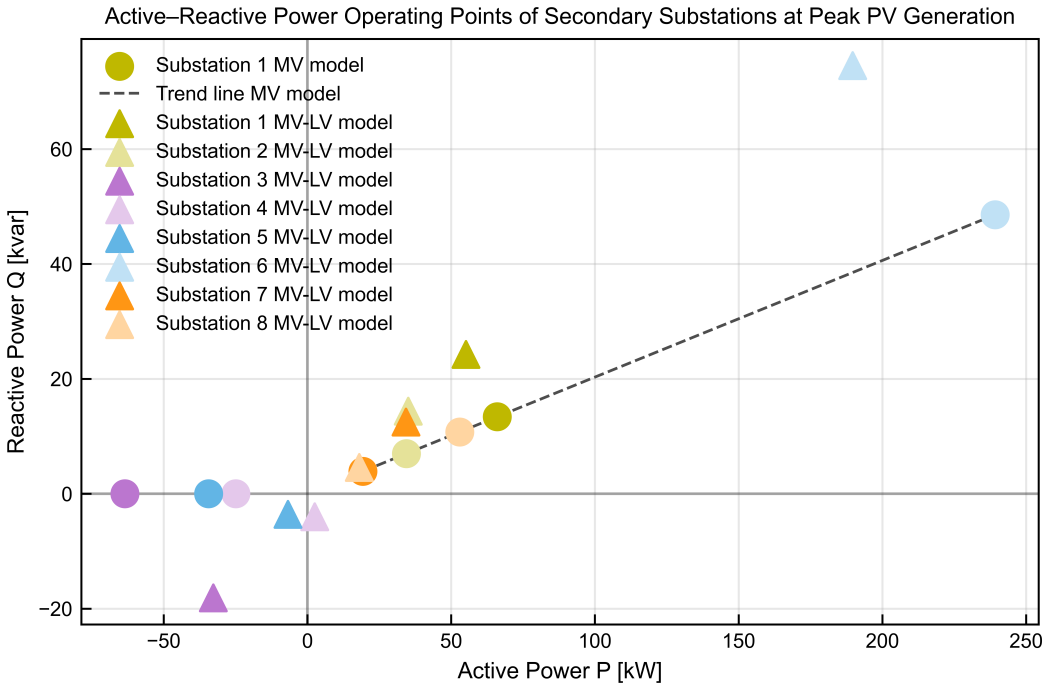

Figure 3.4: Active and reactive power flow at eight distribution transformers under system peak load conditions (29 April 2025, 11:00). Results the MV grid model with aggregated MV loads (dots) are compared against the MV–LV network model incorporating a simplified LV topology to reproduce meshed network behaviour (triangles, colour-matched per transformer).

The model is therefore well-suited for analysing spatial voltage profiles along LV mesh cables and their temporal variations, but it is not suitable for reliably assessing absolute voltage extrema in the LV grid.

3.2.5. Implications of Balanced Load Assumptions

As described in Section 3.1.5, the integrated MV–LV network model uses deterministic LV load and generation profiles aggregated at an electrically relevant level. While this preserves load distribution along LV mesh cables, it does not capture uneven phase allocation of single-phase loads.

In practice, such unequal allocation results in phase asymmetry, as discussed in Section 2.1.2. Since these effects are not represented, the model does not capture phase-specific loading. Consequently, it cannot reliably assess absolute current extremes, but remains suitable for analysing temporal loading patterns and power flow distribution.

3.2.6. Impact of Transformer Tap Changes

Deviations from optimal tap settings introduce voltage differences between the secondary sides of distribution transformers, which may arise in practice due to unknown or misconfigured tap positions. In meshed LV grids, these voltage differences across LV mesh cables drive circulating currents that do not supply local load, but increase asset loading and, consequently, power losses [10], [11].

To quantify these effects, the tap position of a single distribution transformer is varied by one and two steps, while all others remain at their neutral position. The resulting changes in total apparent, active, and reactive power at annual peak load, along with the corresponding annual losses, are summarized per secondary substation in Appendix E.1.

As an illustrative case, a one-step tap increase at Substations 1 and 3 is examined, corresponding to voltage changes of 2.32% and 2.44%, respectively. A higher tap position increases the transformation ratio,

$$t = \frac{U_{\mathrm{nom,prim}} + n \cdot \Delta V}{U_{\mathrm{nom,sec}}}, \tag{3.1}$$

where t is the transformation ratio, $U_{\text{nom,prim}}$ and $U_{\text{nom,sec}}$ are the nominal primary and secondary voltages, n is the tap position relative to neutral, and ΔV is the voltage step per tap.

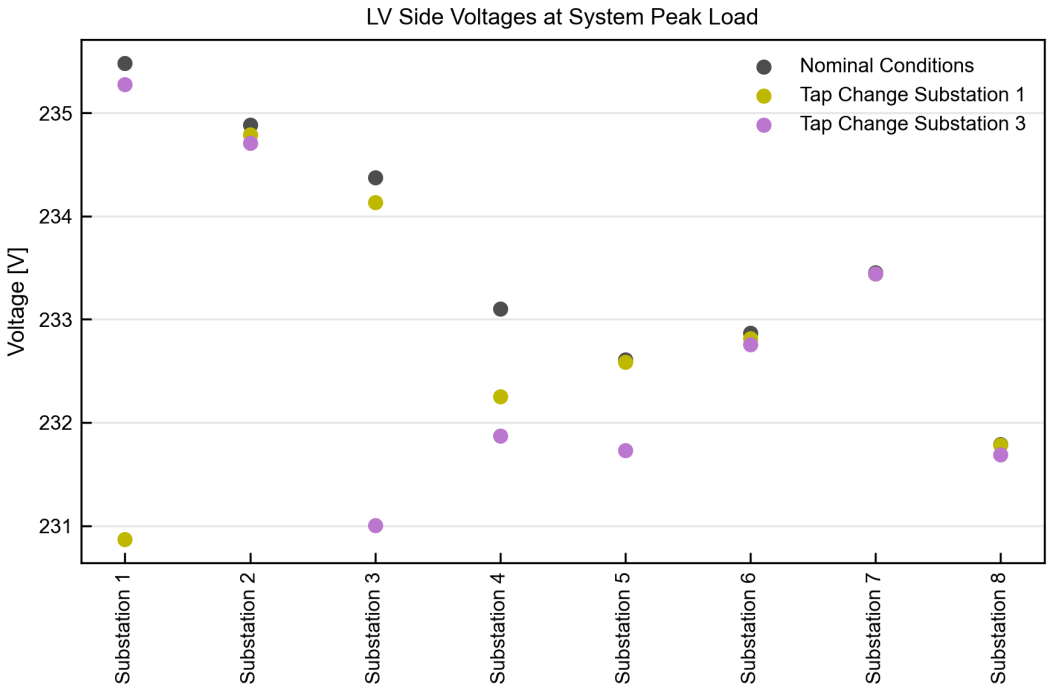

Figure 3.5: LV-side voltages of the eight distribution transformers (Substations 1-8) at annual peak load (19 January 2025, 16:00).

As shown in Figure 3.5, the increased tap setting reduces the LV-side voltages compared to nominal operating conditions. Consequently, voltage differences along the LV mesh cables increase. Due to the meshed topology, local tap changes propagate through the network via redistributed power flows.

For example, a tap change at Substation 1 interacts with Substation 4 via LV mesh cable 5 (Figure 3.2), introducing additional voltage differences along cables connecting Substation 4 to Substations 2, 3, and 6. This effect is particularly pronounced at Substation 3, which is interconnected with two neighbouring substations through three LV mesh cables. These interactions collectively shift the LV voltage profile and increase voltage differences across mesh cables, as shown in Figure 3.6.

Impact on System Power Exchange

Table 3.2: Total apparent, active, and reactive power at annual peak consumption are reported for nominal operating conditions, in which all distribution transformers operate at their nominal tap position, and for two scenarios with a one-step tap increase applied to a single distribution transformer while all remaining transformers retain their nominal tap settings.

Scenario	**Apparent power [MVA]**	**Active power [MW]**	**Reactive power [kvar]**
Nominal conditions	2.4267	2.3796	475.84
Substation 1	2.4277	2.3803	476.77
	(+0.034%)	(+0.028%)	(+0.194%)
Substation 3	2.4286	2.3811	478.01
	(+0.076%)	(+0.061%)	(+0.455%)

Circulating currents increase the total power exchanged with the meshed LV grid. Table E.1 summarises the apparent, active, and reactive power at system peak load.

Although apparent power increases in both scenarios, the relative change remains small since the source also supplies multiple substations along the MV feeder. However, reactive power increases

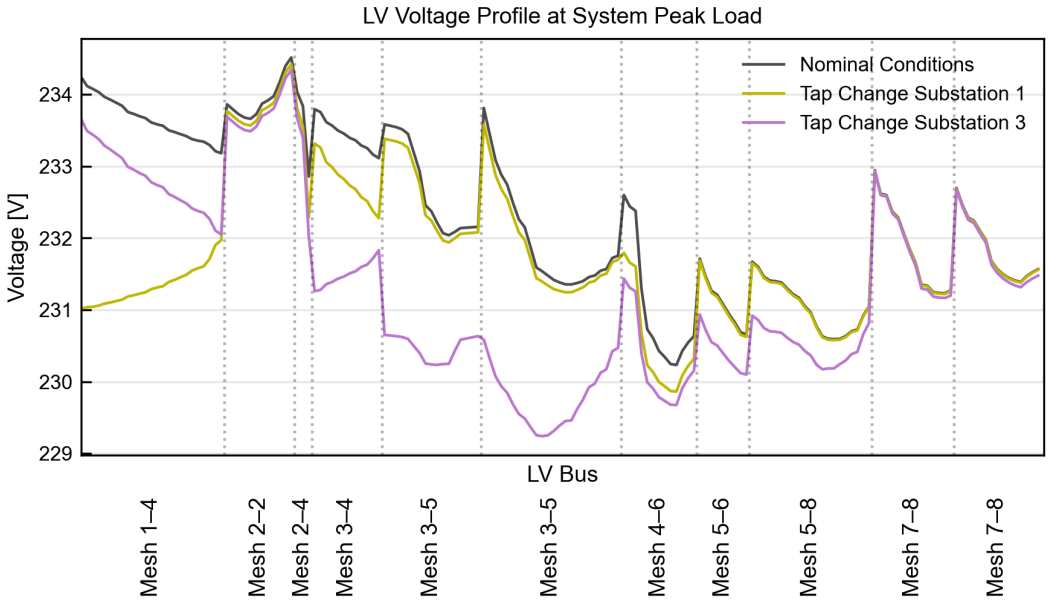

Figure 3.6: LV voltage profile along the 11 LV mesh cables (mesh x-x) at annual peak consumption (19 January 2025, 16:00).

more significantly than active power, reflecting stronger circulating currents and the high R/X ratio of LV cables, as discussed in Section 2.2.

Impact on System Losses

While the above effects are instantaneous, they accumulate over time as increased annual energy losses. Circulating currents raise current magnitudes in cables and distribution transformers, thereby increasing resistive and copper losses, respectively.

Table 3.3: Annual cable and transformer losses are reported for nominal operating conditions, in which all distribution transformers operate at their neutral tap position, and for scenarios with a one-step tap increase applied to a single distribution transformer while all remaining transformers retain their nominal tap settings.

Scenario	MV cable losses [MWh]	LV cable losses [MWh]	Transformer losses [MWh]
Nominal conditions	40.3	9.6	46.1
Substation 1	41.5 (+2.9%)	14.4 (+49.9%)	46.49 (+0.8%)
Substation 3	41.6 (+3.1%)	16.4 (+70.9%)	50.1 (+8.6%)

The annual energy loss is calculated as

$$E_{loss} = \sum_{t=0}^{T} \sum_{i=1}^{N} P_{loss,i,t}, \tag{3.2}$$

where N is the total number of components (MV/LV cables and distribution transformers), $P_{loss,i,t}$ is the active power loss of component i at time t, and T is the number of time steps in the QD simulation. The resulting annual energy losses are summarised in Table 3.3.

A tap change at Substation 1 mainly increases LV cable losses due to enhanced circulating currents, while distribution transformer losses remain nearly unchanged. In contrast, a tap change at Substation 3 increases both LV cable and distribution transformer losses, indicating stronger redistribution of power flows and higher maximum distribution transformer loading. In both cases, MV cable losses change only marginally compared to LV cable losses, reflecting the dominant impact of circulating currents within the LV grid.

Combined Interpretation and Implications for Meshed LV Grid Design

Tap-setting mismatches introduce voltage differences across LV mesh cables, which drive circulating currents. These currents increase asset loading and losses without contributing to local load supply. This effect is visible at the MV level as a disproportionate increase in reactive power exchange.

Since resistive losses in LV cables scale with the square of the current,

$$P_{\text{loss}} \propto I^2 R, \tag{3.3}$$

where P_{loss} are the resistive losses, I the current magnitude and R the resistance, even small mismatches can significantly increase active power losses. This is confirmed by the U-shaped relationship between tap deviations and LV cable losses in Figure 3.7a. In contrast, the impact on MV cable losses remains limited. Depending on the redistribution of power flows through the LV grid, these variations may result in either increases or reductions in losses, as illustrated in Figure 3.7b.

While LV cable losses increase substantially, by 68.8% to 140.6% for a one-step deviation and 235.4% to 525.0% for a two-step deviation, MV cable losses vary only between 0.7% and 5.0% (one-step) and 1.5% and 10.9% (two-step). The reported ranges are derived from the results presented in Appendix E.1.

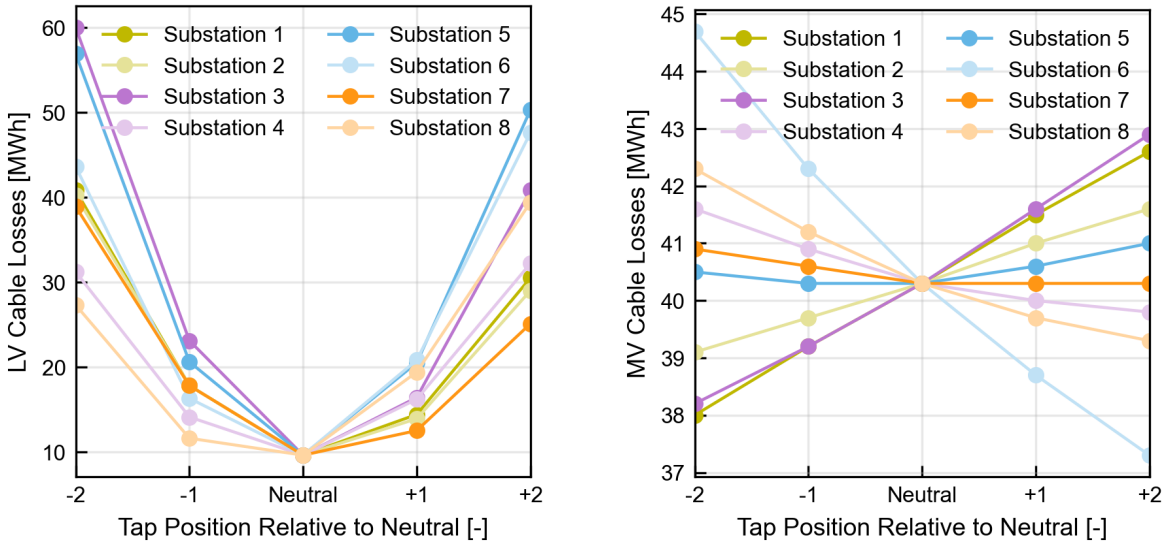

(a) Annual LV cable losses.

(b) Annual MV cable losses.

Figure 3.7: Annual cable losses resulting from one- and two-steps tap changes at a single distribution transformer, with all other transformers remain at their neutral tap position.

Transformer copper losses also follow a quadratic relationship with current given by Equation 3.3, but their relative increase remains moderate, ranging from 1.5% to 10.8% for a one-step deviation and from 5.2% to 43.0% for a two-step deviation. In absolute terms, however, this increase can still be significant due to the relatively high baseline losses under nominal operating conditions.

Overall, these results highlight the sensitivity of meshed LV grids to misalignment in transformer types and tap settings. Coordinated tap-setting strategies are therefore essential to limit circulating currents, minimise losses, and avoid inefficient utilisation of network capacity.

However, current modelling approaches tend to underestimate these effects due to simplified representations of meshed LV grids in both MV and LV models, as discussed in Sections 3.1.1 and 3.1.2. As a result, both active and reactive components of circulating currents are understated, and broader network interactions in meshed LV grids are not fully captured, highlighting the need for integrated MV-LV network modelling approach to accurately assess network capacity and efficiency.

4

Automatic Determination of Network Openings in Meshed LV grids

This chapter addresses the automatic identification of feasible network openings that enable the reconfiguration of meshed LV grids into radial configurations. Building on the integrated MV-LV network model developed in Chapter 3.1.1, a GA-based optimisation approach is introduced that explicitly accounts for relevant operational and topological constraints. The proposed method determines feasible opening locations that minimise network losses and voltage deviations, thereby directly addressing Research Questions 3 and 4.

The optimisation problem is characterised by a rapidly growing combinatorial complexity, driven by the number of meshed LV cables and the number of potential opening positions along each cable. For the case study network, comprising 11 fundamental loops, approximately 1.32×10^{13} configurations exist, making exhaustive search infeasible and manual identification impractical.

To overcome this challenge, Section 4.1 presents the GA-based optimisation approach for efficiently exploring the solution space while ensuring compliance with operational constraints. Sections 4.2 and 4.3 describe the simulation setup and the integration of the GA with quasi-dynamic (QD) simulations. Finally, Section 4.4 evaluates the proposed simulation-optimisation framework by comparing GA-optimised configurations with a reference configuration based on industrial de-meshing approaches.

4.1. Optimisation Approach

4.1.1. Genetic Algorithms

GAs form a class of metaheuristic optimisation methods commonly used for DNR. Inspired by natural evolution, they simulate processes such as reproduction, mutation, and survival of the fittest to iteratively improve a population of candidate solutions. Each solution is encoded as a *chromosome* composed of several *genes*, where each gene represents a decision variable. Through repeated application of evolutionary operators, the population evolves towards increasingly high-quality solutions [48].

Each individual is evaluated using a fitness (objective) function that reflects solution quality. Based on the fitness value, the algorithm selectively generates offspring solutions from the best-performing individuals while preserving sufficient diversity in the population to explore the search space effectively. This balance between exploitation of good solutions and exploration of new regions forms the core of the GA's global search capability.

Evolutionary Operators

In each iteration, referred to as an evolutionary cycle, evolutionary operators are applied to improve the population. These operators guide the search process by balancing exploitation of high-quality solutions and exploration of the solution space. The main operators are:

- **Selection**
  In each generation, individuals are selected based on their fitness value. According to the principle of survival of the fittest, solutions with higher fitness scores are selected to generate offspring solutions.
- **Crossover**
  Selected individuals (parents) undergo crossover, or recombination, to create offspring for the next generation. The genetic material from two parent solutions is recombined to create two new candidate solutions. This allows the GA to explore new combinations of parameters and potentially discover better solutions.
- **Mutation**
  Mutation introduces random modifications to one or more genes of the offspring. This is essential for maintaining genetic diversity, exploring new areas of the solution space, and reducing the risk of premature convergence to suboptimal solutions. Excessive mutation, however, transforms the process into a random search and diminishes the benefit of evolutionary learning.
- **Elitism**
  Elitism ensures that a predefined number of the best-performing individuals are preserved and passed unchanged to the next generation. This ensures that such well performing solutions are not being degraded when applying the crossover or mutation operators.

Over successive generations, these operators drive the population towards improved solutions while maintaining sufficient diversity. The algorithm converges when termination criteria are met, such as maximum number of generations or convergence of solution quality. The best individual in the final population is returned as the GA's best approximation of the global optimum.

Compared to other optimisation algorithms, GAs offer several advantages for DNR problems [32], [36]:

- **Ability to handle nonlinear objective functions:** GAs are well suited for optimization problems involving nonlinear objective functions, which are common in DNR. As discussed in Section 2.4, power flow equations and operational constraints create nonconvex optimisation landscapes.
- **Effective handling of discrete variables:** Switch states in DNR are inherently discrete. In this thesis, discretized line sections are switched in or out of service, a structure that GAs can handle directly without relaxation or reformulation.
- **Strong global search capability:** Through crossover and mutation, GAs explore a broad solution space and reduce the risk of premature convergence, making them effective for large-scale and topologically complex meshed LV grids.
- **Flexibility for multi-objective optimisation:** GAs support multi-objective formulations and constraint-handling strategies, enabling trade-offs between losses, voltage profiles, and asset loading.
- **Ease of implementation and adaptability:** GAs are straightforward to implement and integrate with QD simulations, facilitating rapid experimentation and adaptation to different network models and operating conditions.

4.1.2. Topological Description of the MV-LV Network

The meshed LV grid topology is represented as a directed graph with N_b buses (nodes) and N_e branches (edges), derived from the integrated MV-LV network model. To evaluate candidate opening locations, each LV mesh cable is discretised into branches, where LV load connection points are modelled as buses and intermediate cable sections as branches. Branch directions are inherited from the model.

Network connectivity is described by a bus-branch incidence matrix A of size $N_b \times N_e$, which contains one row per bus and one column per branch [49]. Its elements are defined as:

$$a_{ij} = \begin{cases} +1, & \text{if branch } E_j \text{ leaves bus } B_i, \\ -1, & \text{if branch } E_j \text{ enters bus } B_i, \\ 0, & \text{if branch } E_j \text{ is not incident to bus } B_i. \end{cases} \tag{4.1}$$

If a branch carries current from bus B_i to bus B_k, the corresponding column of A satisfies $a_{ij} = 1$ and $a_{kj} = -1$, with all other entries equal to zero.

A radial network satisfies $N_e = N_b - 1$, while in a meshed network the number of fundamental loops (FLs) is given by

$$L = N_e - (N_b - 1), \tag{4.2}$$

where N_b and N_e denote the total numbers of buses and branches, respectively [50].

4.1.3. Chromosome Representation

In the GA, each chromosome encodes a candidate network configuration by specifying which branches are opened to enforce a radial topology. A chromosome C consists of L genes, where L is equal to the number of FLs in the network as determined by Equation (4.2). This corresponds to the exact number of branches that must be opened to obtain a radial configuration.

A chromosome C encodes a network reconfiguration as

$$C = [c_1, c_2, \ldots, c_L], \tag{4.3}$$

where gene c_i selects the branch to open in the i-th loop [29], [31].

Each FL is represented as an ordered list of branch identifiers, defining the discrete search space. Since FLs may contain different numbers of LV branches, the loop representations have variable length.

For each loop, a corresponding binary mask vector M_i is constructed to represent the operational status of its branches. Each element m_{ij} indicates whether branch E_j in the i-th loop is in service (0) or out of service (1), according to

$$m_{ij} = \begin{cases} 1, & \text{if branch } E_j \text{ in the } i\text{-th loop is out of service,} \\ 0, & \text{if branch } E_j \text{ in the } i\text{-th loop is in service.} \end{cases} \tag{4.4}$$

Not all branches are admissible as control variables in the reconfiguration process. In particular, MV cables and distribution transformer branches are excluded by retaining only branches whose terminal buses both operate at the LV nominal line-to-line voltage (400 V). While prior studies [29], [31], [30] show that removing branches shared across multiple loops can accelerate the search, this filtering already achieves the maximum feasible reduction. In Stedin's meshed networks, only MV cables and transformer branches are shared across loops. Since these are excluded, no further reduction of the search space is possible.

4.1.4. Initialisation using an Initial Searching Point

Starting from high-quality, feasible initial solutions within the search space enhances the capability of the GA to identify near-optimal solutions and improves computational efficiency. Therefore, prior to executing the GA, all fundamental loops (FLs) are identified, after which an initial searching point (ISP) is determined by opening, in each loop, the branch with the smallest current magnitude, following [32]. The ISP is subsequently used to guide the generation of the initial population.

Minimum Spanning Tree

First, an MST of the integrated MV-LV network model is constructed to obtain an initial radial topology. The MST connects all buses without forming loops while minimising total branch weight. Standard algorithms such as Prim's or Kruskal's algorithm can be used for this purpose.

Kruskal's algorithm is adopted due to its efficiency on sparse graphs and straightforward implementation, as shown in Algorithm 1 [51]. Branch weights reflect network characteristics: LV branches are weighted by length, while MV cables and transformers receive small weights (i.e., below 1 meter) to prevent their removal. The branches excluded from the MST correspond to the FLs of the original meshed network and form the basis for subsequent loop analysis [50].

Although the MST is not mathematically unique due to equal weighing of MV and transformer branches and not necessarily distinct lengths of LV cable sections, the implementation is deterministic for a fixed

input. As Kruskal's algorithm iterates through branches sorted in ascending order of weight, different tie-breaking choices could, in principle, lead to different MSTs. However, for a fixed input, the implemented Python code consistently produces the same MST. This is because Python's sorting algorithm is stable and preserves the original insertion order for equal weights. Furthermore, for each pair of nodes, only the lowest-weight branch is retained, and in the case of equal weights, the branch with the smallest index is selected, thereby ensuring deterministic behavior.

Extraction of Fundamental Loops

Each excluded branch is processed by temporarily closing it, forming a topology with exactly one FL. The loop is identified using an iterative pruning procedure that removes first-order buses (nodes connected to a single branch) along with their incident branches, until only the loop remains. In the incidence matrix, such buses correspond to rows with a single nonzero element [52], [53].

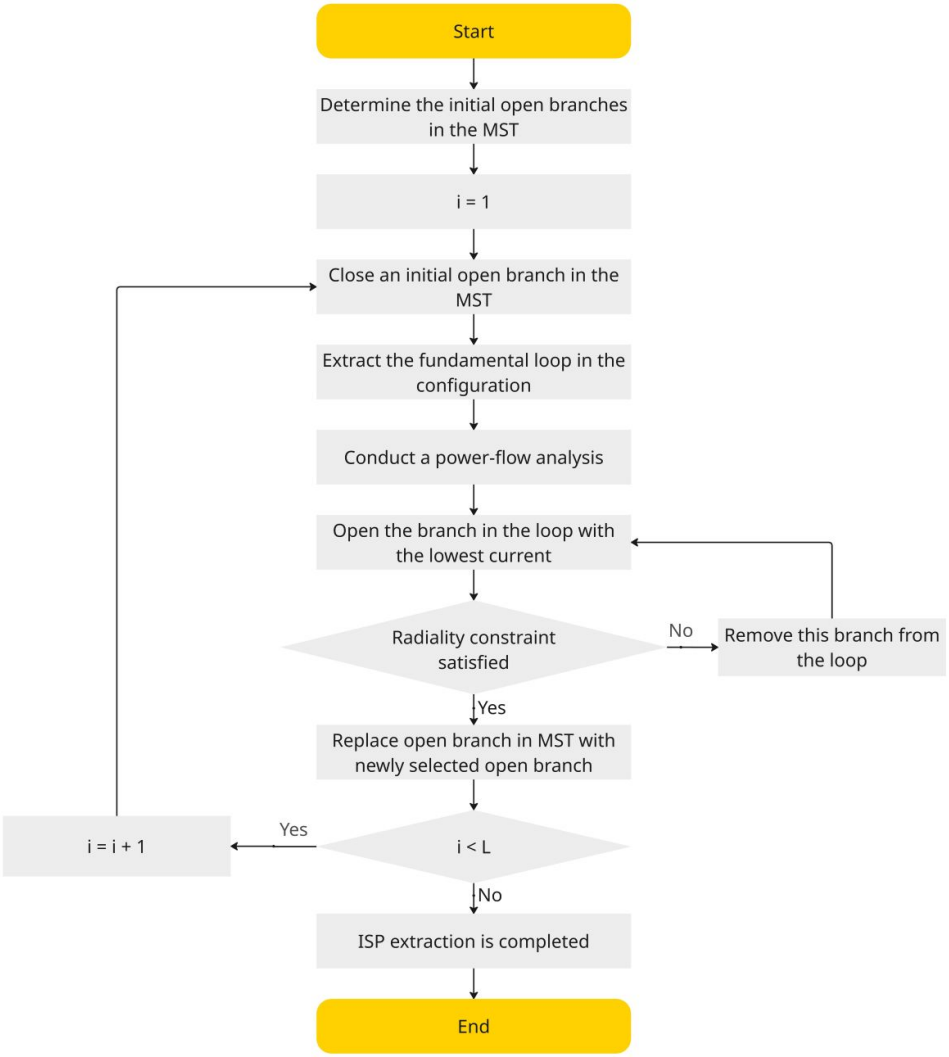

Figure 4.1: Flowchart for extracting the ISP used to generate the initial population of the GA. Following [32], low-current branches are opened to obtain a radial configuration.

Extracting an Initial Searching Point

For each extracted FL, the branch with the smallest current magnitude is selected as the candidate branch to open. Opening the branch with the lowest current generally results in lower power losses. Although one could compute the branch currents once for all loops, interactions between loops may alter current distributions and lead to suboptimal selections. Therefore, the ISP-extraction method evaluates each loop individually, following the concept introduced in [32]. However, unlike [32], which

assumes an initial radial topology with predefined open switches, the method is adapted here to operate directly on the MST obtained from the meshed LV grid.

The ISP extraction procedure is summarized as follows:

1. Determine the MST of the integrated MV-LV network model.
2. Temporarily close one open branch of the MST, forming a topology with exactly one closed loop.
3. Extract the corresponding FL.
4. Perform a power flow analysis.
5. Identify the branch in the closed loop with the smallest current magnitude and open this branch.
6. Verify whether the resulting topology is radial. If the radial constraint is satisfied, record the opened branch as part of the ISP. Otherwise, remove the candidate branch from the loop and return to Step 5.
7. Replace the original open branch in the MST with the newly selected open branch.
8. Repeat Steps 2-7 for each remaining FL in the distribution network.
9. Stop the algorithm once all FLs have been processed and their corresponding open branches have been determined.

The algorithm terminates once all FLs have been processed and a complete set of open branches defining the ISP has been obtained. A flowchart of the ISP procedure is shown in Figure 4.1.

4.1.5. Generation of the Initial Population

Previous studies [50], [54] employ different strategies to generate the initial population, each making use of available system information and heuristic methods to obtain efficient starting solutions. Similarly, this thesis uses FL information together with the ISP heuristic to construct a feasible radial topology with low losses, which serves as a baseline for initialisation.

In the proposed approach, the decision variables of each individual are initially set equal to those of the ISP solution. To introduce diversity, 50% of the variables are subsequently reassigned randomly within their feasible ranges. This hybrid strategy preserves guidance from the ISP while enabling exploration of the search space. Consequently, the population is more likely to start from feasible and relatively high-quality solutions, which can improve convergence performance.

However, this initialisation approach also limits population diversity. Since the population is not fully randomized, variability may be insufficient for thorough exploration of the solution space. As a result, the GA may exhibit reduced exploration capability, converge prematurely to suboptimal solutions, and face an increased risk of failing to approach the global optimum.

4.1.6. Generation of New Chromosomes

New chromosomes are generated through crossover and mutation. During crossover, genetic material from two randomly selected parent chromosomes is recombined to produce offspring solutions. From the available crossover operators, this work employs a guided multi-point crossover strategy [48], [54].

Genes that are identical in both parents are directly copied to the offspring. For the remaining genes, the offspring takes the selected branch either from Parent 1 or Parent 2, following an alternating pattern. This approach promotes diversity while preserving shared structural characteristics. An illustrative example of the guided multi-point crossover for a meshed network with six FLs is shown in Figure 4.2.

Mutation introduces additional diversity by randomly modifying a chromosome selected from the population. A mutation consists of selecting one or more genes and replacing the current branch index with a randomly chosen alternative within the valid range of the corresponding FL. This ensures feasibility of the resulting configuration while reducing the risk of premature convergence [48].

4.1.7. Chromosome Evaluation

QD simulations are employed to evaluate the time-dependent behavior of the meshed LV grid by combining elements of static and dynamic analysis. This approach assumes a sequence of steady-state

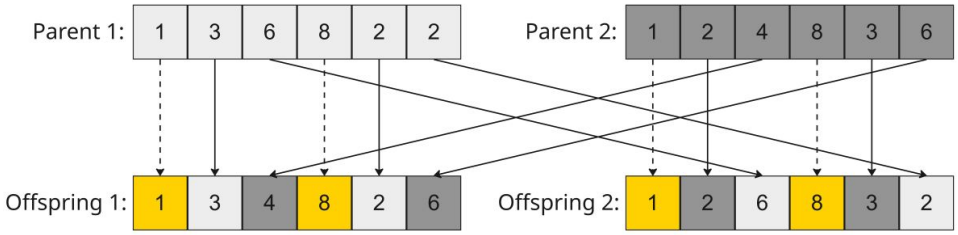

Figure 4.2: Guided multi-point crossover process. Equal genes are copied to the offspring (highlighted in yellow), while the remaining genes are inherited alternately from Parent 1 and Parent 2.

operating points and offers a computationally efficient approximation of system dynamics. As such, it is well suited for assessing the fitness of chromosomes generated by the GA.

The evaluation is performed over a discrete set of time steps consistent with the temporal resolution of the MV and LV load profiles. At each discrete time step, the system is assumed to be in quasi-equilibrium, and a static power flow analysis is carried out to compute the relevant electrical variables.

The primary objective of the reconfiguration problem considered in this study is to minimise the active power losses in the distribution network. The average active power loss function is expressed as

$$f = \frac{\sum_{t=0}^{T} \sum_{i=1}^{N_e} k_i P_{loss,i,t}}{T}, \tag{4.5}$$

where N_e denotes the total number of branches, $P_{loss,i,t}$ represents the active power loss of branch i at time t, and T is the total number of time steps (hours) evaluated in the QD simulation. The binary variable k_i indicates the operational status of each branch, where $k_i = 0$ if the branch is in service and $k_i = 1$ if the branch is out of service.

The optimisation problem is constrained by the operational requirements summarized in Table 4.1, which are derived from the design principles for opening meshed LV grids [27]. Constraints C1 and C2 are enforced as hard constraints, whereas constraints C3–C6 are treated as soft constraints. These soft constraints are incorporated into the multi-objective fitness function:

$$\text{fitness} = \lambda_f \cdot f + \lambda_d \cdot U_{drop} + \lambda_v \cdot \Delta U_{deviation} + \lambda_t \cdot u_{\text{transformer}} + \lambda_l \cdot u_{\text{cable}} \tag{4.6}$$

where:

- f is the average active power loss in the system, as formulated in Equation (4.5),
- U_{drop} is the maximum voltage drop along an LV feeder,
- $\Delta U_{deviation}$ is the system maximum absolute deviation from the nominal LV voltage,
- $u_{\text{transformer}}$ is the maximum transformer loading,
- u_{cable} is the maximum cable loading,
- λ_f, λ_v, λ_d, λ_t, λ_l are penalty coefficients enforcing compliance with operational limits.

Because the soft constraints differ in magnitude and units, each is normalized to the interval $[0, 1]$. This normalization ensures that all soft constraints contribute comparably to the overall fitness value, independent of their original scale. For constraints that must be minimised (e.g., voltage drop, maximum voltage, transformer loading, cable loading), the following normalization is applied

$$obj_{min}(norm) = \frac{obj - obj_{min}}{obj_{max} - obj_{min}}, \tag{4.7}$$

where obj_{min} and obj_{max} define lower and upper bounds of the normalization interval for a given objective, obj denotes the actual value, and $obj_{min}(norm)$ is the normalized objective value [49].

For constraints that must be maximized (e.g., minimum system voltage), the normalization becomes

$$obj_{max}(norm) = \frac{obj_{max} - obj}{obj_{max} - obj_{min}}, \tag{4.8}$$

where $obj_{max}(norm)$ is the normalized objective value.

Constraint C2 is satisified when the QD simulation is succesfully executed.

The penalty coefficients in the fitness function are set to:

$$\lambda_f = 0.5, \quad \lambda_d = 0.95, \quad \lambda_v = 1.25, \quad \lambda_t = 0.02, \quad \lambda_l = 0.01.$$

These coefficients reflect a balance between loss minimisation and constraint enforcement from a planning perspective. Voltage-related terms are assigned higher weights because voltage is treated as a primary design driver. While asset loading can be mitigated through reinforcement, such as upgrading cables or transformers, voltage issues are significantly harder to correct after implementation. For this reason, voltage deviations and drops are prioritised more strongly. In contrast, transformer and cable loading are treated as feasibility constraints and are assigned lower weights.

The weighting is calibrated relative to the normalised active power losses and supplemented by iterative tuning. As a baseline, a 1% reduction in losses is equally important as a 5% (or approximately 1 V) reduction in voltage deviation. The voltage drop exhibits a larger variation among solutions than voltage deviation. To account for this, voltage deviation is weighted more heavily than voltage drop. Both voltage-related weights were subsequently scaled down by a factor of two to prevent overemphasising voltage performance and maintain a balanced trade-off.

Finally, loading terms are assigned low weights. This ensures sufficient sensitivity to heavily loaded conditions while still allowing variability among feasible solutions.

Table 4.1: Operational constraints for radial LV grids, derived from the design principles for opening meshed LV grids [27].

ID	Description
C1	The network must operate radially, without isolating any buses.
C2	Power flow equations for distribution networks must be satisfied.
C3	The loading of existing distribution transformers must not exceed 120% of their rated capacity.
C4	The main cable may be loaded up to 100% of its nominal capacity.
C5	The voltage at all consumer connections must remain within the range of 207 V to 249 V.
C6	The maximum allowable voltage variation in the LV grids is 5%, with a maximum of 4% along the main cable and 1% along connection cables.

Radiality

To ensure compliance with Constraint C1 in Table 4.1, each feasible configuration must contain exactly one open branch per FL, thereby guaranteeing a radial network structure. Radiality is verified by constructing the bus-branch incidence matrix A of the candidate configuration. The column associated with the reference bus is then removed, resulting in a reduced square matrix of size $N_e \times N_e$. If the determinant of this reduced incidence matrix is equal to $+1$ or -1, the configuration is radial, while any other value indicates the presence of meshed loops in the network [49].

4.2. Simulation Setup

DIgSILENT PowerFactory (referred to as PowerFactory) is used as the modelling and simulation environment, as motivated in Section 3.1.5. It serves both as the repository for the integrated MV–LV network model and as the solver for QD simulations. Its Python API enables programmatic access to grid elements, including modifying network topology, switching lines in and out of service, and retrieving simulation outputs.

Python functions as the central orchestration environment of the framework due to its readability, flexibility, and extensive ecosystem of libraries. Through seamless integration with simulation software,

Python controls simulation execution, manages data exchange, processes results, and implements the optimisation algorithm.

The proposed closed-loop framework relies on bidirectional data exchange between Python and PowerFactory, similar to a method previously applied within Stedin [55]. As illustrated in Figure 4.3, Python transmits candidate sets of branches to be taken out of service to PowerFactory. In return, QD simulation results are provided, including active power losses, voltage magnitudes, cable loadings, and distribution transformer loadings, which are subsequently evaluated by the GA.

All scripting and optimisation were conducted using Python 3.13.9, employing *pandas* for data handling, *numpy* for numerical operations, and *matplotlib* for visualisation, in combination with the PowerFactory Python API. Simulations were performed using DIgSILENT PowerFactory 2025 SP3 (x64) and executed on a system equipped with an Intel® Core™ Ultra 7 165U processor operating at 1.70 GHz.

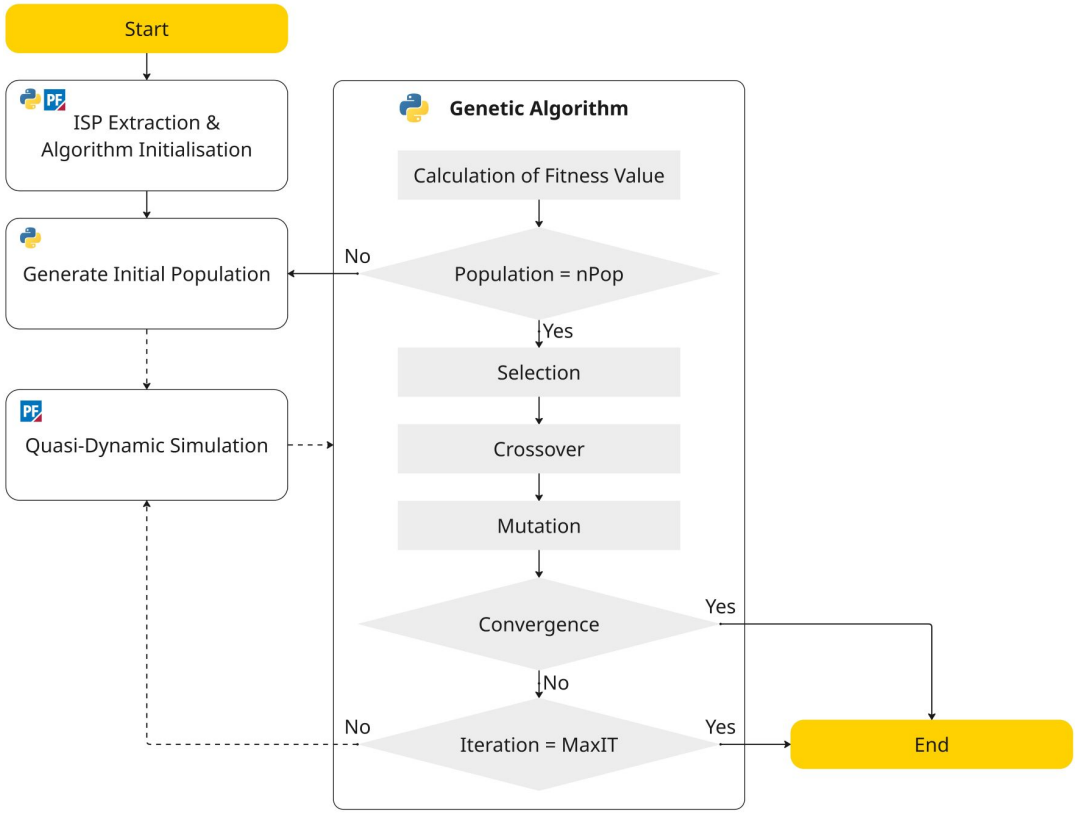

Figure 4.3: Flowchart of the GA-based optimisation process. Python initializes the algorithm and generates an initial population, after which evolutionary operators guide the search towards feasible and near-optimal solutions. Dashed lines indicate data exchange with PowerFactory: Python provides simulation settings and candidate opening sets, while PowerFactory returns QD simulation results. The process terminates upon convergence or reaching the maximum iterations.

4.3. Implementation of the Integrated Simulation and Optimisation Framework

The proposed framework integrates GA-based optimisation with QD simulations in a closed-loop process. The GA generates candidate network configurations, encoded as discrete decision variables representing network openings, leveraging its effectiveness in handling discrete optimisation problems and its adaptability to complex network structures.

Each candidate configuration is evaluated using QD simulations through a multi-objective fitness function that balances network losses, voltage performance, and asset loading, making use of the GA's capability to handle nonlinear and multi-objective optimisation problems.

Through the application of crossover and mutation operators, the GA efficiently explores the solution

space of the case study network. These evolutionary operators also support the scalability of the framework to larger and more topologically complex meshed LV grids.

The framework relies on an integrated MV-LV network model (Section 3.1.5) suitable for QD simulations, requiring:

- Network topology of the supplying MV feeder(s) and the meshed LV grid, except radially configured LV feeders;
- Hourly load and generation profiles of LV connections within the meshed section;
- Aggregated hourly load and generation profiles at distribution transformer level for secondary substations supplying radial LV feeders that are not part of the meshed LV grid but connected to the same MV feeder;
- Asset characteristics of distribution transformers, MV cables, and LV mesh cables.

4.3.1. Overall Workflow

The overall workflow, illustrated in Figure 4.3, combines GA-based optimisation with QD simulations in an iterative process. Starting from an initial population, candidate network configurations are evaluated, and evolutionary operators are applied to progressively improve solution quality.

1. Initialisation
    - The process is initiated by the Python script.
    - All network elements are retrieved from the integrated MV-LV network model.
    - FLs are identified through a pruning procedure, and a set of branches with the lowest currents is determined, the ISP.
    - The algorithm is initialised and an initial population of candidate network configurations, of size *nPop*, is generated with information from the ISP and FLs.
2. QD Simulation
    - The network topology in the model is adapted according to the candidate opening set.
    - Candidate solutions that violate the radial topology constraint are classified as infeasible. These solutions are assigned a penalised fitness value to ensure elimination in subsequent generations.
    - QD simulations are executed for the specified simulation periods.
    - The QD simulation outputs are collected and returned to Python for evaluation.
3. Fitness Evaluation and Evolutionary Operators
    - Fitness Evaluation: The QD simulation results are processed in Python, and the fitness value of each chromosome is computed using the defined fitness function.
    - Sorting: The population is sorted based on fitness (Algorithm 3).
    - Selection: Chromosomes with higher fitness values are selected to serve as parents for the next generation.
    - Crossover: Parent solutions are recombined to generate offspring (Algorithm 4).
    - Mutation: Random perturbations are applied to offspring (Algorithm 5).
4. Algorithm Termination
    - Convergence is assessed based on a predefined number of consecutive iterations (*patience*) with no improvements in fitness.
    - The algorithm also checks whether the maximum number of iterations (*MaxIT*) has been reached.
    - If neither stopping condition is satisfied, the updated population is returned to the QD simulation stage for further evaluation.

- Once *MaxIT* is reached or convergence is achieved, the algorithm terminates and outputs the best solution identified during the optimisation process as its approximation of the global optimum.

The integration of the evolutionary operators within the complete optimisation workflow is formalised in Algorithm 6, which summarises the iterative procedure.

4.3.2. Quasi-Dynamic Simulations

The QD simulations are performed at hourly resolution, matching the level of temporal detail of the load and generation profiles. A full-year simulation requires approximately 3.5–5 minutes per run, excluding data handling and post-processing. Given the large number of candidate solutions evaluated by the GA, incorporating full-year simulations within the optimisation loop would render the method practically unattractive and limit its scalability to larger networks or broader application.

Table 4.2: Total active power demand and PV generation evaluated at the timestamps corresponding to the extreme LV operating conditions (maximum demand, maximum PV in-feed, and minimum demand) in the meshed LV grid from October 2024 to September 2025.

Extreme point	Timestamp	Total Demand	Total Generation
Maximum demand	2025-01-19 16:00	1.1927 MW	0.0 MW
Maximum PV generation	2025-04-29 11:00	0.4764 MW	0.1873 MW
Minimum demand	2025-09-14 03:00	0.3604 MW	0.0 MW

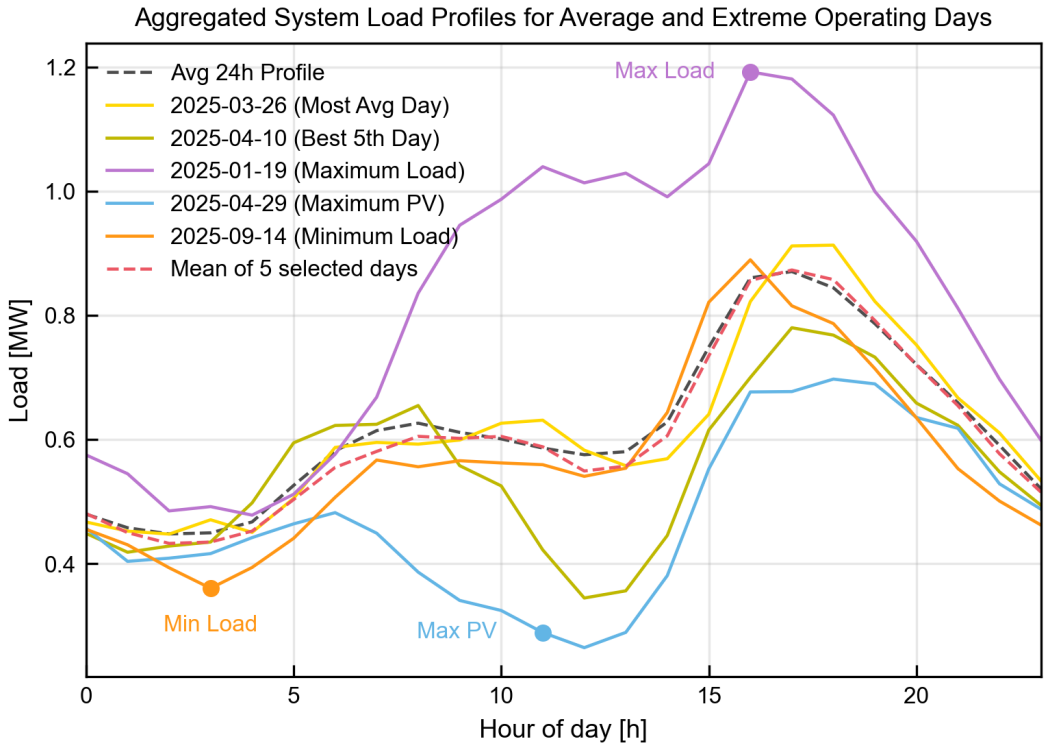

Figure 4.4: Aggregated deterministic LV load profiles of the meshed LV grid for selected representative operating days during the period October 2024 to September 2025, compared with the annual mean 24-hour LV load profile and the mean 24-hour LV load profile of the selected subset.

To reduce the computation time whilst maintaining physical representativeness, each candidate is evaluated using a representative subset of operating days selected to capture average conditions and extremes (Table 4.2). The subset includes:

- maximum demand,

- minimum demand,
- maximum PV generation,
- day with smallest mean squared error (MSE) relative to the annual mean profile,
- a day minimizing the MSE relative to the annual mean profile.

The last day (10 April 2025) of the subset is included to further minimise the MSE between the subset and the annual profile, improving the accuracy of loss estimation. The MSE is defined as

$$\text{MSE}(y, \hat{y}) = \frac{1}{n} \sum_{i=1}^{n} (y_i - \hat{y}_i)^2, \tag{4.9}$$

where y_i denotes the actual value obtained from full-year QD simulations, $\hat{y_i}$ the corresponding value represented by the subset and n the number of data points. The MSE is chosen as a metric because it emphasises larger deviations from the annual mean profile [56].

Using a set of representative days balances computational efficiency and accuracy. Including additional days would reduce the approximation error but increase computation time. The representativeness of the selected subset is illustrated in Figure 4.4 and further analysed in Appendix B.

Genetic Algorithm Configuration

The GA configuration adopted in this study is based on the parameter selection and convergence analysis presented in Appendix D, where population size, crossover and mutation rates, and convergence behaviour were evaluated. This analysis identified a configuration that achieves consistent convergence and solution quality. The resulting parameter values are fixed and applied consistently throughout this work, and are summarised below:

- **Number of Variables** (*nVar*): The number of decision variables corresponds to the number of FLs in the network. Each variable represents the position of an opening in one FL, such that a feasible radial network configuration is obtained.
- **Variable Ranges** (*VarRanges*): Each FL is represented by an ordered list of candidate branch identifiers at which an opening can be placed. The discrete search space is therefore defined by these candidate sets. As the number of candidate branches differs per FL, the decision variables have non-uniform, FL-specific ranges, which are captured in the vector *VarRanges*.
- **Initial Population**: The decision variables derived from the heuristic ISP extraction method are used to generate the initial population. For each individual, these decision variables are first copied, after which 50% of the variables are reassigned within their respective range. This strategy preserves guidance from the ISP while introducing sufficient diversity to support effective exploration of the search space.
- **Population Size** (*nPop*): The population size is fixed at 20 individuals. During the selection phase, only the fittest *nPop* individuals are passed on to the subsequent generation.
- **Crossover Percentage** (*pCrossover*): A crossover percentage of 70% is applied to promote recombination of promision solutions and exploration of diverse network configurations.
- **Mutation Percentage** (*pMutation*): A mutation rate of 30% is used to introduce sufficient random variations into the population and reduce the risk of premature convergence to local optima.
- **Convergence Criterion** (*patience*): An early-stopping criterion based on stagnation is employed to terminate the optimisation when no further improvement is observed. The GA stops when the best fitness value remains unchanged for five consecutive generations, indicating convergence.
- **Maximum Number of Iterations** (*MaxIT*): If the early-stopping criterion is not triggered, the GA terminates upon reaching the predefined maximum number of iterations. A limit of 30 iterations is selected as an effective compromise between computational efficiency and solution quality.

4.4. Simulation Results

This section evaluates the performance of the proposed GA-based optimisation-simulation framework. Sections 4.4.1 and 4.4.2 first analyse the impact of population initialisation and the robustness of the selected GA configuration. Section 4.4.3 then examines the drivers of optimisation performance, followed by Section 4.4.4, which asses the role of stochasticity in the optimisation process. Finally, Sections 4.4.5–4.4.7 evaluate the impact on system performance under present and future conditions.

The GA results are benchmarked against several reference configurations for the case study (Section 3.2.1). The *ISP* represents a heuristic baseline, whereas the *Worst-Case* configuration provides sensitivity bounds. In addition, Gaia's *Fuse-Removal* and *Cable-Cut* strategies are included as representative industry approaches, currently employed within Stedin. The *Gaia Fuse-Removal* approach prioritizes the removal of fuses to create network openings, resorting to cable disconnections only when necessary to avoid violations of operational constraints. Conversely, the *Gaia Cable-Cut* approach constructs radial configurations by directly disconnecting LV mesh cables.

4.4.1. Effect of ISP on Initialisation Strategy

To assess the impact of initialisation, ISP-based initialisation (derived at peak demand) is compared with four alternatives: ISP derived at peak PV, ISP at minimum demand, fully random initialisation, and worst-case initialisation. Worst-case initialisation represents the inverse of the ISP strategy: instead of opening the branch with the lowest current in each FL, the branch with the highest current is selected.

Figure 4.5a shows that worst-case initialisation converges slowest, requiring approximately 20 iterations, while random initialisation converges after about eight iterations. ISP-based initialisation derived at peak demand achieves both faster convergence and lower final fitness values.

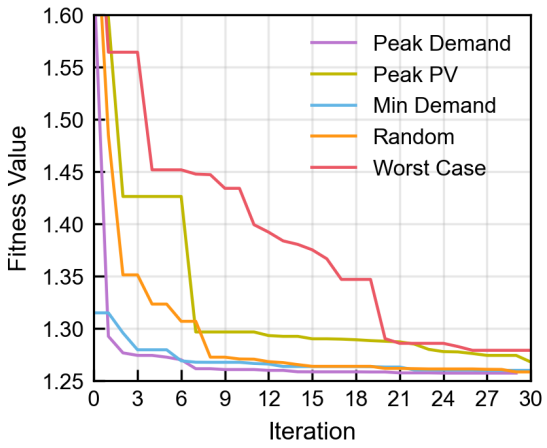

(a) ISP-based initialisation derived at peak demand is compared with ISP derived at peak PV, ISP at minimum demand, fully random initialisation, and worst-case initialisation.

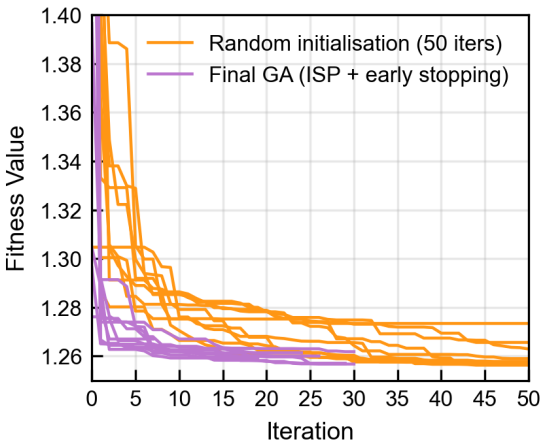

(b) Fitness convergence across 10 runs comparing random initialisation (terminated at 50 iterations) with the final GA configuration using ISP-based initialisation derived at peak demand and early stopping (triggered after 5 consecutive identical fitness values or terminated at a maximum of 30 iterations).

Figure 4.5: Effect of different initialisation strategies on GA convergence behaviour.

4.4.2. Robustness of the GA Optimisation Results

To assess solution consistency, the robustness of the selected GA configuration is evaluated across ten independent optimisation runs in Appendix D.3. The results demonstrate that the GA consistently converges to high-quality solutions across repeated runs, exhibiting stable optimisation behaviour during both the GA iterations and the subsequent full-year validation.

A small deviation is observed between the fitness values computed during optimisation and those obtained from full-year QD simulations. This discrepancy reflects a minor bias introduced by the use of five representative days instead of a full annual evaluation. As demonstrated in Appendix D.4, this bias leads to a slight systematic underestimation of fitness, with an average relative deviation of approxi-

mately 0.53%. This indicates that extreme operating conditions are not fully captured or that average active power losses are slightly underestimated.

The magnitude of this deviation remains limited, while reducing the number of evaluated days from 365 to 5 yields a substantial improvement in computational efficiency. This demonstrates that the adopted approximation achieves an effective balance between accuracy and computational effort.

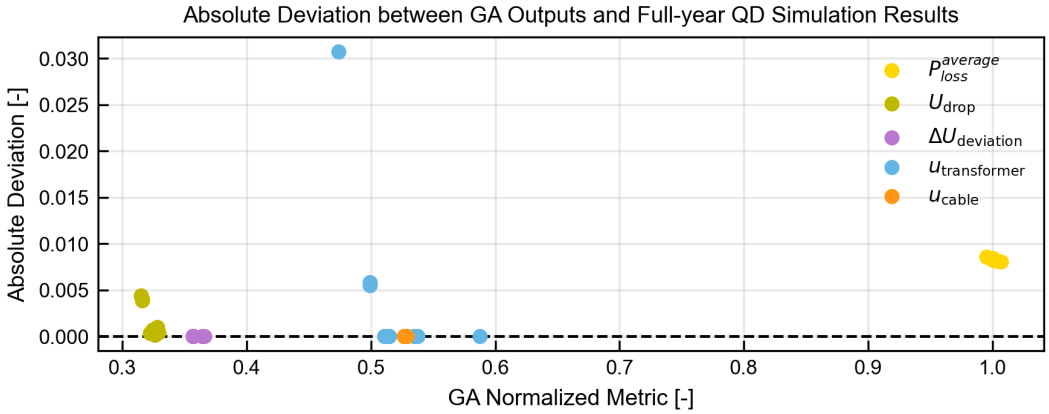

Figure 4.6: Scatter plot of absolute deviations between GA-based evaluations and full-year QD simulation results. Shown are deviations of the normalised performance indicators used in the fitness function (Equation (4.6)), quantifying the bias introduced by the reduced set of representative operating days. A value of zero indicates perfect agreement.

Figure 4.6 shows that the largest discrepancy occurs for transformer loading, with a maximum deviation of approximately 0.03 in its normalised value, corresponding to about 3.6% loading difference. Annual average losses are consistently underestimated by approximately 0.010, while maximum voltage drop and voltage deviation exhibit smaller differences of around 0.005, corresponding to deviations in the order of 0.1–0.01 V.

Given the planning-oriented nature of the optimisation, these deviations remain within acceptable engineering tolerances. Overall, the validation indicates that the GA captures both average and extreme operating conditions with sufficient accuracy, and that the use of representative days provides a reliable and computationally efficient basis for network reconfiguration.

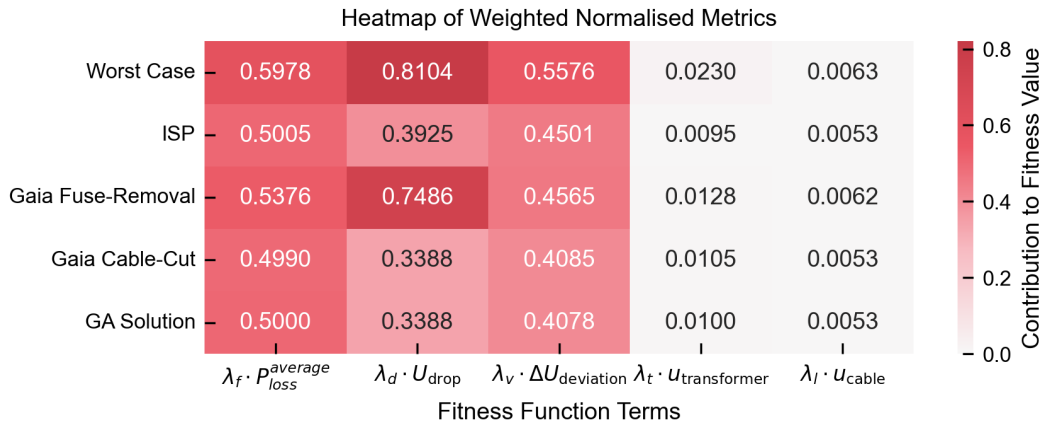

Figure 4.7: Weighted decomposition of the fitness function for a representative GA-optimised configuration compared with the Worst Case, Gaia strategies (fuse-removal and cable-cut), and ISP configurations. The figure illustrates the weighted contributions of the individual normalized performance indicators to the total fitness value, as computed using Equation (4.6).

4.4.3. Drivers of GA Optimisation Performance

Having established the robustness of the GA, this section examines the performance indicators driving the optimisation and the resulting trade-offs. Figure 4.7 presents a weighted decomposition of the fit-

ness function (Equation (4.6)) for a representative GA solution compared with reference configurations.

The GA and Gaia Cable-Cut configurations exhibit comparable performance. While Gaia achieves slightly lower losses, the GA solution compensates through improved voltage profile and reduced transformer loading, indicating a trade-off between objectives. This behaviour reflects the multi-objective nature of the problem. The optimisation yields a set of non-dominated solutions referred to as the Pareto-optimal front, representing trade-offs between loss minimisation, improved voltage profile, and asset utilisation [48]. A solution is considered non-dominated if no other solution performs better in all objectives simultaneously. In mathematical terms, a solution X_1 dominates X_2 if:

$$\forall i \in \{1, 2, \ldots, N_{obj}\}, f_i(X_1) \leq f_i(X_2) \tag{4.10}$$

$$\exists j \in \{1, 2, \ldots, N_{obj}\}, f_i(X_1) < f_i(X_2), \tag{4.11}$$

where N_{obj} denotes the number of objectives [37]. The Pareto front represents the set of solutions offering the most favourable trade-offs between competing objectives. As shown in Figure 4.8, most GA solutions lie on this Pareto front, and no single configuration dominates across all objectives. The figure also highlights the best-compromise solution, defined as the solution with the lowest fitness value. While this solution achieves low losses and voltage deviation, it does not perform best across all objectives.

By combining the objectives into a weighted fitness function, the final solution reflects a prioritisation of the objectives through the selected weights. Consequently, the choice of weights introduces subjectivity into the optimisation outcome. In particular, higher weights assigned to loss and voltage-related terms strongly influence the optimisation outcome.

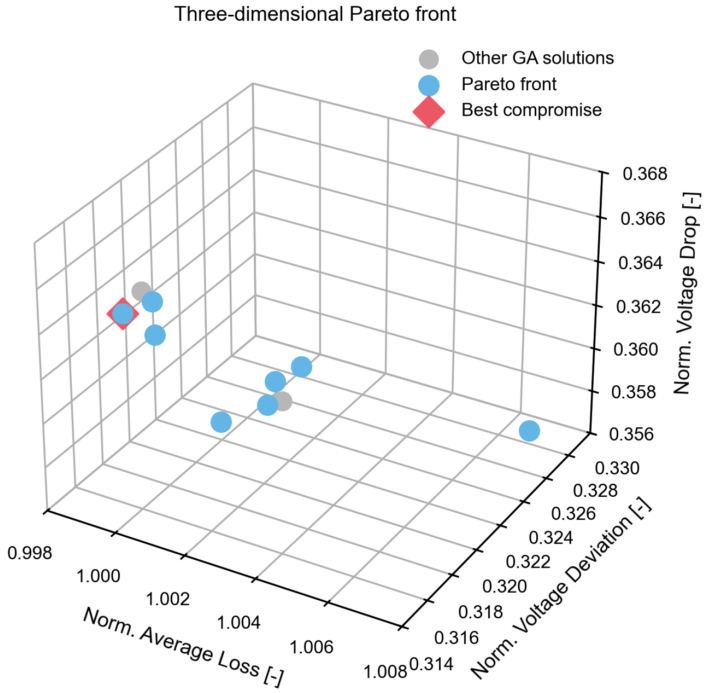

Figure 4.8: Three-dimensional Pareto front plot of normalised active power losses, voltage deviation, and voltage drop for ten independent GA solutions, highlighting Pareto front solutions (blue) and the best-compromise solution (red diamond). The figure shows that eight out of ten GA solutions obtained from independent runs lie on the Pareto front.

To assess consistency among GA solutions, Table 4.3 summarises full-year QD simulation results for ten independent GA-optimised configurations. Here, the annual energy losses are calculated according to Equation (3.2). The limited spread in loss and voltage indicators confirms the robustness of the optimisation to near-optimal solutions. Transformer loading shows greater variability as a result of its lower penalty weight, reflecting its role as a soft constraint.

Table 4.3: Statistical summary of key operating conditions derived from full-year QD simulations for ten independent GA-optimised configurations, parameterised according to Section 4.3.2. Median values represent typical system performance, while minimum and maximum values capture variability across independent optimisation runs.

	Minimum	Median	Maximum
Annual Energy Losses [MWh]	95.59	96.08	96.67
Maximum Voltage Drop [V]	3.32	3.32	3.40
Max Voltage [V]	237.58	237.67	237.79
Min Voltage [V]	229.07	229.52	229.55
Transformer Loading [%]	60.57	61.49	70.50
Cable Loading [%]	52.67	52.68	52.89

Extending the optimisation to 100 iterations yields only marginal improvements, indicating rapid convergence under the current parameter configuration. The best compromise solution shows a slight additional loss reduction (-0.03%) and improved voltage deviation (-0.07 V), at the expense of a small increase in maximum voltage drop (+0.08 V).

As explained in Section 4.1.7, the relative importance of the trade-off between loss, voltage-related and asset loading terms is treated heuristically, based on analysis of the relative contributions and ranges of performance indicators, and refined through iterative tuning. Nevertheless, the selected weighting was found to yield balanced optimisation behaviour for this case study.

In future research, these weights could be derived from more grounded considerations, such as economic cost functions or region-specific operational priorities. Moreover, the presented coefficients are calibrated for a single case study and may require adjustment depending on the characteristics of different grid areas. For example, voltage deviation could be weighted less strongly if post-optimisation control actions, such as tap changer adjustments, are available. Conversely, higher weights on transformer loading may be appropriate in regions where transformers operate close to their technical limits, particularly when designing future-proof grids under increasing loading and DG.

4.4.4. Impact of Stochasticity on GA Convergence

Despite consistent convergence, small variations in final solutions remain. These arise from the stochastic nature of the GA and the presence of multiple Pareto-front solutions as discussed in Section 4.4.3, meaning that the final outcome depends partly on stochastic effects in the algorithm.

Randomness is introduced during both initialisation and application of evolutionary operators.

- Initialisation:
  - The MST extracted using Kruskal's algorithm (Algorithm 1) is mathematically non-unique, but the Python implementation preserves original insertion order for equal weights, thereby ensuring deterministic behavior. The ordering of network elements depends on the model state, making the resulting MST and derived set of excluded branches effectively model-dependent.
  - The ISP extraction evaluates loops sequentially, such that the resulting ISP depends on the order in which the set of branches excluded from the MST are considered. Although non-unique, it remains reproducible for a fixed model.
  - The initial population is generated based on the ISP by randomly reassigning 50% of decision variables within their bounds, introducing controlled stochasticity. Conversely, this randomness is partially mitigated through ISP-based initialisation, which provides structured starting solutions instead of a fully random population.
- Evolutionary operators:
  - Crossover randomly selects parent solutions, while recombination itself is deterministic.
  - Mutation introduces randomness by selecting chromosomes and genes for modification and reassigning decision variables within their allowed ranges.

These stochastic elements influence convergence to different near-optimal solutions within the combinatorial search space. Early stopping (after five consecutive identical fitness values) further limits exploration in later generations, for minor improvements in solution quality.

To assess whether ISP-based initialisation limits solution quality due to reduced randomness and thus search space coverage, it is compared with fully random initialisation. Figure 4.5b demonstrates that ISP-based initialisation leads to faster and more stable convergence. Statistical results further show that the final GA configurations with ISP-based initialisation and early stopping achieve performance comparable to that obtained with random initialisation and a 50-iteration limit, as shown in Tables 4.3 4.4, respectively. This indicates that the improved convergence efficiency does not compromise solution quality, while comparable solutions are obtained in significantly fewer iterations.

Table 4.4: Statistical summary of key operating conditions derived from full-year QD simulations for ten independently GA-optimised configurations using random initialisation and a maximum of 50 iterations. Median values represent typical system performance, while minimum and maximum values capture variability across optimisation runs.

	Minimum	Median	Maximum
Annual Energy Losses [MWh]	95.70	96.06	96.45
Maximum Voltage Deviation [V]	3.32	3.36	3.58
Max Voltage [V]	237.52	237.62	237.81
Min Voltage [V]	229.25	229.52	229.55
Transformer Loading [%]	60.59	63.68	72.37
Cable Loading [%]	52.68	52.80	52.91

To improve search space coverage while retaining high-quality starting solutions, a different initialisation approach could be considered. In [30], [32] a single high-fitness individual is added to an otherwise random population. However, since parent selection is stochastic, such individuals may not always be propagated. This limitation can be mitigated through selection mechanisms that favour fitter individuals, such as rank-based selection [32], increasing their probability of contributing to offspring generation.

4.4.5. System Performance

The practical relevance of the proposed framework is assessed by evaluating system performance over the course of a year, based on a QD simulation covering a full year. Table 4.5 compares annual energy losses and maximum LV voltage drop for the GA-optimised configuration and reference configurations. Relative to the Gaia Fuse-Removal strategy, the GA reduces annual losses by 6.78 MWh (6.6%) and more than halves the maximum voltage drop.

Figure 4.9 shows the LV voltage profile at annual peak demand. The Gaia Fuse-Removal strategy selects opening locations near cable ends, resulting in pronounced voltage gradients. In contrast, both Gaia Cable-Cut and GA configurations place openings closer to the cable center, yielding more balanced voltage profiles and reducing the maximum voltage drop from 7.39 V to 3.32 V. Between the latter two, the GA produces a slightly more balanced voltage profile.

Table 4.5: Results of full-year QD simulations (October 2024–September 2025) for key system performance indicators, comparing reference configurations with the GA-optimised configuration.

Configuration	**Annual Energy Losses [MWh]**	**Maximum Voltage Drop [V]**
ISP	97.11	3.74
Gaia Fuse-Removal	102.82	7.39
Gaia Cable-Cut	95.86	3.32
GA Solution	96.04	3.32

Table 4.6 shows that these improvements extend to voltage and asset loading indicators. Compared to Fuse-Removal, the GA increases minimum voltage and reduces transformer and cable loading, indicating more balanced asset utilisation. Compared to Gaia Cable-Cut, improvements are smaller, including a 5.7% reduction in voltage range and a 2.8% decrease in transformer loading.

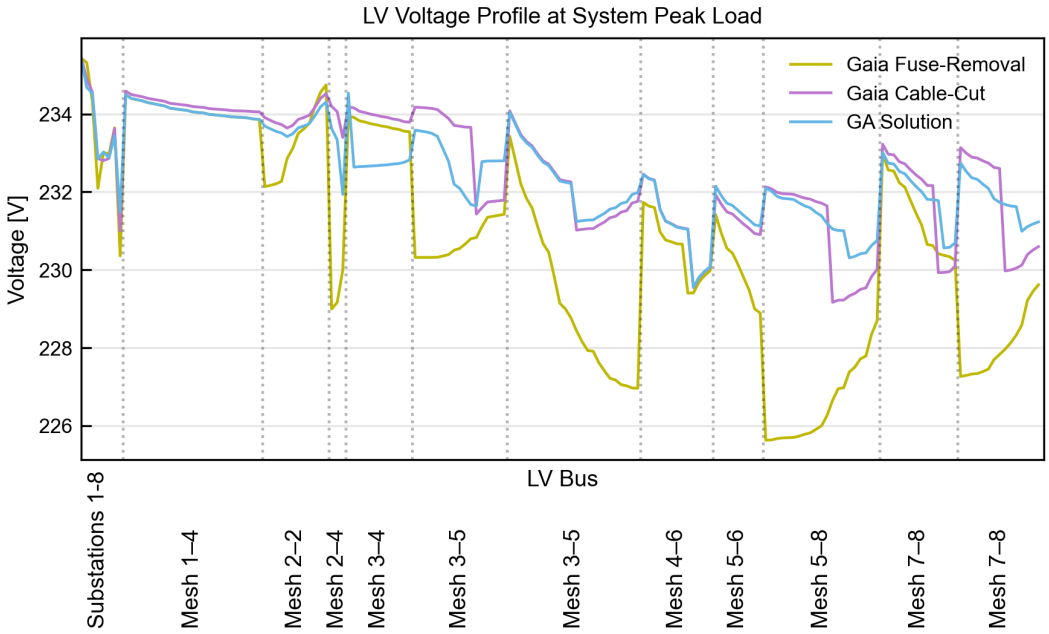

Figure 4.9: LV voltage profile of the Gaia Strategy and the GA-optimised configurations at annual peak demand (19 January 2025, 16:00). Substations 1–8 denote the buses at the secondary sides of the distribution transformers, while the remaining buses are grouped according to their original LV mesh cables (mesh x–x).

Table 4.6: Results of full-year QD simulations (October 2024–September 2025) for voltage and asset loading indicators used as soft constraints in the optimisation, comparing reference configurations with the GA-optimised configuration.

Configuration	Max Voltage [V]	Min Voltage [V]	Transformer Loading [%]	Cable Loading [%]
ISP	238.13	229.08	61.62	52.62
Gaia Fuse-Removal	238.65	225.62	76.73	62.31
Gaia Cable-Cut	237.74	229.16	63.01	52.72
GA Solution	237.64	229.55	61.27	52.68

Figure 4.10 further illustrates these differences. The wide voltage spread observed for Fuse-Removal reflects significant voltage variation, whereas Gaia Cable-Cut and the GA configuration produce distributions centred around nominal values. Differences between latter two are minor, although the GA achieves a slightly narrower distribution.

Comparison with the ISP configuration, shown in Appendix E.2, reveals that the additional improvement achieved by the GA remains limited, confirming the results in Tables 4.5 and 4.6. This indicates that the ISP already provides a near-optimal solution for the studied network. The GA refines this solution by accounting for interactions between multiple loop openings, resulting in modest gains.

From a practical perspective, heuristic approaches such as ISP and Gaia Cable-Cut may be sufficient for this network, given their near-optimal performance and the additional computational effort and modelling requirements associated with the GA. In both cases, appropriately selected opening locations yield results comparable to the GA-optimised solution.

Nevertheless, the contribution of this thesis lies in the structured integration of optimisation and simulations within a closed-loop framework, enabling a systematic and scalable approach to network reconfiguration. This framework translates optimised placement of network openings in reduced energy losses and a more uniform voltage distribution. For the studied network, the benefits of optimisation remain limited, as heuristic methods already achieve near-optimal performance. However, this analysis is based on a single, relatively small case study. For larger or more complex networks, where interactions between mesh openings are stronger, heuristic methods may become less effective, and

the proposed GA-based approach is expected to provide more substantial performance gains.

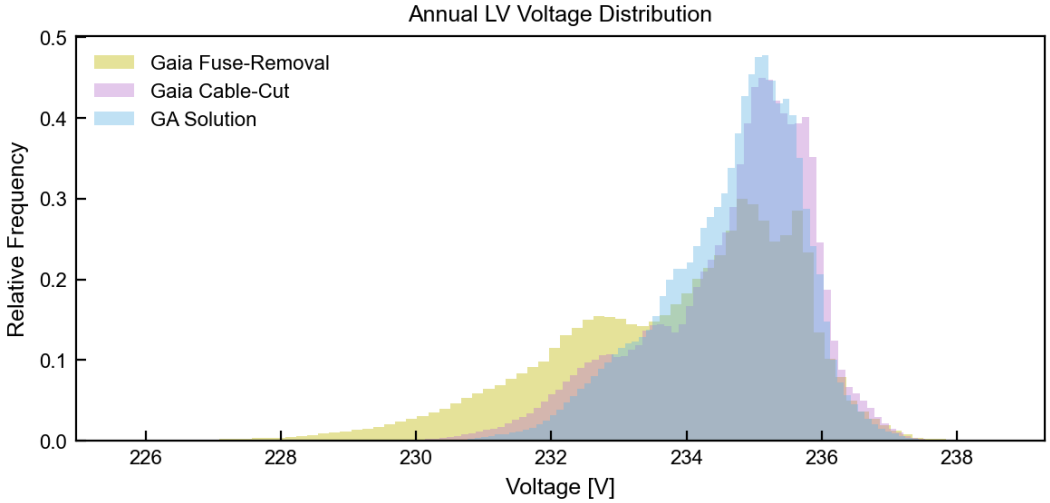

Figure 4.10: Distribution of LV bus voltages over the simulated year for the Gaia Strategy and GA-optimised grid configuration. The histogram represents the relative frequency of voltage values across all LV buses and all simulated time steps.

4.4.6. Cost Implications of Relocating Opening Locations

While the proposed framework identifies electrically feasible opening locations, practical implementation also requires consideration of physical feasibility. In some cases, implementing the optimal solution may be undesirable (e.g., cutting a cable near a transformer) or infeasible. Engineers may therefore choose alternative measures, such as fuse removal or relocating the opening to a nearby accessible location.

Such deviations introduce cost–performance trade-offs. As opening locations are shifted from their optimal positions, network performance deteriorates. To illustrate the lower bound of performance, an extreme scenario is constructed using a worst-case strategy, defined as the inverse of the ISP approach, where in each loop the branch with the highest current magnitude is opened.

Under this configuration, annual energy losses increase to 113.70 MWh and the maximum LV voltage drop rises to 7.91 V. This corresponds to an increase of approximately 10% in losses relative to the Gaia Fuse-Removal strategy, accompanied by a significant deterioration in voltage quality. In addition, the voltage range widens substantially, and severe asset overloading occurs, including distribution transformer loading up to 137.91% and cable loading of 63.11%.

These results demonstrate that the Gaia Fuse-Removal strategy does not represent a worst-case scenario and that poorly chosen opening locations can lead to inferior performance. Consequently, practical implementation requires careful balancing of feasibility constraints against increases in losses, voltage profiles, and asset loading.

From a planning perspective, this highlights the importance of evaluating alternative de-meshing strategies, such as fuse removal versus cable disconnection, within a broader cost–performance framework. This enables informed decision-making that considers not only electrical optimality, but also feasibility, safety, and long-term operational costs.

4.4.7. Future Proof Network Reconfiguration Under High Demand

While the preceding analysis demonstrates the effectiveness of the GA-based reconfiguration under current conditions, it is essential to assess its robustness under future operating scenarios. Increasing demand and DG are expected to significantly alter network loading and voltage profiles.

The supplying substation currently operates at a peak demand of 24 MVA with 5 MVA of installed PV capacity. By 2050, these values are projected to increase to 52 MVA and 37 MVA, respectively. This scenario is approximated by scaling all loads by 217%, representing electrification-driven demand

growth, while keeping PV capacity constant. Uniform PV scaling is not considered, as future expansion is expected to occur through additional installations rather than proportional growth of existing units.

Table 4.7: Results of full-year QD simulations (October 2024–September 2025) under an increased loading scenario, where demand is scaled to 217%, for key system performance indicators. The results compare reference configurations with the GA-optimised configuration. Values exceeding operational limits are shown in italics.

Configuration	Annual Energy Losses [MWh]	Maximum Voltage Drop [V]
ISP	276.55	8.44
Gaia Fuse-Removal	305.35	*16.81*
Gaia Cable-Cut	270.37	7.48
GA Solution	271.94	7.48

As in the present-day scenario, Table 4.7 compares the performance of the different configurations. However, under increased loading, the differences between strategies become more pronounced. The Gaia Fuse-Removal configuration exhibits severe voltage violations, with a maximum drop of 16.81 V, whereas both Gaia Cable-Cut and the GA remain within acceptable limits. Compared to Fuse-Removal, these approaches reduce losses by approximately 11% and significantly improve voltage performance.

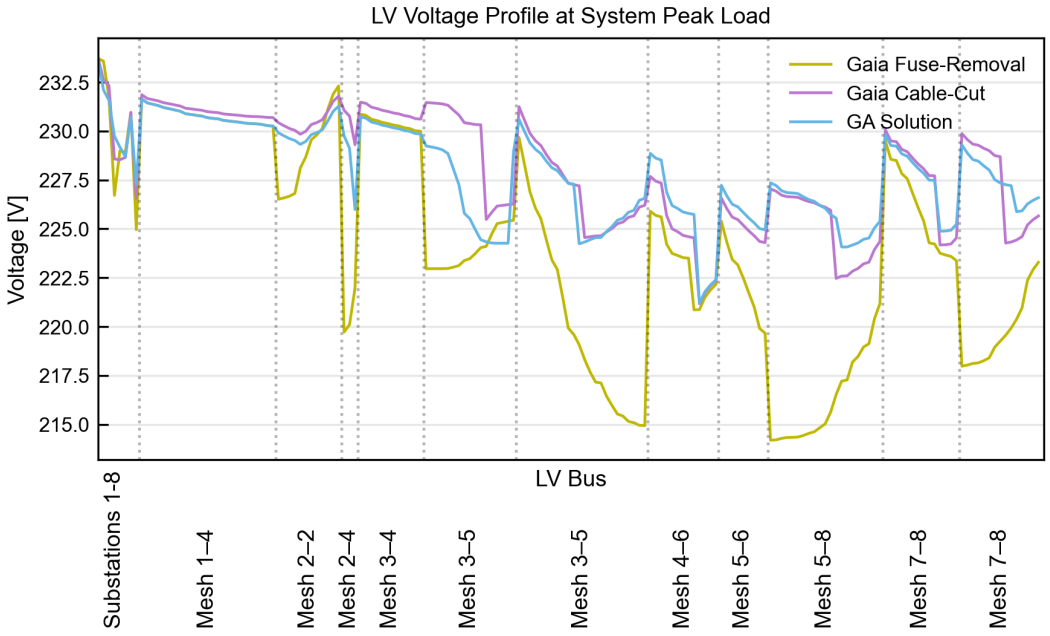

Figure 4.11: LV voltage profile of the Gaia Strategy and the GA-optimised configurations under future demand scenario at annual peak demand (19 January 2025, 16:00). Substations 1–8 denote the buses at the secondary sides of the distribution transformers, while the remaining buses are grouped according to their original LV mesh cables (mesh x–x).

Table 4.8: Results of full-year QD simulations (October 2024–September 2025) under an increased loading scenario, where demand is scaled to 217%, for voltage and asset loading indicators used as soft constraints in the optimisation. The results compare reference configurations with the GA-optimised configuration. Values exceeding operational limits are shown in italics.

Configuration	Max Voltage [V]	Min Voltage [V]	Transformer Loading [%]	Cable Loading [%]
ISP	237.49	220.09	*136.32*	*104.23*
Gaia Fuse-Removal	237.63	214.19	*171.32*	*140.89*
Gaia Cable-Cut	237.21	221.16	*139.68*	96.60
GA Solution	237.34	221.20	*134.12*	96.05

Figures 4.11 and 4.12 show that, compared to the present-day scenario, voltage variation increases significantly under higher loading. This effect is most pronounced for the Fuse-Removal strategy, which produces steep voltage gradients due to suboptimal opening locations. In contrast, the GA and Gaia Cable-Cut configurations maintain more balanced profiles and voltage distributions centred around nominal values, with only minor differences, the GA achieving a slightly more uniform distribution.

The corresponding voltage extremes and asset loading indicators in Table 4.8 confirm these trends. The Gaia Fuse-Removal configuration leads to severe violations, including substantial asset overloading. In contrast, the GA significantly mitigates these issues by keeping cable loading below 100% and reducing transformer overload compared to heuristic approaches.

Overall, the results demonstrate that GA-based reconfiguration remains effective under substantial demand growth. It produces more balanced network configurations with improved voltage profiles and reduced asset overloading, supporting its application as a planning-oriented reconfiguration tool. The impact of extreme PV growth, not considered here, may further increase the importance of such optimisation-based approaches.

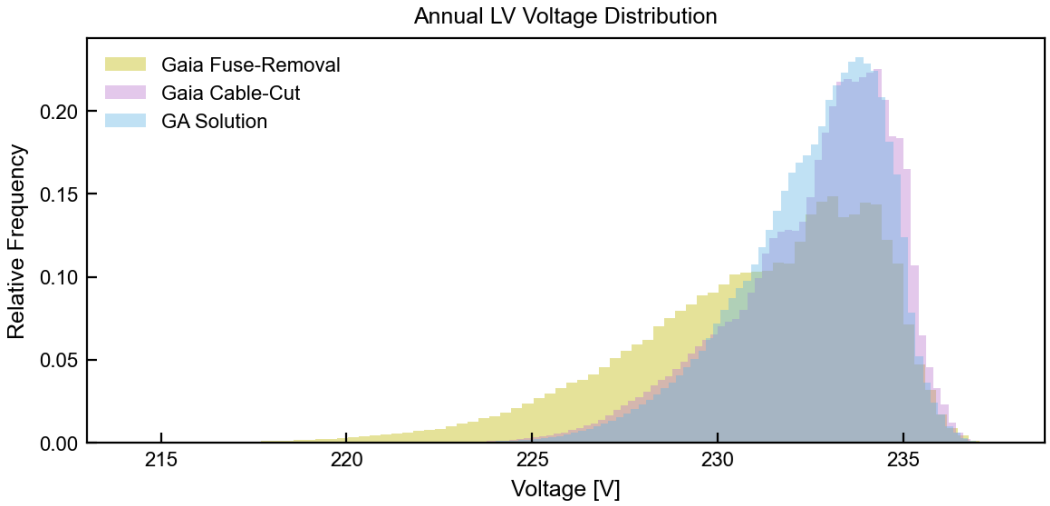

Figure 4.12: Distribution of LV bus voltages under future demand scenario over the simulated year for the Gaia Strategy and GA-optimised grid configuration. The histogram represents the relative frequency of voltage values across all LV buses and all simulated time steps.

5

Conclusion and Recommendation

This thesis presents an integrated simulation and optimisation framework for the automatic determination of network openings in meshed LV grids. The proposed framework combines a GA-based optimisation approach in Python with QD simulations in PowerFactory in a closed-loop process, enabling efficient exploration of the highly combinatorial solution space and identification of technically feasible radial grid configurations.

A central component of this framework is the integrated MV-LV network model, which facilitates direct access to grid elements, manipulation of network topology and evaluation of reconfiguration strategies. This model forms the foundation for automated analysis and optimisation of LV grid de-meshing.

Overall, the framework offers a systematic, scalable, and practically applicable solution for LV grid reconfiguration. It supports grid design in the context of increasing electrification and the growing integration of distributed generation, thereby contributing to the development of reliable and future-proof distribution systems.

The following sections present the main findings of this thesis, discuss the limitations of the proposed approach, and provide recommendations for future work.

5.1. Research Questions

1. How can meshed LV grids be modelled by leveraging Stedin's existing distribution network modelling tools?

This thesis demonstrates that meshed LV grids can be effectively modelled by integrating LV grid representations into MV models to form a combined MV–LV network model. The developed model captures key electrical interactions, including circulating currents and load sharing between distribution transformers, without introducing excessive model complexity through aggregation of non-critical LV components.

Validation shows that the model reproduces characteristic meshed LV grid power flow behaviour not present in current MV representations, such as the influence of path diversity and the emergence of circulating currents driven by small voltage differences. As a result, the model provides a sufficiently accurate representation for analysing power flows, voltage behaviour, and asset loading in meshed LV grids.

Although based on a single case study and limited by simplifications such as a fixed MV voltage reference and the omission of phase asymmetry, the model is well suited for planning-level analyses. In addition, integration with the PowerFactory Python API enables its seamless integration into an automated optimisation frameworks.

2. What impact do circulating currents have on cable and distribution transformer power losses in meshed LV grids?

Circulating currents, induced by small voltage differences between interconnected distribution transformers, can significantly increase LV cable losses. In the model, these voltage differences are represented through tap-setting variations, reflecting practical deviations from misaligned tap positions.

Results from the case study indicate that a single-step deviation from the nominal tap setting at one distribution transformer leads to a strong increase in circulating currents, reflected in a disproportionate rise in reactive power exchange relative to active power at the MV feeder infeed. Consequently, annual LV cable losses increase substantially, by 68.8–140.6%, whereas the impact on MV cable and distribution transformer losses remains limited to only a few percent.

Moreover, active power losses in both LV cables and distribution transformers follow a U-shaped relationship, where both positive and negative deviations from the nominal tap setting result in higher losses. Although the relative increase in losses is smaller for distribution transformers, their absolute increase can still be significant.

These findings highlight that circulating currents are a structurally significant phenomenon in meshed LV grids. Coordinated tap-setting strategies are therefore essential to limit unnecessary losses and avoid inefficient use of network capacity.

3. Which constraints must be considered when selecting feasible locations for network openings in meshed LV grids?

Reconfiguration of meshed LV grids into a radial topology must satisfy both structural and operational constraints. Structurally, the resulting network must be radial and free of isolated buses, which can be verified through the incidence matrix. Operationally, power flow feasibility must be guaranteed across all considered operating conditions.

In addition, practical implementation requires compliance with DSO-specific design criteria. In this thesis, four key criteria were prioritised: absolute voltage limits, and allowable voltage variation, transformer loading, cable loading. These are explicitly incorporated, while additional criteria related to protection, safety, and short-circuit performance should be evaluated as post-optimisation feasbility checks.

4. How can these constraints be integrated into an automated and systematic approach for identifying feasible network opening locations?

The identified constraints are incorporated into a GA-based optimisation framework through a multi-objective fitness function. Operational limits are included as weighted and normalised penalty terms, allowing candidate configurations to be evaluated based on power losses, absolute voltage limits, and allowable voltage variation, and asset loading

Feasibility is enforced through a combination of simulation and constraint handling: configurations violating radiality are explicitly penalised, while power flow feasibility is ensured through successful execution of QD simulations. This approach enables automated identification of technically feasible and near-optimal network opening locations in line with operational requirements.

All these answers contribute to addressing the main research question outlined at the introduction of this thesis:

> *How can an automated distribution network reconfiguration method be developed to identify feasible opening locations in existing meshed LV grids that minimise power losses and improve system reliability?*

This thesis proposes an integrated modelling and optimisation framework for automatic determination of network openings in meshed LV grids. The underlying optimisation problem exhibits rapidly increasing combinatorial complexity due to the number of fundamental loops and potential opening positions along each LV mesh cable. For the studied 11-loop network, the de-meshing problem exhibits a combinatorial search space exceeding $1.3 * 10^{13}$ possible configurations, making manual or exhaustive evaluation computationally infeasible. To address this, the framework combines GA-based optimisation with QD simulations in a closed-loop process, enabling automated evaluation of candidate configurations.

The results show that the method consistently identifies technically feasible configurations that balance power loss minimisation, voltage profile improvement, and asset utilisation. Validation confirms robust convergence, with only minor approximation error (0.53%) introduced by the use of representative operating days. Optimisation performance is primarily driven by trade-offs between loss minimisation and voltage profile improvement, while loading constraints act mainly as feasibility criteria.

Application to a single realistic case study demonstrates that the framework achieves a 6.6% reduction in annual losses and substantial improvements in voltage profiles compared to a fuse-removal based approach in Gaia, while maintaining compliance with operational constraints. Compared to Gaia's cable-disconnection approach, the proposed method delivers comparable performance.

Further analysis shows that the heuristic ISP strategy, that is used for GA initialisation, alone provides a strong, low-complexity baseline for for the case study network, achieving near-optimal performance in the studied case. The GA offers additional value by globally coordinating opening locations across interacting meshes, consistently yielding small incremental improvements.

Scenario analysis further shows that optimisation-based configurations remain more robust under increased loading, whereas heuristic approaches may lead to larger constraint violations. This highlights the growing importance of systematic optimisation under future-loading conditions.

The primary contribution of this thesis is the integration of simulation and optimisation into a unified, automated framework for network reconfiguration. While benefits are limited for the studied network, it demonstrates a promising and scalable approach for larger and more complex meshed LV grids, where heuristics fail to capture global interactions. By enabling effective de-meshing, the framework enhances grid reliability through reduced short-circuit levels, simplified protection, and compliance with operational constraints, providing a systematic method to support efficient and future-proof LV grid operation.

5.2. Future Research

Several opportunities remain for further research to enhance the effectiveness, robustness, and practical applicability of the proposed method. The following directions are recommended for future work:

- **Application to additional case studies**
  The proposed GA-based optimisation approach was configured and validated using a single case study network. Applying it to a broader set of LV grids would enable a systematic assessment of its robustness, scalability and general applicability. In particular, larger and more complex systems may reveal performance trends not evident in the 11-loop case, and help determine whether the method consistently outperforms heuristic approaches in globally coordinating network opening decisions across interacting network sections.

  Similarly, Section 4.4.5 shows that the ISP heuristic provides a strong, computationally efficient baseline, yielding a near-optimal solutions for the studied network. Future work should therefore assess its robustness and performance in larger and more complex grids with stronger interactions.

- **Exploration of alternative multi-objective optimization formulations**
  While the GA-based optimisation approach provides robust near-optimal solutions, Section 4.1.7 shows that repeated runs may converge to different configurations reflecting trade-offs between competing objectives. These trade-offs are currently governed by heuristic weight selection, and refined through iterative tuning. Future work could derive weights from more grounded considerations, such as economic cost functions or region-specific priorities. Additionally, alternative formulations, such as fuzzy membership approaches, could be explored to minimise bias and enable balanced multi-objective evaluation [16].

- **Incorporation of additional operational design constraints**
  The current optimisation framework includes a subset of Stedin's design criteria. Extending the formulation to incorporate additional constraints, such as protection coordination, safety requirements (e.g., protection against electric shock), and maximum circuit impedance, would improve alignment with practical design standards.

- **Extension to economic and environmental evaluation**
  This study focuses on technical performance indicators. Future work should extend the analysis to include economic and environmental aspects, such as cost–benefit comparisons of different de-meshing strategies (e.g., fuse removal versus physical cable removal) and associated environmental impacts.

- **Exploration of alternative initialisation strategies and evolutionary operators**
  Section 4.4.4 states that search space coverage may be improved by adopting alternative initialisation strategies, such as attaching a high-fitness individual to an otherwise random population [30], [32]. As stochastic parent selection may limit propagation of the high-fitness individual, this can be mitigated using mechanisms such as rank-based selection [32]. Further improvements in GA efficiency and convergence could be achieved by refining evolutionary operators, including alternative recombination strategies and mutation techniques [48].

- **Assessment under extreme PV growth scenarios**
  The impact of extreme PV penetration was not explicitly considered in the future operating scenarios analysed in Section 4.4.7. High levels of distributed generation may significantly affect optimal network configurations due to reverse power flows and voltage rise. Incorporating such scenarios could provide deeper insight into the robustness of current and proposed de-meshing strategies.

- **Explore the potential of parallel computing**
  The execution time is constraint by the iterative evaluation of candidate configurations for the set of representative operating days. Evaluating candidate configurations in parallel using multiple DIgSILENT PowerFactory licenses can significantly reduce execution time and enhance practical application across large-scale and large numbers of LV grids.

5.3. Recommendations

Based on the findings of this research, the following practical recommendations are proposed for Stedin and other distribution system operators:

- **Use DA3 measurement data to support LV grid model validation and de-meshing prioritisation**
  Although DA3 measurement units are in 2026 sparsely deployed, their feeder-level voltage and current measurements provide valuable information on actual loading patterns. Comparing measured data with simulation results can help identify unexpectedly highly loaded LV mesh cables, indicating circulating currents and supporting prioritisation of LV grids for de-meshing.
- **Systematically align transformer types and tap settings in meshed LV grids**
  Section 3.2.6 demonstrated that misalignment of transformer types and tap settings results in voltage differences between interconnected secondary substations, driving circulating currents and increasing active power losses. Systematic alignment of transformer parameters can reduce unnecessary losses and avoid inefficient use of network capacity, particularly prior to de-meshing.

  The analysis was limited to a LV grid fed by a single MV-feeder. In practice, meshed LV grids may be supplied by multiple MV feeders, introducing additional voltage magnitude and phase-angle differences at the primary side of distribution transformers. Investigating such configurations would provide further insight into the combined impact of misalignment in tap settings and MV-level asymmetries on circulating currents and associated losses.
- **Develop standardised data and topology representations**
  Manually building an integrated MV-LV network model is labour-intensive and highlights the lack of a unified data structure and topology representation across tools. Standardised data and topology descriptions should enable the evaluation of the network from HV/MV down to LV levels within a single modelling environment. This would eliminate the need for intermediate conversion steps, improve scalability and support the application of optimisation-based de-meshing methods in large and complex networks. It would also enable other research and grid design that requires an integrated view of the power system.

  As an intermediate step, this limitation can be mitigated by developing transformation tools to convert existing LV grid models in Gaia into PowerFactory. This would enable the integration of MV and LV representations in the near future and enhance applicability to large-scale meshed LV grids.
- **Include future load and generation scenarios in de-meshing analyses**
  Long-term demand growth and increasing PV penetration may significantly alter network stress patterns, and careful reconfiguration is required to prevent severe violations of voltage and asset loading constraints, as shown in Section 4.4.7. Incorporating predictions of future demand and generation ensures that de-meshing decisions remain robust under evolving grid conditions, rather than being optimised solely for current operation.
- **Balance optimisation outcomes with engineering judgement**
  Exact implementation of optimised opening locations may be infeasible or impractical (e.g., near transformers). Alternatives such as fuse removal or relocation may be preferred. However, uninformed adjustments can result in solutions that underperform heuristics, as discussed in Section 4.4.6. Decisions should therefore balance feasibility and cost against impacts on network losses, voltage profile, and asset loading.

References

[1] Ministery of Economic affairs, *Klimaatakkoord*, 2019.

[2] Autoriteit Consument en Markt, *Ontwerp codebesluit codewijziging veiligheid bestaande laagspanningsnetten*, May 2022. [Online]. Available: www.acm.nl.

[3] Autoriteit Consument en Markt, *Netcode elektriciteit*. [Online]. Available: https://wetten.overheid.nl/BWBR0037940/2025-10-01.

[4] Stedin, *Investeringsplan 2024-2026*, 2024.

[5] E. Coster, *Motivatiedocument ontmazen ls-netten*, 2017.

[6] G. Celli, F. Pilo, G. Pisano, V. Allegranza, R. Cicoria, and A. Iaria, "Meshed vs. radial mv distribution network in presence of large amount of dg," in *IEEE PES Power Systems Conference and Exposition*, vol. 2, 2004, pp. 709–714. DOI: 10.1109/PSCE.2004.1397664.

[7] B. Ruben, D. Strickland, M. Aten, and R. Ferris, "Meshing radial networks at 11kv," in *2011 2nd IEEE PES International Conference and Exhibition on Innovative Smart Grid Technologies*, 2011, pp. 1–8. DOI: 10.1109/ISGTEurope.2011.6162691.

[8] M. Davoudi, V. Cecchi, and J. R. Aguero, "Investigating the ability of meshed distribution systems to increase penetration levels of distributed generation," in *IEEE SOUTHEASTCON 2014*, Institute of Electrical and Electronics Engineers Inc., Nov. 2014, ISBN: 9781479965854. DOI: 10.1109/SECON.2014.6950661.

[9] M. Kerzel, J. Garzon-Real, M. Zdrallek, D. Wolter, and C. Schacherer, "Optimal switch configuration algorithm for dynamically meshed power distribution grids," *SEST 2020 - 3rd International Conference on Smart Energy Systems and Technologies*, Sep. 2020. DOI: 10.1109/SEST48500.2020.9203089.

[10] B. Zhao, Y. Yang, and X. Li, "Current decomposition in loop distribution network," in *2023 26th International Conference on Electrical Machines and Systems, ICEMS 2023*, Institute of Electrical and Electronics Engineers Inc., 2023, pp. 3733–3738, ISBN: 9798350317589. DOI: 10.1109/ICEMS59686.2023.10344554.

[11] Z. Zhang *et al.*, "Research on optimal power flow control of closed-loop distribution network with superconducting cable," in *2020 Asia Energy and Electrical Engineering Symposium (AEEES)*, 2020, pp. 555–559, ISBN: 9781728167824.

[12] Phase to Phase, *Gaia lv network design*.

[13] H. Lotfi, M. E. Hajiabadi, and H. Parsadust, "Power distribution network reconfiguration techniques: A thorough review," in *Sustainability*. Multidisciplinary Digital Publishing Institute (MDPI), Nov. 2024, vol. 16. DOI: 10.3390/su162310307.

[14] P. Schavemaker and L. van der Sluis, *Electrical Power System Essentials*, 2nd ed. Wiley & Sons Ltd, 2017.

[15] Phase to Phase, *Netten voor distributie van elektriciteit*. Phase to Phase, 2021, vol. 4, ISBN: 9789081798310.

[16] M. R. Maghami, E. Yaghoubi, M. Mohamed, E. Yaghoubi, M. Z. Jahromi, and T. K. Fei, "Multi-objective optimization of unbalanced power distribution systems: A comprehensive approach to address uncertainties and enhance performance," *Energy Conversion and Management: X*, vol. 27, Jul. 2025, ISSN: 25901745. DOI: 10.1016/j.ecmx.2025.101087.

[17] K. Ma, L. Fang, and W. Kong, "Review of distribution network phase unbalance: Scale, causes, consequences, solutions, and future research directions," *CSEE Journal of Power and Energy Systems*, vol. 6, pp. 479–488, 3 Sep. 2020, ISSN: 20960042. DOI: 10.17775/CSEEJPES.2019.03280.

[18] Phase to Phase, *Stochastische load flow in gaia met het gaussian-mixture belastingmodel*, Dec. 2022.

[19] M. Loos, S. Werben, and J. Maun, “Circulating currents in closed loop structure, a new problematic in distribution networks,” *2012 IEEE Power and Energy Society General Meeting*, pp. 1–7, 2012. DOI: 10.1109/PESGM.2012.6344889.

[20] D. Shirmoharmnadi, H. Member, and S. Member, “A compensatioon-based power flow method for weakly meshed distribution and transmission networks,” *IEEE Transactions on Power Systems*, vol. 3, pp. 753–762, 2 1988.

[21] D. K. Patel, S. Mansani, and A. K. Goswami, “Fast flexible direct power flow for unbalanced and balanced distribution systems,” *International Transactions on Electrical Energy Systems*, vol. 2022, 2022, ISSN: 20507038. DOI: 10.1155/2022/2857358.

[22] W. Peng, L. Sha, K. Zheng, S. Dong, X. Zhang, and J. Tian, “An online loop closing current calculation method for complex distribution networks considering source and load uncertainties,” *IET Generation, Transmission and Distribution*, vol. 19, 1 Jan. 2025, ISSN: 17518695. DOI: 10.1049/gtd2.13359.

[23] K. Zhang, Y. Feng, Y. Yu, and Q. Guo, “Study of calculation schemes of currents induced by closing-loop operations in medium-voltage distribution grids,” in *2019 IEEE Sustainable Power and Energy Conference (iSPEC)*, 2019, pp. 2488–2493, ISBN: 9781728149301. DOI: 10.1109/iSPEC48194.2019.8974973.

[24] F.-D. Hou, B. Que, L. Chen, W.-Y. Zhen, and J.-Q. Fu, “A simultaneous closed loop current calculation method for multiple distribution lines,” in *2nd Annual International Conference on Energy, Environmental & Sustainable Ecosystem Development (EESED 2016)*, vol. 115, Jan. 2017. DOI: 10.2991/eesed-16.2017.7.

[25] H. Wang, X. Yu, Z. Zhang, and Y. Yao, “Calculation, measurement and engineering application of loop closing current in power grid,” in *5th IEEE Conference on Energy Internet and Energy System Integration: Energy Internet for Carbon Neutrality, EI2 2021*, 2021, pp. 2237–2241, ISBN: 9781665434256. DOI: 10.1109/EI252483.2021.9713007.

[26] Z. Qiu, L. Wu, T. Zeng, W. Yuan, X. Zhang, and T. Cheng, “An efficient sparse matrix technique for closed loop current analysis in distribution network,” in *2022 5th International Conference on Renewable Energy and Power Engineering, REPE 2022*, Institute of Electrical and Electronics Engineers Inc., 2022, pp. 222–227, ISBN: 9781665482066. DOI: 10.1109/REPE55559.2022.9948978.

[27] E. Coster, *Ontwerp ontmazen laagspanningsnetten*, 2022.

[28] E. Coster, *Ontwerp laagspanningsnetten*, 2020.

[29] L. I. Silva, E. A. Belati, C. Gerez, and I. C. S. Junior, “Reduced search space combined with particle swarm optimization for distribution system reconfiguration,” *Electrical Engineering*, vol. 103, pp. 1127–1139, 2 Apr. 2021, ISSN: 14320487. DOI: 10.1007/s00202-020-01150-z.

[30] A. Swarnkar, N. Gupta, and K. R. Niazi, “Adapted ant colony optimization for efficient reconfiguration of balanced and unbalanced distribution systems for loss minimization,” *Swarm and Evolutionary Computation*, vol. 1, pp. 129–137, 3 Sep. 2011, ISSN: 22106502. DOI: 10.1016/j.swevo.2011.05.004.

[31] C. Gerez, L. I. Silva, E. A. Belati, A. J. S. Filho, and E. C. Costa, “Distribution network reconfiguration using selective firefly algorithm and a load flow analysis criterion for reducing the search space,” *IEEE Access*, vol. 7, pp. 67 874–67 888, 2019, ISSN: 21693536. DOI: 10.1109/ACCESS.2019.2918480.

[32] “Optimal network reconfiguration to reduce power loss using an initial searching point for continuous genetic algorithm,” *Complexity*, vol. 2020, 2020, ISSN: 10990526. DOI: 10.1155/2020/2420171.

[33] R. Asiamah, Y. Zhou, and A. S. Zamzam, “Machine learning-assisted distribution system network reconfiguration problem,” in *2025 IEEE PES Grid Edge Technologies Conference and Exposition, Grid Edge 2025*, 2025, ISBN: 9798350352528. DOI: 10.1109/GridEdge61154.2025.10887483.

[34] S. E. Hoseini, M. Simab, and B. Bahmani-Firouzi, “Ai-based multi-objective distribution network reconfiguration considering optimal allocation of distributed energy storages and renewable resources,” *International Journal of Smart Electrical Engineering*, vol. 14, 2 2025, ISSN: 2345-6221.

[35] M. R. Islam, H. Lu, J. Hossain, and L. Li, “Multiobjective optimization technique for mitigating unbalance and improving voltage considering higher penetration of electric vehicles and distributed generation,” *IEEE Systems Journal*, vol. 14, pp. 3676–3686, 3 Sep. 2020, ISSN: 19379234. DOI: 10.1109/JSYST.2020.2967752.

[36] D. L. Duan, X. D. Ling, X. Y. Wu, and B. Zhong, “Reconfiguration of distribution network for loss reduction and reliability improvement based on an enhanced genetic algorithm,” *Electrical Power and Energy Systems*, vol. 64, pp. 88–95, 2015, ISSN: 01420615. DOI: 10.1016/j.ijepes.2014.07.036.

[37] H. Lotfi, “Multi-objective network reconfiguration and allocation of capacitor units in radial distribution system using an enhanced artificial bee colony optimization,” *Electric Power Components and Systems*, vol. 49, pp. 1130–1142, 13-14 2021, ISSN: 15325016. DOI: 10.1080/15325008.2022.2049661.

[38] H. Lotfi, A. Azizivahed, A. A. Shojaei, S. Seyedi, and M. F. B. Othman, “Multi-objective distribution feeder reconfiguration along with optimal sizing of capacitors and distributed generators regarding network voltage security,” *Electric Power Components and Systems*, vol. 49, pp. 652–668, 6-7 2021, ISSN: 15325016. DOI: 10.1080/15325008.2021.2011486.

[39] A. Kashtanov, E. Glende, and M. Wolter, “Application of graph theory as a tool for reconfiguration of the distribution network,” in *IEEE PES Innovative Smart Grid Technologies Conference Europe*, vol. 2022-October, 2022, pp. 1–5, ISBN: 9781665480321. DOI: 10.1109/ISGT-Europe54678.2022.9960395.

[40] S. Zhou, Z. Xue, L. Ai, Y. Hu, and A. Cao, “Distribution network fault location method based on graph theory and deep learning under charging load access,” in *2021 IEEE 5th Conference on Energy Internet and Energy System Integration: Energy Internet for Carbon Neutrality (EI2)*, 2021, pp. 1237–1241, ISBN: 9781665434256. DOI: 10.1109/EI252483.2021.9713574.

[41] M. Khoshbaten and P. Poursoltani, “An innovative and robust algorithm for the self-healing of radial distribution networks based on graph theory concept: A case study,” in *2024 28th International Electrical Power Distribution Conference, EPDC 2024*, Apr. 2024, pp. 1–6, ISBN: 9798350385502. DOI: 10.1109/EPDC62178.2024.10571718.

[42] E. F. Yetkin, O. Ceylan, I. Pisica, and A. Ozdemir, “A topology detector based power flow approach for radial and weakly meshed distribution networks,” in *2024 International Conference on Smart Energy Systems and Technologies: Driving the Advances for Future Electrification, SEST 2024 - Proceedings*, 2024, pp. 1–6, ISBN: 9798350386493. DOI: 10.1109/SEST61601.2024.10694284.

[43] Energie Data Services Nederland, *Energiedata voor marktpartijen*. [Online]. Available: https://www.edsn.nl/marktpartijen/.

[44] J.-M. Daignan, *Smart meters in london*, 2022. [Online]. Available: https://www.kaggle.com/datasets/jeanmidev/smart-meters-in-london/data.

[45] Liander, *Open data*. [Online]. Available: https://www.liander.nl/over-ons/open-data#verbruiksdata-slimme-meter.

[46] Phase to Phase, *Pyptp 0.0.32*. [Online]. Available: https://pypi.org/project/pyptp/.

[47] Y. Xiang, P. Salemink, B. Stoeller, N. Bharambe, and W. van Westering, “Power grid model: A high-performance distribution grid calculation library,” *27th International Conference on Electricity Distribution (CIRED 2023)*, vol. 2023, pp. 1089–1093, Jun. 2023. DOI: 10.1049/icp.2023.0633.

[48] S. Mirjalili, “Genetic algorithm,” in *Evolutionary Algorithms and Neural Networks: Theory and Applications*. Springer, 2019, vol. 780, pp. 43–53, ISBN: 978-3-319-93025-1. DOI: https://doi.org/10.1007/978-3-319-93025-1.

[49] A. M. Eldurssi and R. M. O’Connell, “A fast nondominated sorting guided genetic algorithm for multi-objective power distribution system reconfiguration problem,” *IEEE Transactions on Power Systems*, vol. 30, pp. 593–601, 2 Mar. 2015, ISSN: 08858950. DOI: 10.1109/TPWRS.2014.2332953.

[50] D. Jakus, R. Čađenović, J. Vasilj, and P. Sarajčev, "Optimal reconfiguration of distribution networks using hybrid heuristic-genetic algorithm," *Energies*, vol. 13, Mar. 2020, ISSN: 19961073. DOI: 10.3390/en13071544.

[51] A. Mittal, *Kruskal's algorithm*, 2025. [Online]. Available: https://aaryanmittal.medium.com/prims-db212ef73007 (visited on 03/16/2026).

[52] E. Dolatdar, S. Soleymani, and B. Mozafari, "A new distribution network reconfiguration approach using a tree model," *World Academy of Science, Engineering and Technology*, vol. 58, Oct. 2009.

[53] T. T. Nguyen, A. V. Truong, and T. A. Phung, "A novel method based on adaptive cuckoo search for optimal network reconfiguration and distributed generation allocation in distribution network," *International Journal of Electrical Power and Energy Systems*, vol. 78, pp. 801–815, Jun. 2016, ISSN: 01420615. DOI: 10.1016/j.ijepes.2015.12.030.

[54] N. Gupta, A. Swarnkar, K. R. Niazi, and R. C. Bansal, "Multi-objective reconfiguration of distribution systems using adaptive genetic algorithm in fuzzy framework," *IET Generation, Transmission and Distribution*, vol. 4, pp. 1288–1298, 12 Dec. 2010, ISSN: 17518687. DOI: 10.1049/iet-gtd.2010.0056.

[55] C. Zevenbergen, *Development of a universal adaptive voltage control policy for power distribution networks*, Nov. 2024.

[56] R. Hirekerur, *A comprehensive guide to loss functions*, Jun. 2020. [Online]. Available: https://medium.com/analytics-vidhya/a-comprehensive-guide-to-loss-functions-part-1-regression-ff8b847675d6.

A

DIgSILENT PowerFactory MV-LV Grid Model

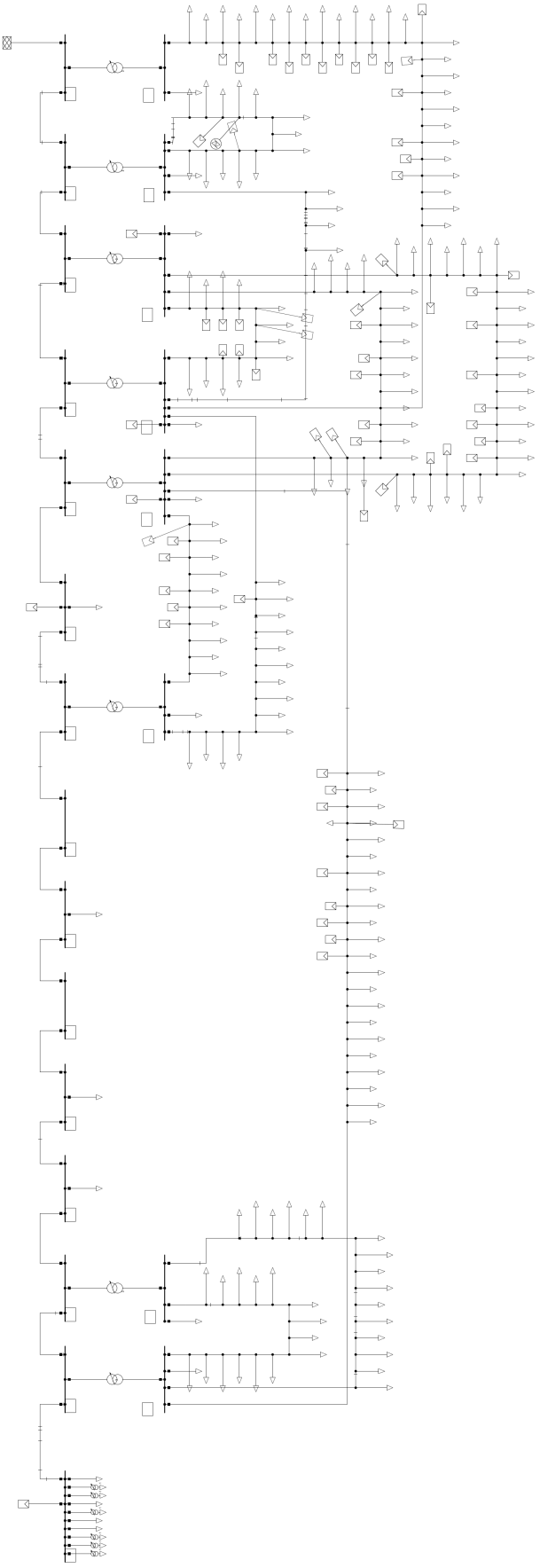

Figure A.1: MV–LV grid network used for the case study, implemented in DIgSILENT PowerFactory.

B

Representative Operating Days

A trade-off must be made between the accuracy of the representative operating-day set and the computational effort required for the QD simulations. As a starting point, four operationally important days were selected: the days with maximum and minimum consumption, the day with maximum PV generation, and the *most average* day, defined as the day with the lowest MSE relative to the annual mean profile. These days ensure that the full range of relevant operating conditions is included.

Additional days are then added heuristically by iteratively selecting the day that minimises the MSE between the subset's mean 24-hour profile and the annual mean day, according to Equation B.1. Here, y_i denotes the actual value obtained from full-year QD simulations, $\hat{y}_i$ the corresponding value represented by the subset and n the number of data points. MSE is chosen because its quadratic nature penalises larger deviations more strongly, making it well suited for identifying representative operating patterns [56].

$$\text{MSE}(y, \hat{y}) = \frac{1}{n} \sum_{i=1}^{n} (y_i - \hat{y}_i)^2 \tag{B.1}$$

Due to simulation time constraints, a subset size of five days was initially selected. Figure B.1 shows that adding the fifth day significantly improves the match between the subset mean profile and the annual mean day. Adding a sixth day results in further improvement, but also increases computational time. To assess the effect of expanding the subset, Table B.1 summarises the performance metrics for subset sizes $k = 4$ to $k = 10$.

Figure B.2 demonstrates that the MSE decreases substantially up to $k = 8$, after which additional days yield negligible improvement. The other performance metrics (MAE, RMSE, MAPE) exhibit a similar stabilisation at $k = 8$. Therefore, a subset size of eight days would provide the most representative set if computational efficiency were not a constraint.

Table B.1: Performance metrics of representative-day subsets of size $k = 4$ to $k = 10$.

Subset Size	Day Added	MSE [MW^2]	MAE [MW]	RMSE [MW]	MAPE [%]
4	None	0.000687	0.021928	0.026203	3.567615
5	2025-04-10	0.000251	0.012867	0.015851	2.218990
6	2024-10-18	0.000087	0.007432	0.009348	1.310489
7	2025-03-14	0.000055	0.005813	0.007402	0.920266
8	2025-07-13	0.000021	0.003737	0.004598	0.654402
9	2024-10-11	0.000026	0.003835	0.005126	0.650985
10	2025-03-08	0.000023	0.003971	0.004820	0.647877

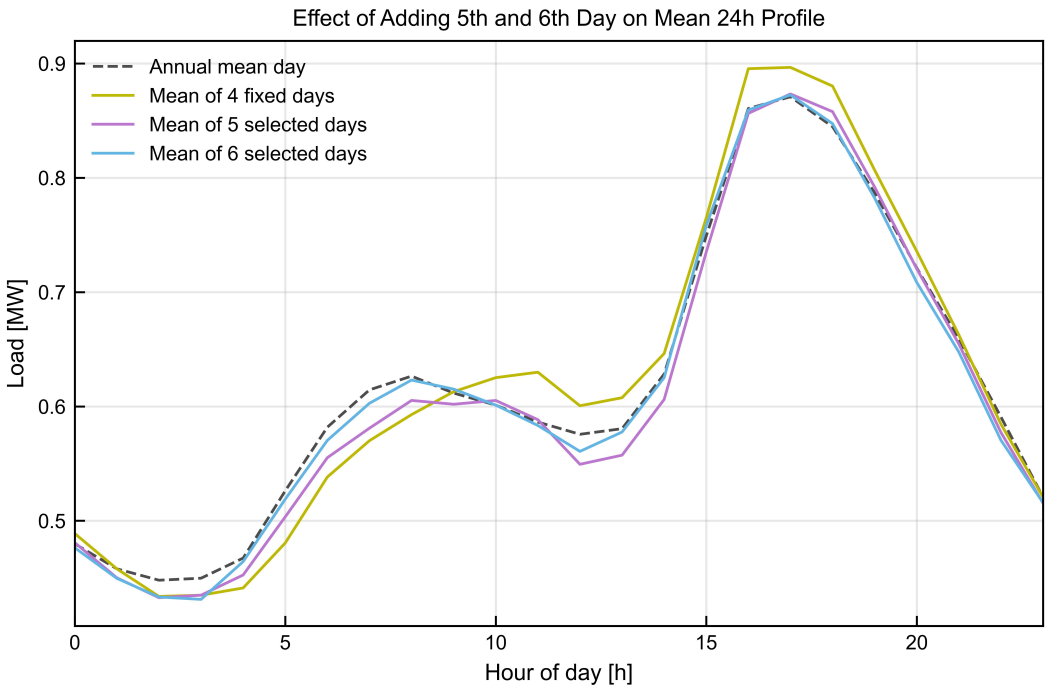

Figure B.1: Effect of adding a 5th and 6th day on the mean 24 hour profile of the subset of representative operating days.

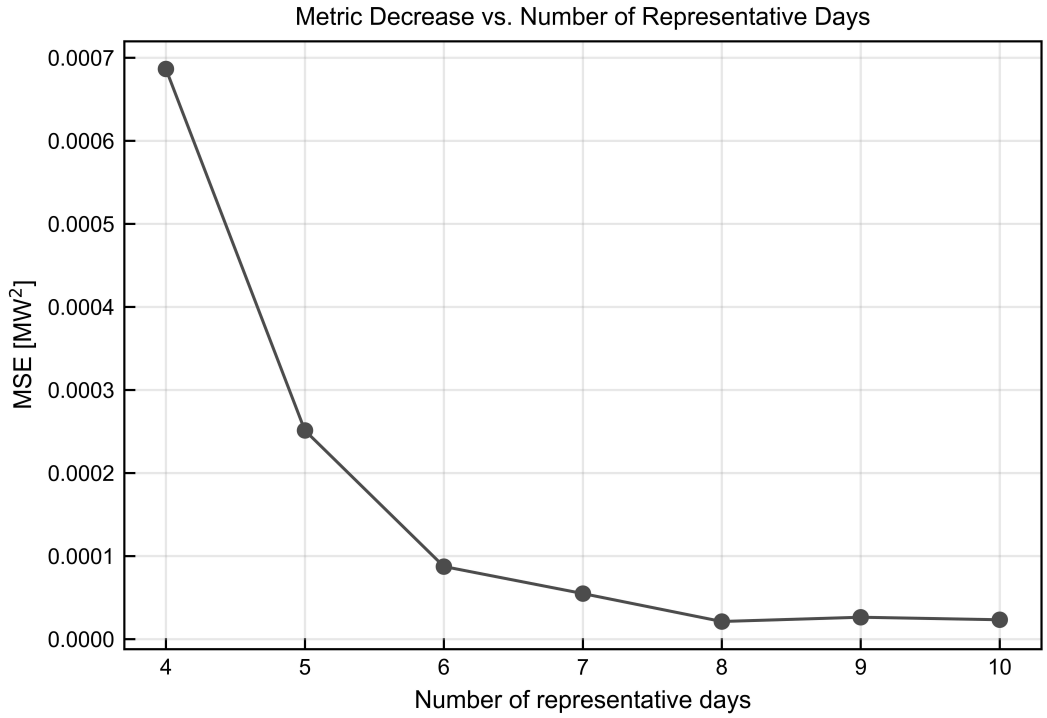

Figure B.2: Reduction in MSE as more representative days are added to the subset.

C

Algorithms

Algorithm 1 Kruskal's Algorithm for Minimum Spanning Tree

Require: List of weighted branches $(a, b, \text{branch\_idx}, w)$, number of buses N_b
Ensure: List of MST branch indices and names

```
parent[i] ← i   ∀i                                   ▷ Initialize disjoint sets
branches_sorted ← sort(branches by w)                ▷ Branches sorted by ascending weight
mst_branches ← [ ]
for all (a, b, branch_idx, w) in branches_sorted do
    r_a ← a                                          ▷ Trace parent pointers of a up to root
    while parent[r_a] ≠ r_a do
        r_a ← parent[r_a]
    end while
    r_b ← b                                          ▷ Trace parent pointers of b up to root
    while parent[r_b] ≠ r_b do
        r_b ← parent[r_b]
    end while
    if r_a ≠ r_b then                                ▷ If roots are different, a and b are in different sets
        Append e_idx to mst_branches
        parent[r_a] ← r_b                            ▷ Merge the two sets (Union)
    end if
    if |mst_branches| = N_b − 1 then
        break
    end if
end for
return mst_branches
```

Algorithm 2 Extract Fundamental Loop

Require: Incidence data structure containing A, bus_order, branch_order
Ensure: List of branch names forming the fundamental loop

```
A ← incidence_data["A"]
bus_order ← incidence_data["bus_order"]
branch_order ← incidence_data["branch_order"]
(N_b, N_e) ← shape(A)
remaining ← 1_{N_e}                          ▷ Boolean mask of remaining branches
changed ← True
while changed do
    changed ← False
    degree_bus ← Σ |A[:, remaining]|          ▷ Bus degrees
    leaf_buses ← {b | degree_bus[b] = 1}
    if |leaf_buses| = 0 then
        break                                 ▷ Only the loop remains
    end if
    for all b ∈ leaf_buses do
        branch_idx ← {e | A[b, e] ≠ 0}
        for all e ∈ branch_idx do
            if remaining[e] then
                remaining[e] ← False          ▷ Remove leaf branch
                changed ← True
            end if
        end for
    end for
end while
loop_idx ← {i | remaining[i] = True}
loop_names ← [branch_order[i] | i ∈ loop_idx]
return loop_names
```

Algorithm 3 Sort Population Algorithm

Require: population pop
Ensure: sorted population a^{sorted}, cost vector C

```
le ← length(pop)                              ▷ population size
C ← []                                        ▷ initialize empty cost array
for i = 0 to le − 1 do                        ▷ iterate over individuals in population
    append pop[i].Cost to C                   ▷ extract and store cost for each individual
end for
sorted_index ← argsort(C)                     ▷ get indices that sort costs
pop^sorted ← []                               ▷ initialize empty sorted array
for all i ∈ sorted_index do                   ▷ iterate over sorted indices
    append pop[i] to pop^sorted               ▷ build sorted population
end for
return pop^sorted, C
```

Algorithm 4 Crossover Operator

Require: parent solutions p_1 and p_2
Ensure: recombined chromosomes c_1 and c_2

```
n ← length(p_1)                                   ▷ number of genes
Initialize c_1[1..n], c_2[1..n]                   ▷ initialize empty arrays for offspring chromosomes
toggle ← 0
for i = 1 to n do                                 ▷ iterate over all genes
    idx_1 ← p_1[i]
    idx_2 ← p_2[i]
    if idx_1 = idx_2 then                         ▷ copy identical genes
        c_1[i] ← idx_1                            ▷ copy the gene
        c_2[i] ← idx_1
    else
        if toggle = 0 then                        ▷ used to alternate between both parents
            c_1[i] ← idx_1                        ▷ replace the gene
            c_2[i] ← idx_2
        else
            c_1[i] ← idx_2
            c_2[i] ← idx_1
        end if
        toggle ← 1 − toggle                       ▷ flip binary
    end if
end for
return c_1, c_2
```

Algorithm 5 Mutation Operator

Require: chromosome c, mutation probability p, VarRanges
Ensure: mutated chromosome c'

```
c' ← copy of c                                    ▷ copy chromosome
n ← length(c')                                    ▷ number of genes
m ← max(1, ⌊n · p⌋)                               ▷ number of genes to mutate
Select m distinct positions at random from {1, ..., n}
for all selected positions i do                   ▷ iterate over selected genes
    L ← VarRanges[i]                              ▷ valid range length for gene i
    c'[i] ← random integer in [0, L − 1]          ▷ replace the gene
end for
return c'
```

Algorithm 6 Genetic Algorithm

Require: Cost function $f(\cdot)$, $nVar$, $VarRanges$, $ISPPosition$, $nPop$, $MaxIT$,$nCrossover$, $nMutation$, mutation probability p, initialization mutation probability p_{init}
Ensure: Best solution $BestSol$

▷ initial population
$pop \leftarrow [\,]$ ▷ initialize empty population array
for $i = 1$ to $nPop$ **do** ▷ iterate over individuals in population
$pop[i] \leftarrow [\,]$ ▷ initialize empty array for each individual
$pop[i].Position \leftarrow$ Mutate$(ISPPosition, p_{init}, VarRanges)$ ▷ initial individual solution
$pop[i].Cost \leftarrow f(pop[i].Position)$ ▷ evaluate and store cost of individual
end for
▷ sort population
$(pop, C) \leftarrow$ SortPopulation(pop) ▷ sort population based on cost
$BestSol \leftarrow pop[1]$ ▷ store best solution
for $it = 1$ to $MaxIT$ **do**
▷ crossover
$pop_c[k] \leftarrow [\,]$ ▷ initialize empty array for crossover population
for $k = 1$ to $nCrossover/2$ **do** ▷ create crossover population of size $nCrossover$
Randomly select parents p_1, p_2 from pop ▷ randomly select two parents for crossover
$(c_1.Position, c_2.Position) \leftarrow$ Crossover$(p_1.Position, p_2.Position)$ ▷ offspring solutions
$c_1[i].Cost \leftarrow f(c_1.Position)$ ▷ evaluate and store cost of offspring solution
$c_2[i].Cost \leftarrow f(c_2.Position)$ ▷ evaluate and store cost of offspring solution
Add c_1, c_2 to pop_c ▷ store offspring solutions
end for
▷ mutation
$pop_m[k] \leftarrow [\,]$ ▷ initialize empty array for mutation population
for $k = 1$ to $nMutation$ **do** ▷ create mutation population of size $nMutation$
Randomly select chromosome c from pop ▷ randomly select chromosome for mutation
$c'.Position \leftarrow$ Mutate$(c.Position, p, VarRanges)$ ▷ mutated chromosome solution
$c'.Cost \leftarrow f(c'.Position)$ ▷ evaluate and store cost of mutated chromosome
Add c' to $pop_{c'}$ ▷ store mutated chromosome solution
end for
▷ sort population
$pop \leftarrow pop \cup pop_c \cup pop_m$ ▷ merge population
$(pop, C) \leftarrow$ SortPopulation(pop) ▷ sort population based on cost
$pop \leftarrow pop[1 : nPop]$ ▷ truncate population
$BestSol \leftarrow pop[1]$ ▷ store best solution
end for
return $BestSol$

D

GA Parameter Selection and Model Configuration

This appendix justifies the GA configuration adopted in this thesis by evaluating the influence of key parameters on convergence behaviour, solution quality, and computational effort. Section D.1 investigates the impact of different population sizes and crossover and mutation settings, and motivates the final crossover and mutation rate selection. Section D.2 then analyses and defines an early stopping criterion of five consecutive identical fitness values, to reduce computational effort while maintaining optimisation performance. Finally, Section D.3 compares the convergence behaviour and solution quality of the two best-performing parameter configurations under both GA optimisation and full-year validation.

D.1. Genetic Algorithm Parameter Selection

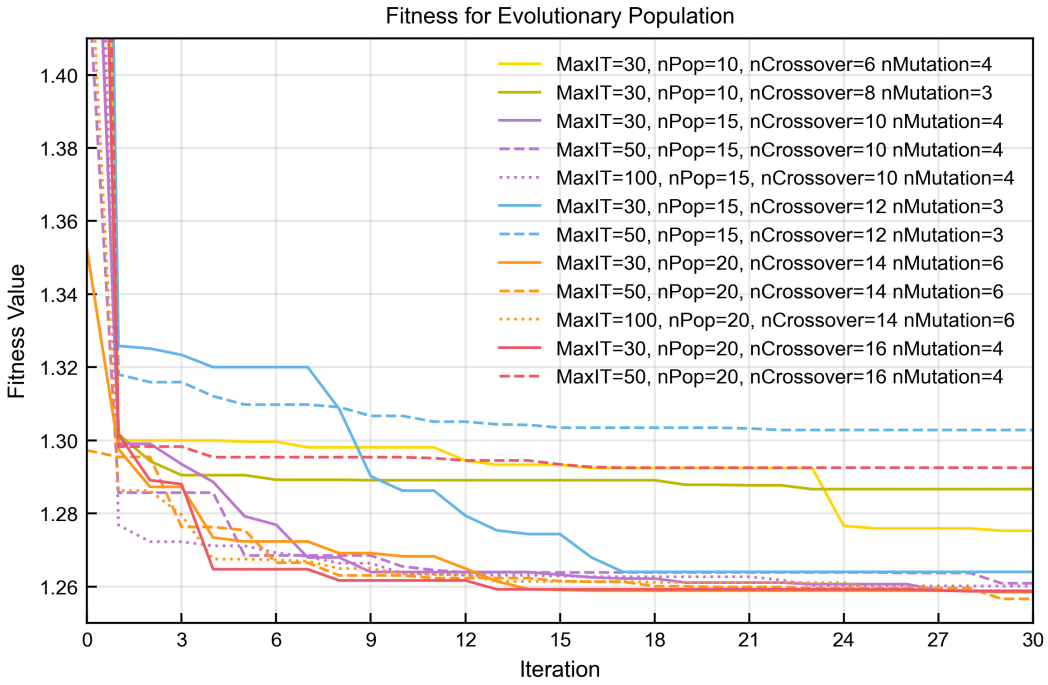

Figure D.1: Evolution of fitness across generations for different GA paramater configurations.

Figure D.1 summarises the convergence behaviour of all evaluated GA parameter configurations. Con-

figurations with a population size of $n_{\text{Pop}} = 10$ consistently fail to reach the fitness levels obtained with larger populations, indicating insufficient exploration of the solution space. The following configurations show the fastest and most consistent convergence:

1. $n_{\text{Pop}} = 15$, $n_{\text{Crossover}} = 10$, $n_{\text{Mutation}} = 4$,
2. $n_{\text{Pop}} = 20$, $n_{\text{Crossover}} = 14$, $n_{\text{Mutation}} = 6$

Both configurations correspond to a crossover rate of 70% and a mutation rate of 30%, and consistently reach fitness values close to 1.262 within the first 8–10 iterations.

By contrast, configurations employing a crossover rate of 80% and a mutation rate of 20% exhibit more variability between runs, indicating insufficient exploration of the solution space. Although the configuration with $n_{\text{Pop}} = 20$, $n_{\text{Crossover}} = 16$, and $n_{\text{Mutation}} = 4$ achieves the best observed fitness value (1.2589) within 30 iterations, this performance is not reproducible in the corresponding 50□iteration run. In comparison, configurations (1) and (2) reach similar fitness levels by iteration 10 and continue to improve, surpassing this value at iterations 40 and 28, respectively, indicating robust convergence.

The crossover and mutation rates are therefore fixed at 70% and 30%. With respect to population size, a trade-off exists between execution time and solution quality. A population of 15 is preferred when computational efficiency is critical, as it achieves consistent convergence in about the same number of iterations with fewer fitness evaluations (due to the smaller population size). For robustness analysis, however, both configurations should be evaluated over a larger number of runs.

D.2. Early Stopping Criterion

To reduce computation time while preserving solution quality, an early stopping criterion based on consecutive identical fitness values is evaluated. Figure D.2 illustrates, for the different GA parameter configurations shown in Figure D.1, the iteration at which each run would terminate under various stopping thresholds.

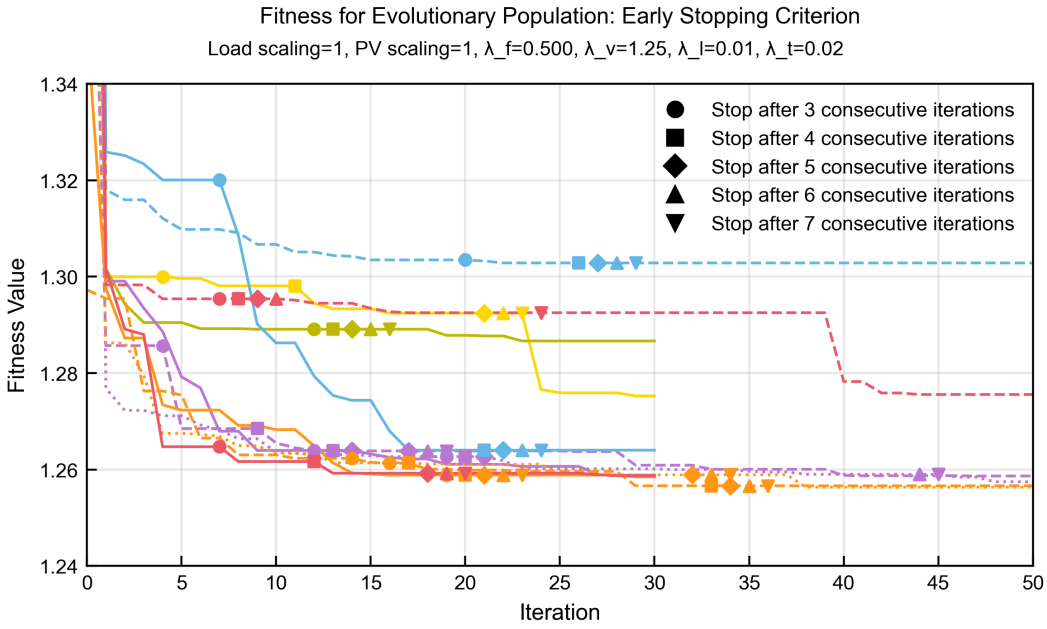

Figure D.2: Iteration at which runs would terminate under different early stopping thresholds

A threshold of three consecutive identical fitness values is found to be overly restrictive, causing all runs to terminate prematurely before meaningful optimisation takes place. Thresholds between five and seven align well with the natural convergence behaviour, as for most configurations they correspond to the point beyond which no further improvements occur.

For the best-performing configurations, no significant improvement is observed after seven identical

fitness values, and most runs reach this point well before 30 iterations. Since thresholds of five and six are typically followed shortly by seven identical iterations, a threshold of five yields identical final solutions with additional computational savings. Therefore, five consecutive identical fitness values is selected as the stopping criterion.

D.3. Comparative Convergence Analysis of Best-Performing Parameter Configurations

To compare the two best-performing configurations, results from ten independent runs are analysed (Figure D.3). Runs terminate either via early stopping or at 30 iterations. A sample size of ten was chosen as a feasible compromise, given the computational effort required per run.

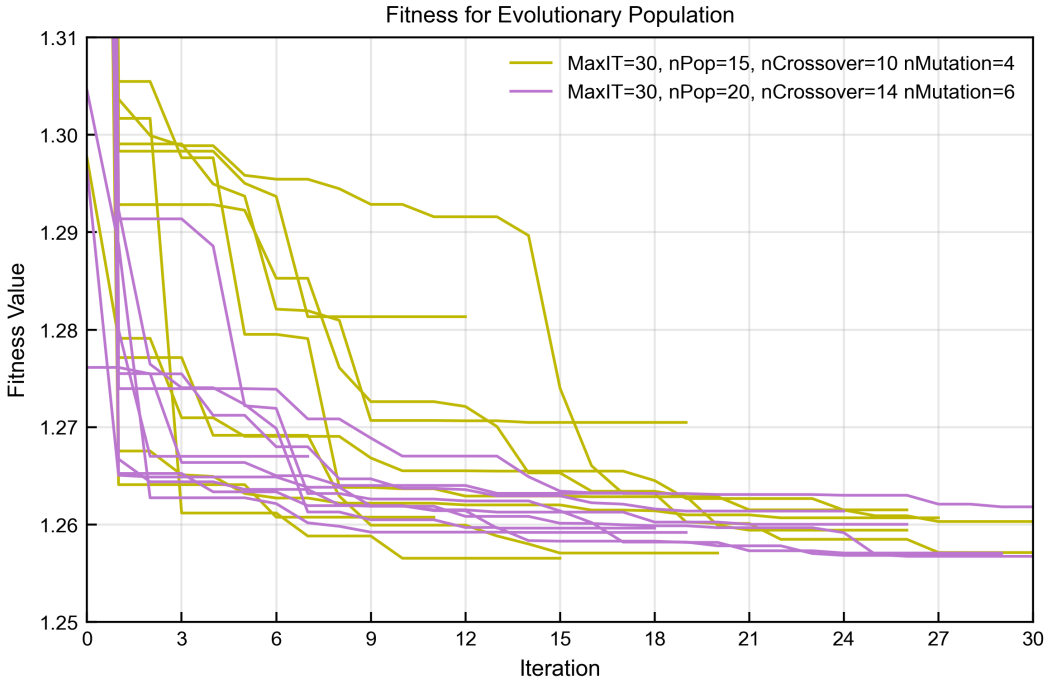

Figure D.3: Fitness convergence across ten runs for the two best-performing GA parameter configurations, terminated either by early stopping after five consecutive identical fitness values or by reaching the maximum number of iterations.

The configuration with $n_{\text{Pop}} = 20$ converges slightly faster initially, but this has limited impact on termination behaviour. Median termination occurs at 23 and 25 iterations for configurations (1) and (2), respectively, indicating similar convergence speed.

Fitness distributions in the boxplots in Figure D.4 show comparable interquartile ranges, but the larger population yields lower average fitness and reduced variability. The smaller population shows greater variation due to two outlier solutions. These results suggest that the larger population size yields more robust convergence and higher solution quality across repeated runs.

To validate these findings, the resulting GA solutions were re-evaluated using full-year QD simulations, shown in Figure D.5. The configuration with $n_{\text{Pop}} = 20$ again exhibits a smaller spread, confirming its more stable performance under full-year evaluation.

Despite this improved robustness, the average fitness advantage of the configuration with $n_{\text{Pop}} = 20$ remains marginal, and its median fitness is slightly worse than than of the configuration with $n_{\text{Pop}} = 15$. This indicates that optimisation based on representative days does not fully translate to annual performance, suggesting potential improvements in capturing average or extreme conditions.

Overall, $n_{\text{Pop}} = 20$ provides more robust performance. A population of 15 may be preferred when computational efficiency is critical, whereas a population of 20 is preferable when robustness is prioritised,

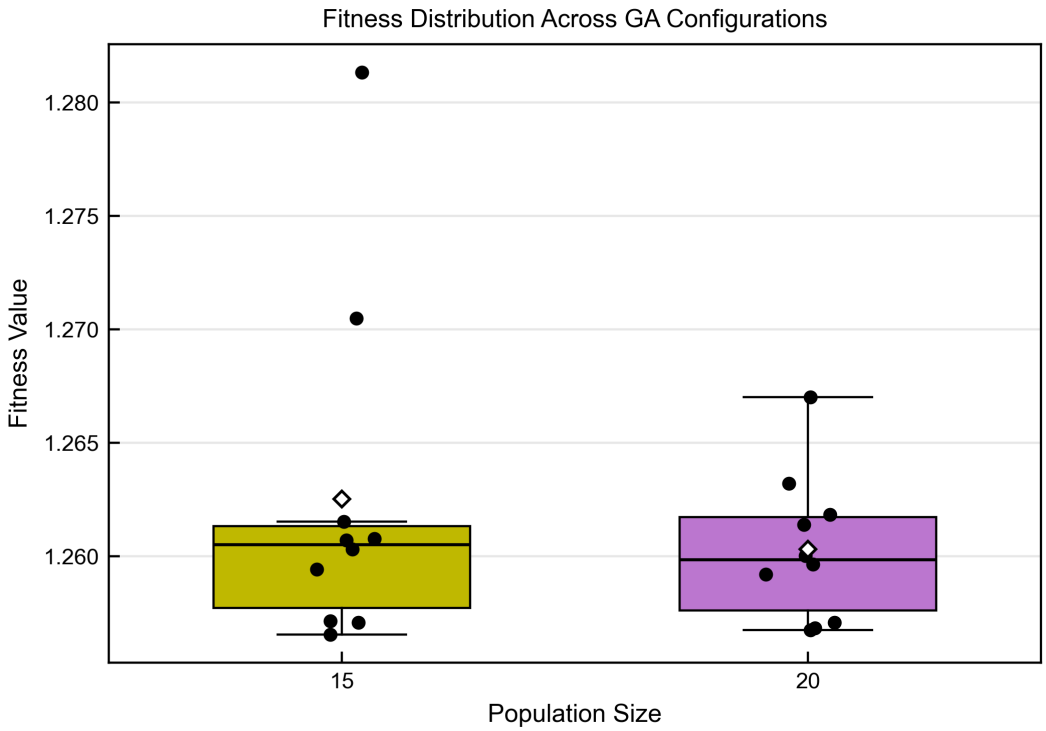

Figure D.4: Boxplots of fitness values across ten runs for the two best-performing GA configurations. Boxes represent the IQR range, whiskers correspond to 1.5 IQR, the horizontal line denotes the median fitness, diamond markers indicate the mean fitness, and individual dots represent separate GA runs.

due to its more stable convergence behaviour under both GA optimisation and full-year validation. The final configuration therefore adopts $n_{\text{Pop}} = 20$ with crossover and mutation rates fixed at 70% and 30%.

D.4. Bias Between GA-Optimisation and Full-Year Evaluation

To quantify the systematic discrepancy between GA-estimated fitness values and objective-function values obtained from full-year QD simulation evaluation, the absolute deviation per run Δ_i is defined as:

$$\Delta_i = fit_i^{year} - fit_i^{GA}, \tag{D.1}$$

with the mean deviation (bias) $\overline{\Delta}$ computed as:

$$\overline{\Delta} = \frac{1}{N} \sum_{i=1}^{N} \Delta_i, \tag{D.2}$$

where, fit_i^{year} is the fitness value resulting from full-year QD simulation, fit_i^{GA} is the fitness value resulting from GA optimisation using a reduced set of representative operating days and N is the number of runs. For all GA runs, the full-year QD simlation results in higher fitness values, indicating a systematic underestimation of fitness when using representative operating days.

The mean absolute deviation, computed using Equations D.1 and D.2, equals approximately 0.0067, corresponding to a small average relative deviation of approximately 0.53%. Figure D.6 shows limited spread, indicating consistent bias across runs rather than driven by outliers. This suggests that either extreme system conditions are not fully captured by the selected representative days or the average power losses are not accurately represented, although the resulting error remains limited.

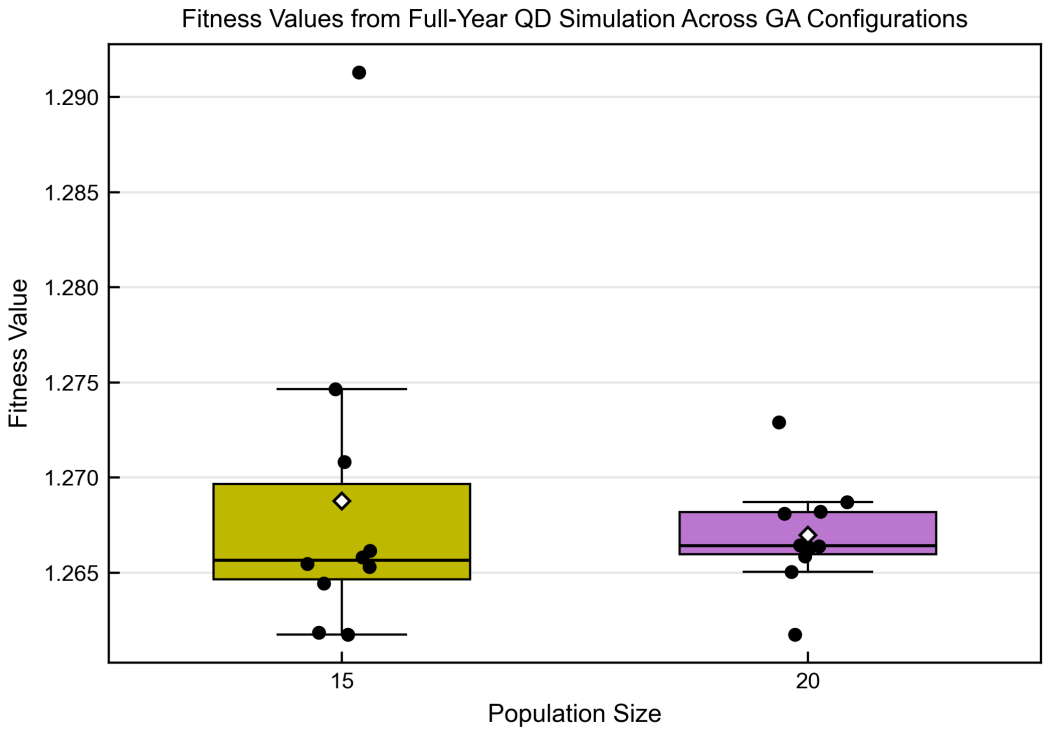

Figure D.5: Boxplots of fitness values computed using full-year QD simulation results for network configurations obtained from ten GA runs. Boxes represent the IQR range, whiskers correspond to 1.5 IQR, the horizontal line denotes the median fitness, diamond markers indicate the mean fitness, and individual dots represent separate GA runs.

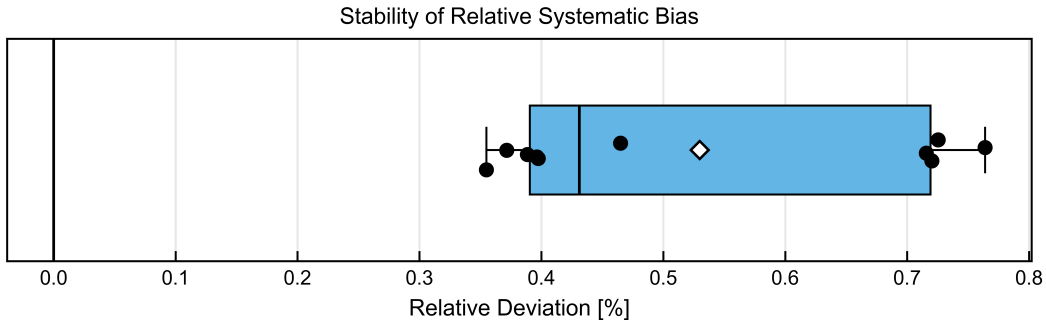

Figure D.6: Boxplot of the relative deviation between full-year QDSL-evaluated objective-function values and GA-estimated fitness values based on representative operating days. Boxes represent the interquartile range, whiskers correspond to 1.5 IQR, the central line denotes the median, diamond markers indicate the mean, and individual dots correspond to relative deviations observed for separate GA runs.

E

Results

E.1. Impact of Transformer Tap Changes

Table E.1: Impact of transformer tap changes at the distribution transformer of secondary substation 1 (10.75/0.42 kV, 400 kVA), with all seven remaining distribution transformers operating at their neutral tap position. Each tap step corresponds to a voltage change of 2.32%. The table summarizes the total apparent, active, and reactive power at the annual system peak load (19 January 2025, 16:00), together with annual cable and distribution transformer active power losses.

Tap Setting	**1**	**2**	**3 (Neutral)**	**4**	**5**
Apparent power [MVA]	2.431	2.428	2.427	2.428	2.430
	(+0.171%)	(+0.042%)	-	(+0.034%)	(+0.136%)
Active power [MW]	2.384	2.381	2.380	2.380	2.382
	(+0.165%)	(+0.042%)	-	(+0.028%)	(+0.118%)
Reactive power [kvar]	477.5	476.0	475.8	476.8	478.7
	(+0.338%)	(+0.034%)	-	(+0.194%)	(+0.594%)
MV cable losses [MWh]	38.0	39.2	40.3	41.5	42.6
	(-5.8%)	(-2.9%)	-	(+2.9%)	(+5.7%)
LV cable losses [MWh]	40.8	17.8	9.6	14.4	30.5
	(+324.0%)	(+84.7%)	-	(+49.9%)	(+217.0%)
Transformer losses [MWh]	49.5	47.0	46.1	46.5	48.0
	(+7.3%)	(+2.0%)	-	(+0.8%)	(+4.0%)
Total losses [MWh]	128.3	103.9	96.1	102.4	121.1
	(+33.5%)	(+8.1%)	-	(+6.6%)	(+26.0%)

Table E.2: Impact of transformer tap changes at the distribution transformer of secondary substation 2 (10.75/0.42 kV, 400 kVA), with all seven remaining distribution transformers operating at their neutral tap position. Each tap step corresponds to a voltage change of 2.32%. The table summarizes the total apparent, active, and reactive power at the annual system peak load (19 January 2025, 16:00), together with annual cable and distribution transformer active power losses.

Tap Setting	1	2	3 (Neutral)	4	5
Apparent power [MVA]	2.431	2.428	2.427	2.428	2.430
	(+0.158%)	(+0.038%)	-	(+0.033%)	(+0.129%)
Active power [MW]	2.383	2.381	2.380	2.380	2.382
	(+0.152%)	(+0.038%)	-	(+0.029%)	(+0.116%)
Reactive power [kvar]	477.3	476.1	475.8	476.5	478.0
	(+0.312%)	(+0.044%)	-	(+0.144%)	(+0.462%)
MV cable losses [MWh]	39.1	39.7	40.3	41.0	41.6
	(-3.1%)	(-1.6%)	-	(+1.6%)	(+3.2%)
LV cable losses [MWh]	40.2	17.8	9.6	13.9	29.0
	(+318.0%)	(+84.9%)	-	(+44.4%)	(+201.5%)
Transformer losses [MWh]	48.0	46.5	46.1	46.8	48.5
	(+4.1%)	(+0.8%)	-	(+1.5%)	(+5.1%)
Total losses [MWh]	127.3	104.0	96.1	101.7	119.1
	(+32.5%)	(+8.2%)	-	(+5.8%)	(+23.9%)

Table E.3: Impact of transformer tap changes at the distribution transformer of secondary substation 3 (10.25/0.40 kV, 315 kVA), with all seven remaining distribution transformers operating at their neutral tap position. Each tap step corresponds to a voltage change of 2.44%. The table summarizes the total apparent, active, and reactive power at the annual system peak load (19 January 2025, 16:00), together with annual cable and distribution transformer active power losses.

Tap Setting	1	2	3 (Neutral)	4	5
Apparent power [MVA]	2.435	2.429	2.427	2.429	2.434
	(+0.325%)	(+0.075%)	-	(+0.076%)	(+0.284%)
Active power [MW]	2.386	2.381	2.380	2.381	2.385
	(+0.288%)	(+0.069%)	-	(+0.061%)	(+0.235%)
Reactive power [kvar]	481.8	476.9	475.8	478.0	483.0
	(+1.248%)	(+0.227%)	-	(+0.456%)	(+1.508%)
MV cable losses	38.2	39.2	40.3	41.6	42.9
	(-5.3%)	(-2.8%)	-	(+3.1%)	(+6.3%)
LV cable losses	60.0	23.1	9.6	16.4	40.8
	(+523.3%)	(+139.9%)	-	(+70.9%)	(+323.9%)
Transformer losses	57.5	48.3	46.1	50.1	59.4
	(+24.6%)	(+4.6%)	-	(+8.6%)	(+28.7%)
Total losses [MWh]	155.7	110.6	96.1	108.1	143.1
	(+62.0%)	(+15.1%)	-	(+12.5%)	(+48.9%)

Table E.4: Impact of transformer tap changes at the distribution transformer of secondary substation 4 (10.25/0.40 kV, 200 kVA), with all seven remaining distribution transformers operating at their neutral tap position. Each tap step corresponds to a voltage change of 2.44%. The table summarizes the total apparent, active, and reactive power at the annual system peak load (19 January 2025, 16:00), together with annual cable and distribution transformer active power losses.

Tap Setting	1	2	3 (Neutral)	4	5
Apparent power [MVA]	2.433	2.428	2.427	2.428	2.432
	(+0.256%)	(+0.058%)	-	(+0.063%)	(+0.231%)
Active power [MW]	2.384	2.381	2.380	2.381	2.384
	(+0.199%)	(+0.044%)	-	(+0.053%)	(+0.188%)
Reactive power [kvar]	483.9	477.8	475.8	477.4	482.1
	(+1.690%)	(+0.414%)	-	(+0.331%)	(+1.307%)
MV cable losses [MWh]	41.6	40.9	40.3	40.0	39.8
	(+3.2%)	(+1.3%)	-	(-0.9%)	(-1.3%)
LV cable losses [MWh]	31.2	14.1	9.6	16.2	32.2
	(+224.2%)	(+46.5%)	-	(+68.0%)	(+234.4%)
Transformer losses [MWh]	65.9	51.1	46.1	49.7	60.8
	(+42.9%)	(+10.7%)	-	(+7.8%)	(+31.7%)
Total losses [MWh]	138.7	106.0	96.1	105.9	132.8
	(+44.3%)	(+10.3%)	-	(+10.2%)	(+38.2%)

Table E.5: Impact of transformer tap changes at the distribution transformer of secondary substation 5 (10.25/0.40 kV, 315 kVA), with all seven remaining distribution transformers operating at their neutral tap position. Each tap step corresponds to a voltage change of 2.44%. The table summarizes the total apparent, active, and reactive power at the annual system peak load (19 January 2025, 16:00), together with annual cable and distribution transformer active power losses.

Tap Setting	1	2	3 (Neutral)	4	5
Apparent power [MVA]	2.434	2.429	2.427	2.429	2.433
	(+0.319%)	(+0.074%)	-	(+0.073%)	(+0.271%)
Active power [MW]	2.386	2.381	2.380	2.381	2.386
	(+0.274%)	(+0.061%)	-	(+0.071%)	(+0.255%)
Reactive power [kvar]	482.8	477.8	475.8	476.5	479.3
	(+1.452%)	(+0.413%)	-	(+0.130%)	(+0.722%)
MV cable losses [MWh]	40.5	40.3	40.3	40.6	41.0
	(+0.4%)	(-0.1%)	-	(+0.6%)	(+1.7%)
LV cable losses [MWh]	56.9	20.6	9.6	20.5	50.3
	(+491.3%)	(+114.1%)	-	(+113.2%)	(+422.8%)
Transformer losses [MWh]	58.1	49.4	46.1	47.6	53.3
	(+26.0%)	(+7.0%)	-	(+3.3%)	(+15.5%)
Total losses [MWh]	155.5	110.3	96.1	108.7	144.6
	(+61.8%)	(+14.8%)	-	(+13.1%)	(+50.5%)

Table E.6: Impact of transformer tap changes at the distribution transformer of secondary substation 6 (10.75/0.42 kV, 630 kVA), with all seven remaining distribution transformers operating at their neutral tap position. Each tap step corresponds to a voltage change of 2.32%. The table summarizes the total apparent, active, and reactive power at the annual system peak load (19 January 2025, 16:00), together with annual cable and distribution transformer active power losses.

Tap Setting	1	2	3 (Neutral)	4	5
Apparent power [MVA]	2.432	2.428	2.427	2.428	2.431
	(+0.217%)	(+0.051%)	-	(+0.050%)	(+0.187%)
Active power [MW]	2.384	2.381	2.380	2.381	2.384
	(+0.204%)	(+0.047%)	-	(+0.048%)	(+0.180%)
Reactive power [kvar]	478.5	476.5	475.8	476.3	477.7
	(+0.548%)	(+0.140%)	-	(+0.095%)	(+0.386%)
MV cable losses [MWh]	44.7	42.3	40.3	38.7	37.3
	(+10.7%)	(+4.9%)	-	(-4.1%)	(-7.6%)
LV cable losses [MWh]	43.6	16.3	9.6	20.8	47.6
	(+353.0%)	(+69.7%)	-	(+116.5%)	(+395.4%)
Transformer losses [MWh]	50.0	47.4	46.1	46.0	46.9
	(+5.5%)	(-2.7%)	-	(-2.9%)	(-1.0%)
Total losses [MWh]	138.2	106.0	96.1	105.5	131.8
	(+43.8%)	(+10.3%)	-	(+9.8%)	(+37.2%)

Table E.7: Impact of transformer tap changes at the distribution transformer of secondary substation 7 (10.25/0.40 kV, 250 kVA), with all seven remaining distribution transformers operating at their neutral tap position. Each tap step corresponds to a voltage change of 2.44%. The table summarizes the total apparent, active, and reactive power at the annual system peak load (19 January 2025, 16:00), together with annual cable and distribution transformer active power losses.

Tap Setting	1	2	3 (Neutral)	4	5
Apparent power [MVA]	2.431	2.428	2.427	2.427	2.430
	(+0.196%)	(+0.052%)	-	(+0.025%)	(+0.118%)
Active power [MW]	2.384	2.381	2.380	2.380	2.382
	(+0.181%)	(+0.050%)	-	(+0.019%)	(+0.098%)
Reactive power [kvar]	478.5	476.4	475.8	476.7	478.7
	(+0.558%)	(+0.111%)	-	(+0.175%)	(+0.606%)
MV cable losses [MWh]	40.9	40.6	40.3	40.3	40.3
	(+1.5%)	(+0.5%)	-	(-0.2%)	(0.0%)
LV cable losses [MWh]	38.9	17.8	9.6	12.5	25.1
	(+304.1%)	(+85.2%)	-	(+30.3%)	(+160.5%)
Transformer losses [MWh]	52.5	47.7	46.1	47.4	51.2
	(+13.9%)	(+3.4%)	-	(+2.8%)	(+11.0%)
Total losses [MWh]	132.3	106.1	96.1	100.2	116.6
	(+37.6%)	(+10.4%)	-	(+4.3%)	(+21.3%)

Table E.8: Impact of transformer tap changes at the distribution transformer of secondary substation 8 (10.25/0.398 kV, 200 kVA), with all seven remaining distribution transformers operating at their neutral tap position. Each tap step corresponds to a voltage change of 2.44%. The table summarizes the total apparent, active, and reactive power at the annual system peak load (19 January 2025, 16:00), together with annual cable and distribution transformer active power losses.

Tap Setting	**1**	**2**	**3 (Neutral)**	**4**	**5**
Apparent power [MVA]	2.431	2.427	2.427	2.428	2.432
	(+0.163%)	(+0.028%)	-	(+0.065%)	(+0.210%)
Active power [MW]	2.383	2.380	2.380	2.381	2.384
	(+0.139%)	(+0.023%)	-	(+0.057%)	(+0.184%)
Reactive power [kvar]	479.5	476.6	475.8	477.1	480.0
	(+0.766%)	(+0.149%)	-	(+0.255%)	(+0.867%)
MV cable losses [MWh]	42.3	41.2	40.3	39.7	39.3
	(+4.9%)	(+2.1%)	-	(-1.5%)	(-2.6%)
LV cable losses [MWh]	27.3	11.6	9.6	19.4	39.4
	(+184.0%)	(+20.9%)	-	(+101.7%)	(+309.5%)
Transformer losses [MWh]	55.4	48.2	46.1	48.3	54.3
	(+20.1%)	(+4.6%)	-	(+4.8%)	(+17.8%)
Total losses [MWh]	125.0	101.0	96.1	107.4	133.0
	(+30.1%)	(+5.1%)	-	(+11.8%)	(+38.4%)

E.2. Initial Searching Point

E.2.1. Present-day Operating Scenario

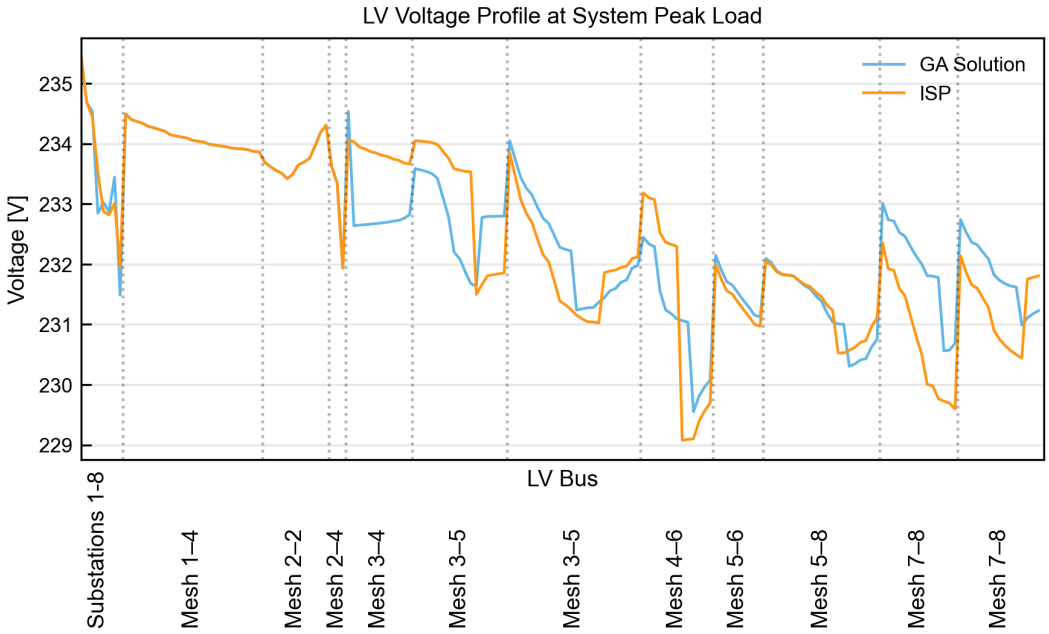

Figure E.1: LV voltage profile of the de-meshed network at annual peak consumption (19 January 2025, 16:00). Substations 1–8 denote the buses at the secondary sides of the distribution transformers, while the remaining buses are grouped according to their original LV mesh cables (mesh x–x). Voltage profiles are shown for the ISP configuration, and the GA-optimised grid configuration.

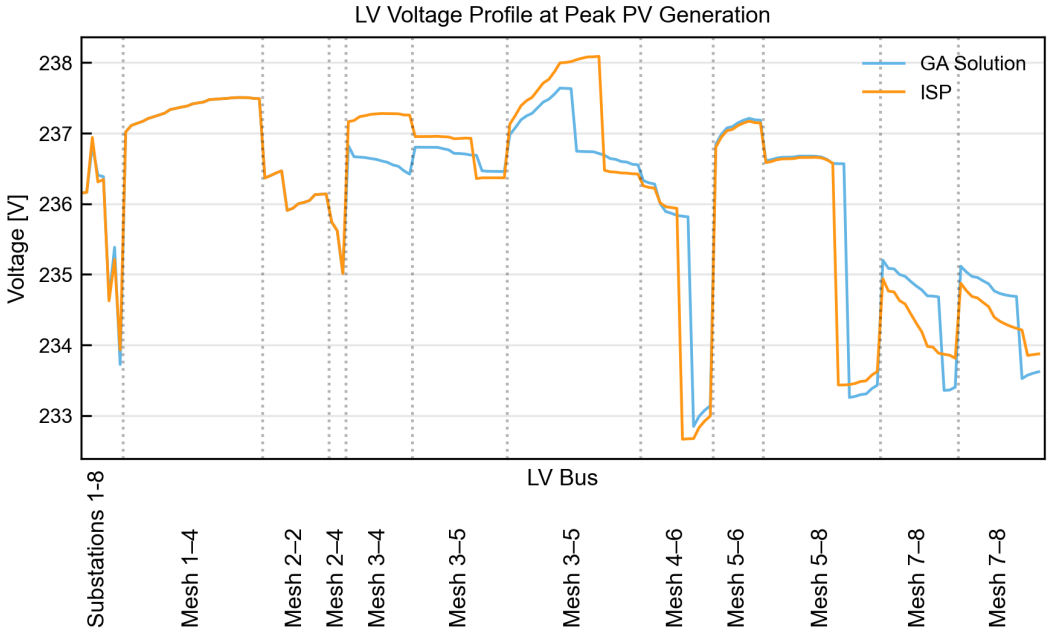

Figure E.2: LV voltage profile of the de-meshed network at annual peak PV generation (29 April 2025, 11:00). Substations 1–8 denote the buses at the secondary sides of the distribution transformers, while the remaining buses are grouped according to their original LV mesh cables (mesh x–x). Voltage profiles are shown for the ISP configuration and the GA-optimised grid configuration.

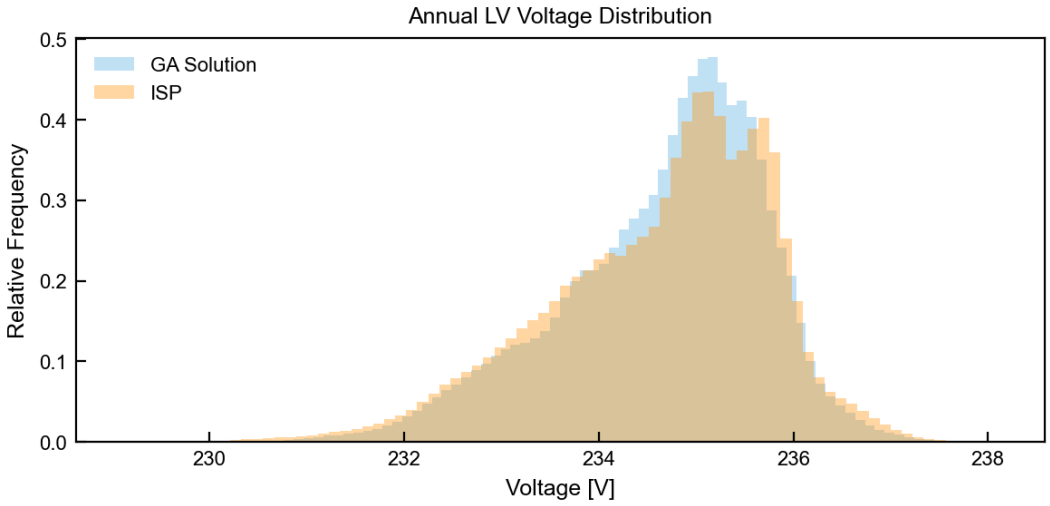

Figure E.3: Distribution of LV bus voltages over the simulated year for the ISP configuration and GA-optimised grid configuration. The histogram represents the relative frequency of voltage values across all LV buses and all simulated time steps.

E.2.2. Future Operating Scenario

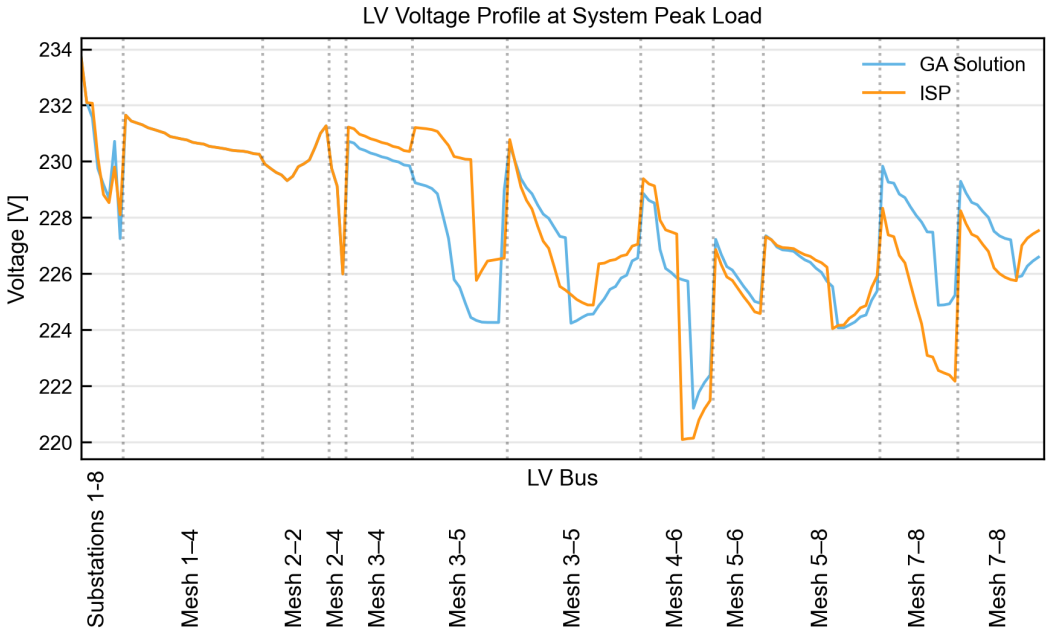

Figure E.4: LV voltage profile of the de-meshed network under future demand scenario at annual peak consumption (19 January 2025, 16:00). Substations 1–8 denote the buses at the secondary sides of the distribution transformers, while the remaining buses are grouped according to their original LV mesh cables (mesh x–x). Voltage profiles are shown for the ISP configuration and the GA-optimised grid configuration.

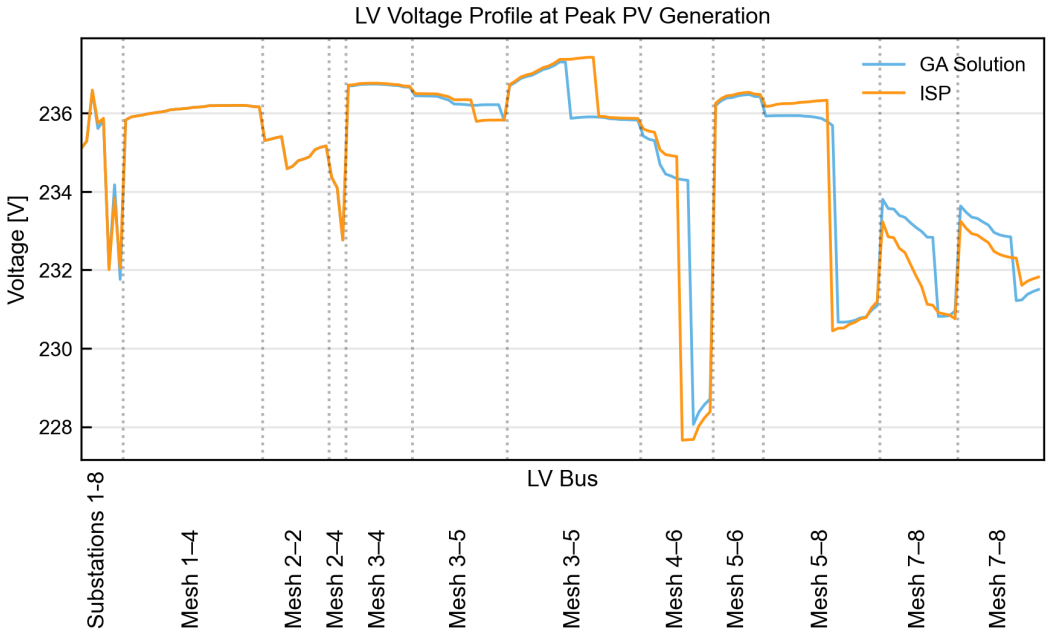

Figure E.5: LV voltage profile of the de-meshed network under future demand scenario at annual peak PV generation (29 April 2025, 11:00). Substations 1–8 denote the buses at the secondary sides of the distribution transformers, while the remaining buses are grouped according to their original LV mesh cables (mesh x–x). Voltage profiles are shown for the ISP configuration and the GA-optimised grid configuration.

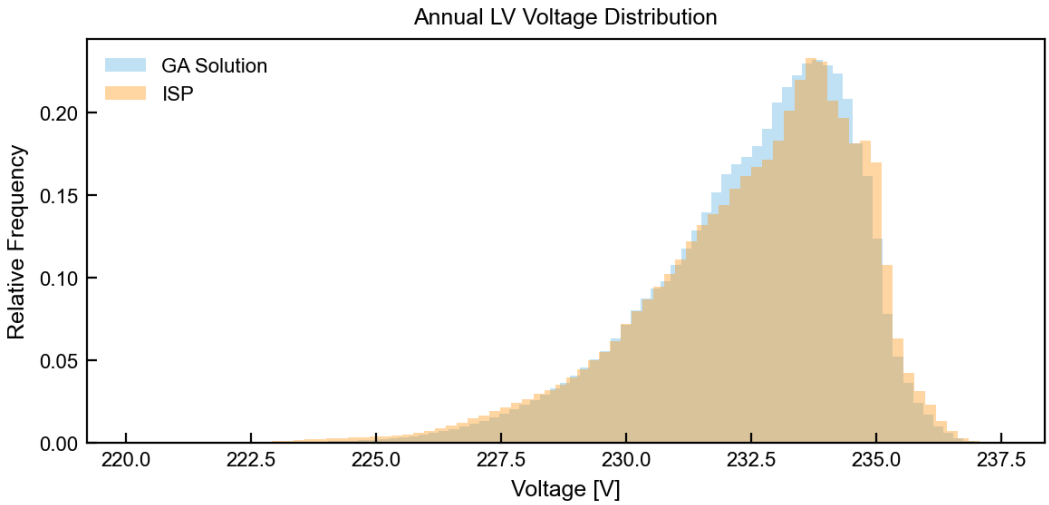

Figure E.6: Distribution of LV bus voltages under future demand scenario over the simulated year for the ISP configuration and GA-optimised grid configuration. The histogram represents the relative frequency of voltage values across all LV buses and all simulated time steps.